



Master's Diploma Thesis
Department of Applied Mathematics
University of Crete

Partial array imaging of extended reflectors in two- dimensional waveguides

Symeon Papadimitropoulos

Advisors: Prof. Chrysoula Tsogka
Prof. Dimitris Mitsoudis

Heraklion, April 2015

Contents

	Page
1 Full array imaging	5
1.1 Array imaging setup	7
1.2 Imaging	8
1.3 Selective imaging	10
1.4 Numerical experiments	12
2 A One-Dimensional Model Problem	20
2.1 Properties of the array response matrix	21
2.1.1 Selective imaging for the model problem	25
2.2 Spectral properties of A_M (revisited)	27
2.2.1 A crack with an endpoint fixed on the surface	28
2.2.2 A crack with endpoints $\alpha, \beta \in (0, D]$, ($\alpha < \beta$)	31
2.3 Selective imaging for the model problem revisited	32
2.4 Numerical experiments	36
3 Model problems vs. full objects	39
3.1 Square scatterer vs. crack	39
3.2 Disc shaped scatterer vs. semicircle	41
4 Partial array imaging	46
4.1 The weighted modal projection for the partial array case . . .	46
4.2 Imaging with \mathcal{I}^{KM} for the model problem	52
4.3 Imaging with $\tilde{\mathcal{I}}^{\text{KM}}$ for the model problem	56
4.3.1 Using a regularized pseudoinverse	60
4.3.2 Adding noise in the data	64

4.3.3	Algorithm for imaging with partial aperture arrays . .	67
4.4	Application of the algorithm	68
4.4.1	Off-centered cuts	74
A	Resolution analysis for a point scatterer	80
A.1	Cross-range resolution for $\tilde{\mathcal{I}}^{\text{KM}}(\omega)$	81
A.2	Range resolution for $\tilde{\mathcal{I}}^{\text{KM}}(\omega)$	83

Introduction

In this work we consider the problem of detecting and imaging *extended* reflectors in a waveguide, using a vertical array of transducers with *partial aperture*, *i.e.*, an array that does not span the whole depth of the waveguide. The term *extended* refers to reflectors that are comparable in size to the acoustic wavelength. The current work carries on the methodology that we have proposed in [1], in order to selectively image extended scatterers in waveguides with the aid of a vertical full-aperture array of transducers, with the intention to extend its applicability in the more general case where the array has partial aperture. In both of these works we have in mind applications in underwater acoustics where sound waves are used to probe the sea and its echoes are recorded and analysed in order to detect objects submerged in the sea. The marine environment that we consider is modelled as a single-layer two-dimensional waveguide with horizontal boundaries. Although this is a simplified and rather ideal model of a marine acoustic environment it still carries and exhibits the main features and challenges of acoustic wave propagation in the sea.

We now present the main features of the imaging problem that we are interested in. We assume that an array consisting of N transducers is set vertically in the waveguide. At first, each element of the array acts as a point source and emits a sound pulse, whose echoes are recorded in all the elements of the array that now act as receivers. In this way it is formed an $N \times N$ matrix $\hat{\Pi}$; this is the so-called *array response matrix*. Specifically, we shall consider that we are given the array response matrix for the scattered field, where this is obtained, as usually, by subtracting the incident field from the total field. Having these data in our hands, we want to create images of parts of the waveguide that would assist us to decide whether a scatterer

is present or not. Of course, it is highly desirable to be able to extract from the image additional information about the size and the shape of the scatterer. The usual procedure in imaging is summarised in the following steps: a) We determine a bounded subdomain of the waveguide that is usually called the *search domain*, b) we discretize the search domain, and c) in each node of the search domain we associate the value of an imaging functional. Then the graph of this functional forms the image that we are looking for, where, usually, peaks that are related with the functional's maxima indicate the presence of the scatterer. Examples of widely used imaging functionals include the *Kirchhoff Migration functional* (KM) (see [2, §9]) and the *matched field functional* (see [3]).

In our previous work, [1], we have proposed an alternative functional, that was based on Kirchhoff migration, and on a weighted modal projection of the array response matrix denoted by $\widehat{\mathbb{P}}$, for imaging extended scatterers in waveguides using an active array of sensors which spans the whole depth of the waveguide. Moreover, we have introduced a filtered version of this functional, based on the singular value decomposition of $\widehat{\mathbb{P}}$, in order to image selectively on specific parts of the scatterer. This approach belongs to the class of the so-called *subspace projection methods*, [4]. In [4], the subspace projection method was employed in order to image selectively extended scatterers in free space. We refer also to [5] for selective imaging in clutter, *i.e.*, propagation medium with inhomogeneities that are unknown, cannot be estimated in detail, and, are modelled as random processes. Note that the concept of selective imaging of extended scatterers has been motivated by the concept of *selective focusing*, which concerns multiple point (or small) scatterers in the medium and, essentially, allows you to distinguish specific scatterers by creating an image which focuses on them. Related works include [6], where Prada and Fink introduced the well-known DORT method in order to achieve selective focusing on individual scatterers, [7, 8], [9] where DORT was analysed with mathematical rigor in the free-space, and [10] for a waveguide problem.

The thesis is organised as follows. In Chapter 1 we formulate the imaging problem and briefly review the selective imaging approach that was proposed in [1]. The array response matrix for the numerical results shown in

Section 1.4 and, later, in Chapters 3 and 4, is obtained by solving numerically the wave equation in the time domain using a high-order finite element C++ code, called Montjoie [11]. Montjoie has been developed in INRIA and is very efficient in solving equations that arise in wave propagation problems.

In Chapter 2 we review the theoretical analysis of the imaging approach that was carried out in [1] for a simplified model problem where the scatterer is a crack, *i.e.*, a vertical one-dimensional perfect reflector. The simpler nature of this problem, and the Born approximation, allowed us to characterise the spectral properties of the weighted modal projection of the array response matrix, $\hat{\mathbb{P}}$. In particular, we have shown in [1] that the singular values of $\hat{\mathbb{P}}$, when they are normalised with respect to the largest one, cluster near one and zero, and just a few lie in the intermediate region. Moreover, in [1] we were able to show that the number of significant singular values equals the size of the scatterer divided by half the wavelength (the array resolution in the vertical direction). Also, when we project on the singular vectors that correspond to intermediate singular values, we are able to create an image that focuses on the edges of the crack. All these properties are exploited in selective imaging. Here, we push the analysis a little bit further and investigate the relation between $\hat{\mathbb{P}}$ and its singular vectors, with the well known *prolate matrix* and the *prolate spheroidal wave functions*, respectively, which have been analyzed in a series of outstanding papers by Slepian, Pollak and Landau, [12, 13, 14, 15, 16].

In Chapter 3, in order to assess if the nice properties that we have obtained for the simplified crack model-problem carry over to more general cases, we compare imaging results for the crack problem with those concerning a square scatterer. For the latter, in order to form the array response matrix, we have to solve numerically the full scattering problem, *i.e.* we do not resort to Born approximation. Our numerical results suggest that selective imaging performs equally well in this more general and complex case. The comparison between another model problem, where the scatterer is a semicircle, with a disc shaped scatterer strengthen our confidence in that selective imaging can be achieved for different reflector geometries.

The main objective of this thesis is to examine the behavior of imaging functionals when the array has partial aperture, *i.e.*, it does not span the

whole depth of the waveguide, and this is the subject of Chapter 4. In the case of the partial array aperture some key properties, like the orthonormality of the vertical eigenfunctions along the array, do not hold any more. In Chapter 4 we modify the definition of the weighted projected matrix $\hat{\mathbb{P}}$ that plays a crucial role in the construction of our imaging functional. This allows us to extend the applicability of our methodology in the case of partial array aperture. We first examine the performance of the proposed imaging functional for the model problem of the crack and compare the results with the ones obtained with KM as we decrease the array aperture. We observe that our approach gives better imaging results and its superiority becomes more significant as the array aperture decreases. We also examine numerically the performance of our methodology in the presence of additive noise and in the case of extended reflectors such as a square and a disc.

We close this thesis with some concluding remarks, and with a brief discussion about possible future extensions

Chapter 1

Full array imaging

We consider the problem of detecting and imaging extended scatterers submerged in the sea using acoustic waves. More precisely, we model a marine environment as an infinite two-dimensional waveguide $\mathbb{R} \times (0, D)$ in Cartesian coordinates (z, x) , where z denotes the range variable, and x the depth (cross-range) variable taken to be positive downward. Throughout this work, vectors in \mathbb{R}^n are denoted by boldface characters while vectors in $\mathbb{R} \times (0, D)$ are denoted by boldface characters with an overscript arrow. Our waveguide consists of a single water layer, with constant density and constant sound speed c_0 . A single extended scatterer denoted by \mathcal{O} is submerged in the water layer, see Figure 1.1. The term ‘extended’ indicates that the typical size of the scatterer is comparable to the wavelength.

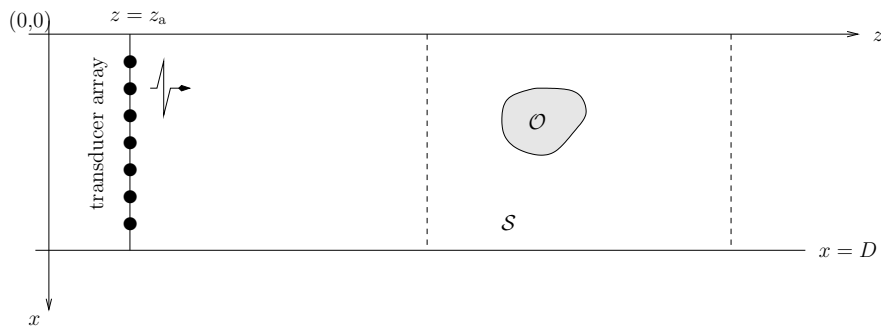


Figure 1.1: Schematic representation of our waveguide problem and of the active array imaging setup.

We assume that the total acoustic pressure field $p^{\text{tot}}(t, \vec{x})$ satisfies the wave equation

$$\Delta p^{\text{tot}}(t, \vec{x}) - \frac{1}{c_0^2} \frac{\partial^2 p^{\text{tot}}(t, \vec{x})}{\partial t^2} = f(t, \vec{x}), \quad (1.1)$$

where the source term is of the form $f(t, \vec{x}) = -\exp(i\omega t)\delta(\vec{x} - \vec{x}_s)$, modelling a point-like source with time harmonic dependence located at \vec{x}_s . The scatterer is assumed to be sound-hard, hence a homogeneous Neumann condition is posed on its boundary $\partial\mathcal{O}$. Equation (1.1) is supplemented with pressure release boundary conditions on the surface and the seafloor, and we also assume that $p^{\text{tot}}(t, \vec{x}) = 0$ for $t \leq 0$, expressing that the medium is quiescent before emission. Taking the Fourier transform

$$\widehat{p}^{\text{tot}}(\omega, \vec{x}) = \int e^{i\omega t} p^{\text{tot}}(t, \vec{x}) dt,$$

we obtain from (1.1) the Helmholtz equation

$$-\Delta \widehat{p}^{\text{tot}}(\omega, \vec{x}) - k^2 \widehat{p}^{\text{tot}}(\omega, \vec{x}) = \widehat{f}(\omega, \vec{x}), \quad (1.2)$$

where $k = \omega/c_0$ is the real wavenumber, ω is the angular frequency, and $\lambda = 2\pi/k$ is the wavelength.

Now, let $\{\mu_n, X_n\}_{n=1,2,\dots}$ denote the eigenvalues and corresponding orthonormal eigenfunctions of the two-point vertical eigenvalue problem

$$X''(x) + \mu X(x) = 0, \quad x \in (0, D) \quad \text{and} \quad X(0) = X(D) = 0,$$

i.e.,

$$\mu_n = (n\pi/D)^2, \quad X_n(x) = \sqrt{2/D} \sin(\sqrt{\mu_n}x), \quad n = 1, 2, \dots \quad (1.3)$$

The family of eigenfunctions $\{X_n\}_{n=1,2,\dots}$ forms an orthonormal basis of $L^2[0, D]$. We assume that for each frequency there exists an index M such that

$$\mu_M < k^2 < \mu_{M+1}.$$

In other words, the wavenumber does not coincide with any of the mode cutoff frequencies, and the first M eigenvalues correspond to the *propagating*

modes, while the rest to the *evanescent* modes. Let us also denote the horizontal wavenumbers by

$$\beta_n = \begin{cases} \sqrt{k^2 - \mu_n}, & 1 \leq n \leq M, \\ i\sqrt{\mu_n - k^2}, & n \geq M + 1. \end{cases} \quad (1.4)$$

Moreover, let $\widehat{G}(\vec{\mathbf{x}}, \vec{\mathbf{x}}_s)$ be the outgoing Green's function of the Helmholtz operator $-\Delta \cdot -k^2 \cdot$, evaluated at $\vec{\mathbf{x}} = (z, x) \in \mathbb{R} \times (0, D)$ due to a point source located at $\vec{\mathbf{x}}_s = (z_s, x_s)$. (In the underwater acoustics community a point source in plane geometry is usually referred to as a line source, [17].) Then it is well known, see, e.g., [17, 10], that \widehat{G} admits the following normal mode representation

$$\widehat{G}(\vec{\mathbf{x}}, \vec{\mathbf{x}}_s) = \frac{i}{2} \sum_{n=1}^{\infty} \frac{1}{\beta_n} e^{i\beta_n |z - z_s|} X_n(x) X_n(x_s), \quad (1.5)$$

where $\{\mu_n, X_n\}$ and β_n are defined in (1.3) and (1.4), respectively.

1.1 Array imaging setup

We consider a one-dimensional vertical active array \mathcal{A} , spanning the whole depth of the waveguide and located at range $z = z_a \geq 0$, see Figure 1.1. The array consists of N transducers which act both as sources and receivers. We assume that they are closely spaced and uniformly distributed on the array with an inter-element array distance h , which is usually called the array *pitch*.

Let, also, $\widehat{\Pi}(\omega)$ denote the $N \times N$ complex *array response matrix* in the frequency domain, whose (r, s) entry is defined as the Fourier transform of the time traces recorded at the r -th transducer due to a δ -function impulse generated by the s -th transducer, for a given frequency ω . In what follows, the data that we are going to use for imaging is the array response matrix for the scattered field in the frequency domain, created by subtracting the array response matrix for the incident field from the corresponding one for the total field.

1.2 Imaging

Let us first define the search domain \mathcal{S} , as a bounded subdomain of our waveguide that may contain a scatterer (see Figure 1.1). \mathcal{S} is discretized, using a rectangular grid, and $\vec{y}^s = (z^s, x^s)$ denotes an arbitrary node in \mathcal{S} . We are interested in creating an image of the search domain \mathcal{S} . A classical imaging method is *Kirchhoff migration (KM)*, [18, 19], defined by,

$$\mathcal{I}^{\text{KM}}(\vec{y}^s, \omega) = \sum_{r=1}^N \overline{\widehat{G}(\vec{x}_r, \vec{y}^s, \omega)} \sum_{s=1}^N \widehat{\Pi}(\vec{x}_r, \vec{x}_s, \omega) \overline{\widehat{G}(\vec{x}_s, \vec{y}^s, \omega)}, \quad (1.6)$$

for a single frequency ω and $\vec{y}^s \in \mathcal{S}$. Here the bars denote complex conjugation. KM consists in backpropagating the signals from each receiver \vec{x}_r to a point \vec{y}^s in the search domain and then back to the source \vec{x}_s . The image is the sum of the backpropagated signals for all sources and receivers.

In (1.6) we have defined the imaging functional for a single frequency ω . When we have multi-frequency data, we can compute instead,

$$\mathcal{I}^{\text{KM}}(\vec{y}^s) = \left| \sum_{\omega} \mathcal{I}^{\text{KM}}(\vec{y}^s, \omega) \right|. \quad (1.7)$$

KM is widely used in seismic imaging and exploration geophysics; in these applications the arrays and the bandwidth are typically very large. This is a setup in which perfect imaging resolution can be achieved. Indeed, in that case the ideal point spread function (i.e., the image of a point scatterer), which is a Dirac distribution, can be obtained, at least asymptotically, as the array aperture and the bandwidth tend to infinity (cf. [18]). To be more precise, this result is obtained for a slight modification of (1.6) that uses a weighing factor that takes into account the source-receiver geometry.

We will assume in the following, that the scatterer and the search domain are located far enough from the array to allow us to retain only the propagating modes in (1.5). Then, replacing \widehat{G} , given by (1.5), into (1.6) we may write the KM functional in the form

$$\begin{aligned} \mathcal{I}^{\text{KM}}(\vec{y}^s, \omega) &= -\frac{1}{4} \sum_{s,r=1}^N \widehat{\Pi}(\vec{x}_r, \vec{x}_s, \omega) \times \\ &\times \sum_{m,n=1}^M \frac{e^{-i(\beta_m + \beta_n)|z_a - z^s|}}{\beta_m \beta_n} X_m(x_s) X_m(x^s) X_n(x_r) X_n(x^s). \end{aligned} \quad (1.8)$$

Assuming that the array pitch h is small enough, we can approximate the double sum in (1.8) by a double integral over \mathcal{A} . In the case where the array spans the whole waveguide depth $\mathcal{A} = [0, D]$, hence

$$\begin{aligned}\mathcal{I}^{\text{KM}}(\vec{\mathbf{y}}^s, \omega) &\approx -\frac{1}{4h^2} \int_0^D dx_s \int_0^D dx_r \hat{\Pi}(\vec{\mathbf{x}}_s, \vec{\mathbf{x}}_r, \omega) \times \\ &\quad \times \sum_{m,n=1}^M \frac{e^{-i(\beta_m+\beta_n)|z_a-z^s|}}{\beta_m\beta_n} X_m(x_s) X_m(x^s) X_n(x_r) X_n(x^s) \\ &= -\frac{1}{4h^2} \sum_{m,n=1}^M \frac{e^{-i(\beta_m+\beta_n)|z_a-z^s|}}{\beta_m\beta_n} X_m(x^s) X_n(x^s) \times \\ &\quad \times \int_0^D \int_0^D \hat{\Pi}(\vec{\mathbf{x}}_s, \vec{\mathbf{x}}_r, \omega) X_m(x_s) X_n(x_r) dx_r dx_s. \quad (1.9)\end{aligned}$$

Now, let us introduce an $M \times M$ matrix $\hat{\mathbb{Q}}(\omega)$, with entries

$$\hat{\mathbb{Q}}_{mn}(\omega) = \int_0^D dx_s \int_0^D dx_r \hat{\Pi}(\vec{\mathbf{x}}_s, \vec{\mathbf{x}}_r, \omega) X_m(x_s) X_n(x_r), \quad (1.10)$$

for $m, n = 1, 2, \dots, M$.

In view of (1.10), (1.9) may be equivalently written as

$$\mathcal{I}^{\text{KM}}(\vec{\mathbf{y}}^s, \omega) \approx -\frac{1}{4h^2} \sum_{m,n} \frac{e^{-i(\beta_m+\beta_n)|z_a-z^s|}}{\beta_m\beta_n} X_n(x^s) X_m(x^s) \hat{\mathbb{Q}}_{mn}(\omega). \quad (1.11)$$

Instead of using (1.11) we propose to use the following imaging functional

$$\tilde{\mathcal{I}}^{\text{KM}}(\vec{\mathbf{y}}^s, \omega) = -\frac{1}{4h^2} \sum_{m,n=1}^M e^{-i(\beta_m+\beta_n)|z_a-z^s|} X_n(x^s) X_m(x^s) \hat{\mathbb{P}}_{mn}(\omega), \quad (1.12)$$

where the $M \times M$ matrix $\hat{\mathbb{P}}$ is defined as

$$\hat{\mathbb{P}}_{mn}(\omega) = \beta_m\beta_n \hat{\mathbb{Q}}_{mn}, \quad m, n = 1, \dots, M. \quad (1.13)$$

For multi-frequency data, we define

$$\tilde{\mathcal{I}}^{\text{KM}}(\vec{\mathbf{y}}^s) = \left| \sum_{\omega} \tilde{\mathcal{I}}^{\text{KM}}(\vec{\mathbf{y}}^s, \omega) \right|. \quad (1.14)$$

Note that $\hat{\mathbb{P}}_{mn}(\omega)$ is a weighted modal projection of the array response matrix. While it is not yet clear why we have introduced the functional $\tilde{\mathcal{I}}^{\text{KM}}$, the reason behind it will be explained in the next chapter.

1.3 Selective imaging

In selective imaging we are interested in reconstructing specific parts of the reflector like, for example, its boundary. A way to achieve this is by means of the subspace projection method [4], which is based on the singular value decomposition (SVD) of the $N \times N$ array response matrix $\widehat{\Pi}(\omega)$ in the frequency domain. As remarked in [4], the SVD of $\widehat{\Pi}(\omega)$ may serve as a filter which enables us to identify reflections emanating from the edges of the scatterer. Such reflections are typically weaker than, and therefore masked by, those coming from the body of the scatterer. The SVD of $\widehat{\Pi}(\omega)$ is a factorization of the form (see, for example, [20, §2.5])

$$\widehat{\Pi}(\omega) = U(\omega)\Sigma(\omega)V^*(\omega),$$

where Σ is a diagonal matrix containing the singular values σ_i of $\widehat{\Pi}(\omega)$ in descending order, and U, V are unitary matrices containing the left and right singular vectors, respectively. For the rest of this section, we will occasionally omit the ω 's for the sake of notational convenience.

Now, let us write the SVD of $\widehat{\Pi}(\omega)$ as a sum of the form:

$$\widehat{\Pi}(\omega) = \sum_{i=1}^{\rho} \sigma_i U_i V_i^*,$$

where $\rho = \text{rank}(\widehat{\Pi}(\omega))$, so that $\sigma_1 \geq \dots \geq \sigma_\rho > \sigma_{\rho+1} = \dots = \sigma_N = 0$, and U_i, V_i are the left and right singular vectors, respectively. Then a filtered version of the response matrix may be written in the form:

$$D[\widehat{\Pi}(\omega)] = \sum_{i=1}^{\rho} d_i \sigma_i U_i V_i^*,$$

where the coefficients d_i are called the filter weights. We will simply consider $d_i \in \{0, 1\}$, which amounts to saying that if $d_i = 1$ then the i -th singular vector is taken into account in the filtered version of the response matrix, while if $d_i = 0$ it is not.

Let us also define the functional

$$\mathcal{I}^{\text{KM},f}(\mathbf{y}^s, \omega) = \sum_{r=1}^N \overline{\widehat{G}(\mathbf{x}_r, \mathbf{y}^s, \omega)} \sum_{s=1}^N D[\widehat{\Pi}(\mathbf{x}_r, \mathbf{x}_s, \omega)] \widehat{G}(\mathbf{x}_s, \mathbf{y}^s, \omega), \quad (1.15)$$

derived by replacing the full response matrix by its filtered version. For multi-frequency data, we define

$$\mathcal{I}^{\text{KM},\text{f}}(\vec{\mathbf{y}}^{\text{s}}) = \left| \sum_{\omega} \mathcal{I}^{\text{KM},\text{f}}(\vec{\mathbf{y}}^{\text{s}}, \omega) \right|. \quad (1.16)$$

Finally, we introduce the functionals

$$\mathcal{I}_J^{\text{KM}}(\vec{\mathbf{y}}^{\text{s}}, \omega) = \sum_{r=1}^N \overline{\widehat{G}(\vec{\mathbf{x}}_r, \vec{\mathbf{y}}^{\text{s}}, \omega)} \sum_{s=1}^N (\sigma_J(\omega) U_J(\omega) V_J^*(\omega))_{rs} \widehat{G}(\vec{\mathbf{x}}_s, \vec{\mathbf{y}}^{\text{s}}, \omega), \quad (1.17)$$

and

$$\mathcal{I}_J^{\text{KM}}(\vec{\mathbf{y}}^{\text{s}}) = \left| \sum_{\omega} \mathcal{I}_J^{\text{KM}}(\vec{\mathbf{y}}^{\text{s}}, \omega) \right|, \quad (1.18)$$

which are derived from (1.15) and (1.16), respectively, when $d_J = 1$ and $d_i = 0$ for all $i \neq J$; in other words, when we consider projection on the single J -th singular vector of the response matrix.

We also introduce selective imaging functionals for $\widetilde{\mathcal{I}}^{\text{KM}}$, as we have done in (1.15)–(1.18), using filtered versions of $\widehat{\mathbb{P}}$. The only thing that changes in this process is the size of the response matrix. Now, we are dealing with an $M \times M$ matrix, where M denotes the number of propagating modes. Specifically, for a single frequency ω , let

$$\widetilde{\mathcal{I}}^{\text{KM},\text{f}}(\vec{\mathbf{y}}^{\text{s}}, \omega) = -\frac{1}{4h^2} \sum_{m,n=1}^M e^{-i(\beta_n + \beta_m)|z_{\text{a}} - z^{\text{s}}|} X_n(x^{\text{s}}) X_m(x^{\text{s}}) \left(D[\widehat{\mathbb{P}}(\omega)] \right)_{mn}, \quad (1.19)$$

while for multi-frequency data we define

$$\widetilde{\mathcal{I}}^{\text{KM},\text{f}}(\vec{\mathbf{y}}^{\text{s}}) = \left| \sum_{\omega} \widetilde{\mathcal{I}}^{\text{KM},\text{f}}(\vec{\mathbf{y}}^{\text{s}}, \omega) \right|. \quad (1.20)$$

Furthermore, we define

$$\widetilde{\mathcal{I}}_J^{\text{KM}}(\vec{\mathbf{y}}^{\text{s}}, \omega) = -\frac{1}{4h^2} \sum_{m,n=1}^M e^{-i(\beta_n + \beta_m)|z_{\text{a}} - z^{\text{s}}|} X_n(x^{\text{s}}) X_m(x^{\text{s}}) \left(\sigma_J(\omega) U_J(\omega) V_J^*(\omega) \right)_{mn}, \quad (1.21)$$

and

$$\widetilde{\mathcal{I}}_J^{\text{KM}}(\vec{\mathbf{y}}^{\text{s}}) = \left| \sum_{\omega} \widetilde{\mathcal{I}}_J^{\text{KM}}(\vec{\mathbf{y}}^{\text{s}}, \omega) \right|, \quad (1.22)$$

where now σ, U, V denote the singular values and vectors of $\widehat{\mathbb{P}}$.

1.4 Numerical experiments

In this section we present numerical experiments for scatterers of various shapes and sizes. In order to construct the array response matrix, which is the data that we need for evaluating the imaging functionals, we solve numerically the wave equation problem (1.1) with appropriate initial and boundary conditions. To this end, we use Montjoie [11], a high-order finite element C++ code developed at INRIA, designed to solve problems arising in wave propagation phenomena, such as acoustic, electromagnetic, aeroacoustic and elastodynamic problems.

We consider a waveguide with depth equal to $D = 200$ m and sound speed $c_0 = 1500$ m/s. The vertical array is placed at $z_a = 40$ m and consists of $N = 39$ transducers uniformly distributed in the water column with a pitch $h = 5$ m, thus spanning the whole depth of the waveguide. Let us note that in Chapter 4 we shall consider the case where the array does not span the whole depth of the waveguide. In such case, the array response matrix may be extracted from the matrix that corresponds to the full aperture array, by removing the appropriate lines and columns.

Point-like sources are simulated by considering the source term in (1.1) to be of the form $f(t, \vec{x}) = h(t)g(\vec{x}; \vec{x}_s)$. Here $h(t)$ is a Ricker function of time, given by

$$h(t) = \sqrt{2}f_0 [1 - 4\pi^2 f_0^2(t - t_c)^2] \exp \left\{ -[\sqrt{2}\pi f_0(t - t_c)]^2 \right\},$$

where f_0 is the central frequency of the pulse and t_c is the time at which the source attains its maximum. In the numerical results that follow, $f_0 = 75$ Hz, $t_c = 0.01$ s and the final computation time is taken equal to $T = 4$ s. The function $g(\vec{x}; \vec{x}_s)$ is a Gaussian, given by $g(\vec{x}; \vec{x}_s) = \sqrt{\alpha/\pi} \exp(-\alpha|\vec{x} - \vec{x}_s|^2)$, where $\alpha = \ln(10^6)/r^2$; r determines the support of the Gaussian and is taken equal to 10 m.

The originally infinite (in the z -direction) domain is truncated by introducing two perfectly matched layers (PML) [21, 22], see Figure 1.2. The one near the source is confined in range in $[-100, 0]$, while the other, far from the source, in $[500, 600]$ (all distances are in meters). We have checked that the width of 100 m for the PML was enough in order to absorb the waves efficiently. The resulting computational domain is discretized with quadrangles

on which the usual basis functions of the \mathbb{Q}_n family ($\mathbb{Q}_n = \text{span}\{x^\ell y^m, 0 \leq \ell, m \leq n\}$) are used. In this work, we will see imaging results for two types of scatterers; a square scatterer and a disc shaped scatterer. We use \mathbb{Q}_8 polynomials for the square scatterer, while for the disc, we use \mathbb{Q}_{12} . Numerical quadrature is based on Gauss-Lobatto rules, and time discretization employs a fourth-order Leapfrog scheme.

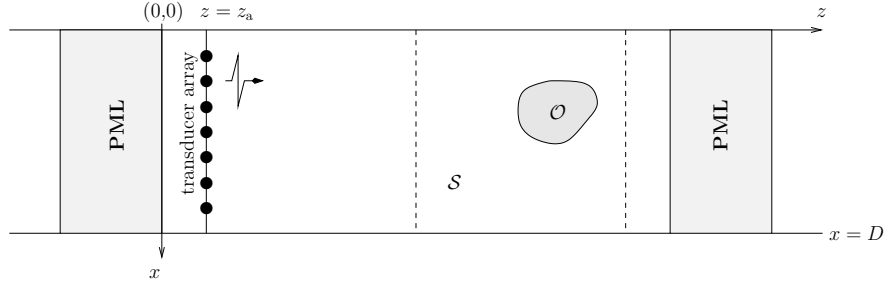


Figure 1.2: Schematic representation of a waveguide truncated near and far from the source with two perfectly matched layers.

In all cases the frequencies that are used are close to a central reference frequency $f_0 = 75$ Hz, for which the corresponding wavelength is equal to $\lambda_0 = 20$ m. In particular, we consider frequencies ranging from 70.5 to 79.5 Hz with an increment of 1 Hz.

In what follows we will examine the performance of the imaging functionals \mathcal{I}^{KM} and $\tilde{\mathcal{I}}^{\text{KM}}$. Let us recall the results for selective imaging with \mathcal{I}^{KM} in free space: it was shown in [4] that information about the edges of a reflector is contained in those singular vectors that correspond to singular values of the response matrix that lie in the intermediate regime between the large ones and zero. In our numerical simulations we observe the same behaviour for imaging in waveguides with $\tilde{\mathcal{I}}^{\text{KM}}$ while this is not the case for \mathcal{I}^{KM} .

Test case 1: Circular scatterer with diameter $\delta = 40$ m

We consider here a circular scatterer with diameter $\delta = 2\lambda_0 = 40$ m centered at (440,100) m. Figure 1.3 depicts the singular values (normalized with respect to the largest one) of the matrices $\hat{\Pi}$ and $\hat{\mathbb{P}}$ for a frequency equal to 75.5 Hz. As expected, only few of the singular values are non-zero.

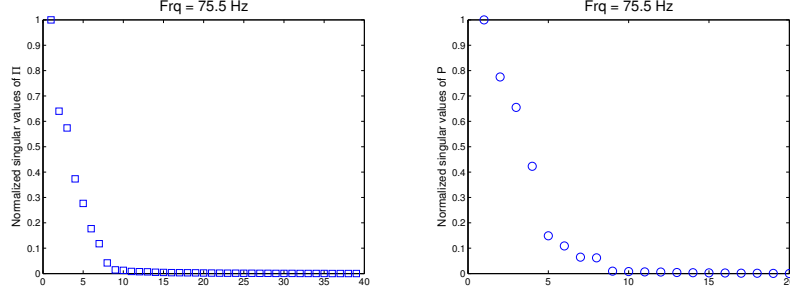


Figure 1.3: Normalized singular values of $\hat{\Pi}$ (left subplot) and $\hat{\mathbb{P}}$ (right subplot) for a circle scatterer with diameter $\delta = 40$ m.

In Figure 1.4 we plot the values of \mathcal{I}^{KM} and $\tilde{\mathcal{I}}^{\text{KM}}$ when the full matrices $\hat{\Pi}$ and $\hat{\mathbb{P}}$, respectively, are used. In both cases we see that the front part of the circle is recovered, although for $\tilde{\mathcal{I}}^{\text{KM}}$ the image is supported mainly around the center of the circle at $x = 100$ m. Let us note here, that while the \mathcal{I}^{KM} image recreates the biggest part of the left side of the circle, we also have oscillations in the image, whose existence is explained in a resolution analysis performed in the Appendix.

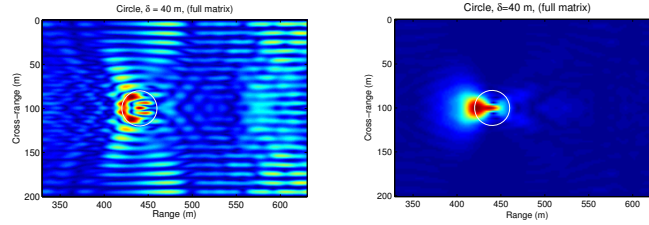


Figure 1.4: \mathcal{I}^{KM} (left subplot) versus $\tilde{\mathcal{I}}^{\text{KM}}$ (right subplot) for a circular scatterer with diameter $\delta = 40$ m.

In Figure 1.5 we present the results of selective imaging with $\mathcal{I}_J^{\text{KM}}$ and $\tilde{\mathcal{I}}_J^{\text{KM}}$ (see (1.18) and (1.22), respectively), for $J = 1, 4$ and 5 . For $J = 1$, $\mathcal{I}_J^{\text{KM}}$ focuses towards the endpoints of the vertical diameter of the circle, while $\tilde{\mathcal{I}}_J^{\text{KM}}$ in the leftmost part of the circle. For $J = 4$, $\mathcal{I}_J^{\text{KM}}$ seems to focus at the two endpoints of the horizontal diameter of the circle and $\tilde{\mathcal{I}}_J^{\text{KM}}$ towards the endpoints of the vertical diameter. For $J = 5$, both $\mathcal{I}_J^{\text{KM}}$ and $\tilde{\mathcal{I}}_J^{\text{KM}}$ seem to locate roughly the boundary of the circle.

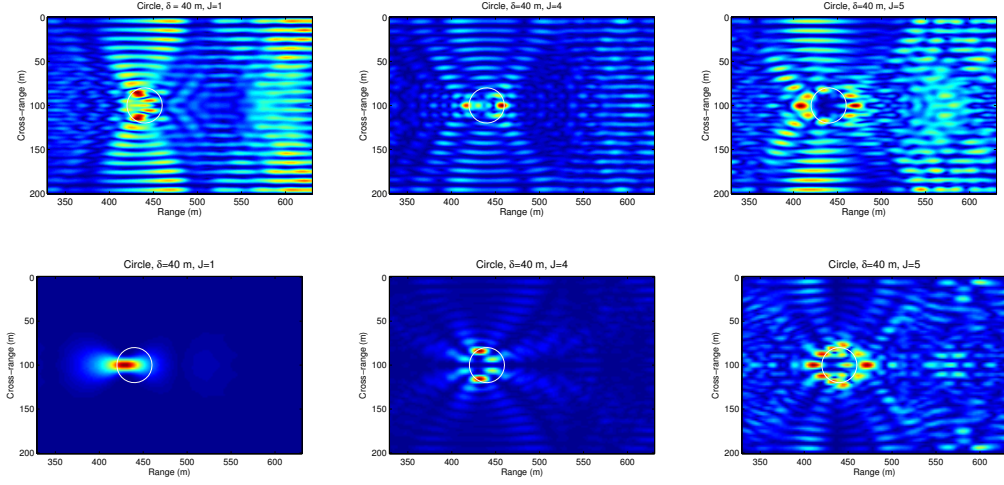


Figure 1.5: $\mathcal{I}_J^{\text{KM}}$ (top row) versus $\tilde{\mathcal{I}}_J^{\text{KM}}$ (bottom row) for a circular scatterer with diameter $\delta = 40$ m. J indicates projection on the J th singular vector. From left to right $J = 1$, $J = 4$ and $J = 5$.

As a first comment, note that selective imaging with $\tilde{\mathcal{I}}^{\text{KM}}$ exhibits the expected behaviour from the free space case (see e.g. [4]), in the sense that the singular vector corresponding to the largest singular value is associated to an image focused at the center of the object, while the ones corresponding to the intermediate singular values carry information about its edges.

Test case 2: Circular scatterer with diameter $\delta = 20$ m for a single frequency

Here we decrease the diameter of the previous circular scatterer to $\delta = \lambda_0 = 20$ m. In Figure 1.6 we plot the values of $|\mathcal{I}_1^{\text{KM}}(\omega)|$ and $|\tilde{\mathcal{I}}_1^{\text{KM}}(\omega)|$ (selective imaging with respect to the first singular vector) for single frequencies of 73 Hz (left column) and 74 Hz (right column). For both frequencies $|\tilde{\mathcal{I}}_1^{\text{KM}}(\omega)|$ focuses towards the leftmost part of the circle, as opposed to $|\mathcal{I}_1^{\text{KM}}(\omega)|$ which focuses towards its edges for $f = 73$ Hz, but in the center for $f = 74$ Hz. This kind of lack of robustness has initially motivated us to work with $\tilde{\mathcal{I}}^{\text{KM}}$ rather than with \mathcal{I}^{KM} .

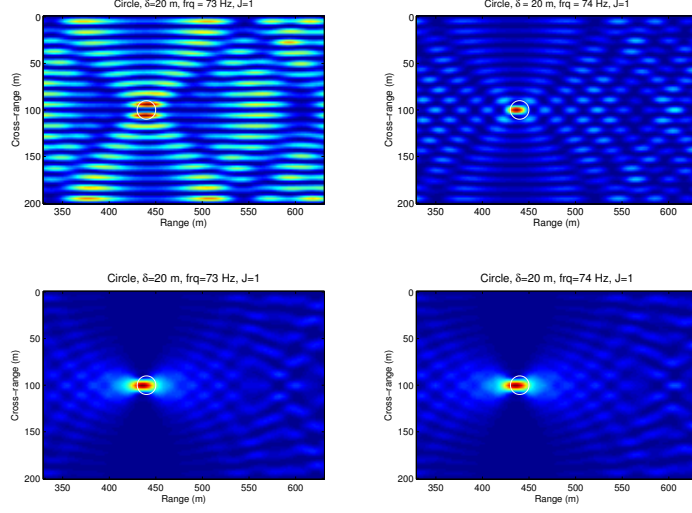


Figure 1.6: $|\mathcal{I}_1^{\text{KM}}(\omega)|$ (top row) versus $|\tilde{\mathcal{I}}_1^{\text{KM}}(\omega)|$ (bottom row) for a circle shaped scatterer with diameter $\delta = 20$ m for single frequencies of 73 Hz (left column) and 74 Hz (right column).

Test case 3: Square scatterer with side length $b = 40$ m

Now, we consider a square scatterer of side length $b = 2\lambda_0 = 40$ m, with its center located at (470,100) m. In this test case we examine the behaviour of $\tilde{\mathcal{I}}^{\text{KM}}$ and its filtered version under the influence of additive noise. In order to simulate measurement noise we proceed as in [4] and add a noise matrix $W(\omega)$ with zero mean uncorrelated Gaussian distributed entries with variance ϵp_{avg} , *i.e.* $W_{r,s}(\omega) \sim \mathcal{N}(0, \epsilon p_{\text{avg}})$. Here the average power received per source, receiver and frequency is given by

$$p_{\text{avg}} = \frac{1}{N^2 N_{\text{freq}}} \sum_{i=1}^{N_{\text{freq}}} \|\hat{\Pi}(\omega_i)\|_{\text{F}}^2,$$

where $\|\cdot\|_{\text{F}}$ is the Frobenius matrix norm and N_{freq} the number of frequencies. The expected power of the noise $W(\omega_i)$ over all frequencies, receivers and sources is

$$\mathbb{E} \left[\sum_{i=1}^{N_{\text{freq}}} \|W(\omega_i)\|_{\text{F}}^2 \right] = \epsilon N^2 N_{\text{freq}} p_{\text{avg}}.$$

Since the total power of the signal received over all frequencies, receivers and sources is $N^2 N_{\text{freq}} p_{\text{avg}}$, the Signal-to-Noise Ratio (SNR) in dB is $-10 \log_{10} \epsilon$.

As before, we use frequencies ranging from 70.5 to 79.5 Hz with an increment of 1 Hz. In Figure 1.7 we plot the singular values of the matrices $\hat{\Pi}$ and $\hat{\mathbb{P}}$ for the frequency of 75.5 Hz (normalized with respect to the largest one) in the absence of noise and for SNR = 10, 0 and -10 dB. Notice that the singular values that are larger than 20% of the largest one in the case of 10 dB SNR remain close to those corresponding to the unperturbed matrices, while noise has a more profound influence in the singular values of 0 dB and -10 dB SNR.

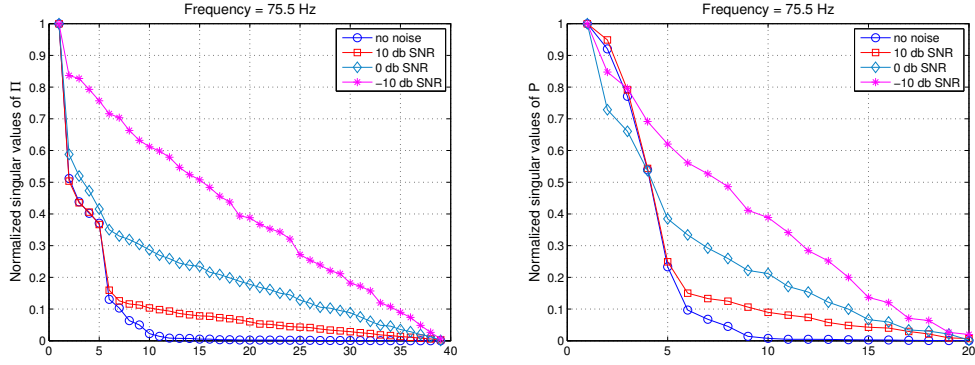


Figure 1.7: Normalized singular values of $\hat{\Pi}$ (left subplot) and $\hat{\mathbb{P}}$ (right subplot) for a square scatterer with side length $b = 40$ m, in the absence of noise and by adding noise with 10, 0 and -10 dB SNR.

In Figure 1.8 we plot the images obtained with $\tilde{\mathcal{I}}^{\text{KM}}$ without using any selective imaging techniques. In all cases the left side of the scatterer is recreated.

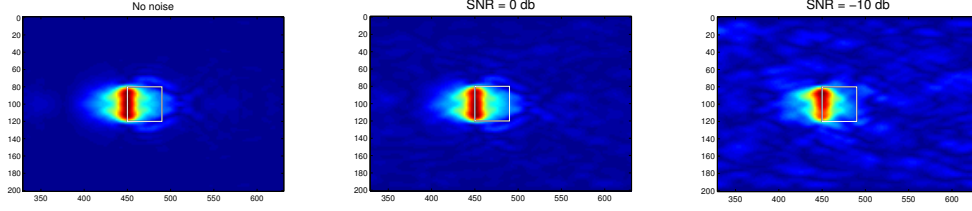


Figure 1.8: $\tilde{\mathcal{I}}^{\text{KM}}$ for $b = 40$ m, $D = 200$ m, $c_0 = 1500$ m/s, $f \in [70.5, 79.5]$ Hz and SNR= $\infty, 0, -10$ dB.

Next, we use filtered versions of the matrix $\hat{\mathbb{P}}$ that employ more than one singular values. These are chosen as follows, [4]:

- a) we normalize the singular values with respect to the largest one,
- b) we determine an interval $[\alpha, \beta] \subset (0, 1)$, and
- c) we include in the filtered version of $\tilde{\mathcal{I}}^{\text{KM},f}$ all the singular values that lie in $[\alpha, \beta]$.

Figures 1.9–1.10 depict the values of $\tilde{\mathcal{I}}^{\text{KM},f}$ without noise included and when noise is included with 0 and -10 dB SNR. We do not show the images with 10 dB SNR because they are essentially the same as the ones without noise. Specifically, in Figure 1.9 we have employed in the computation of $\tilde{\mathcal{I}}^{\text{KM},f}$ the singular values that are between 5% and 60% of the largest one ($[\alpha, \beta] = [0.05, 0.60]$) and in Figure 1.10 we take $[\alpha, \beta] = [0.12, 0.74]$.

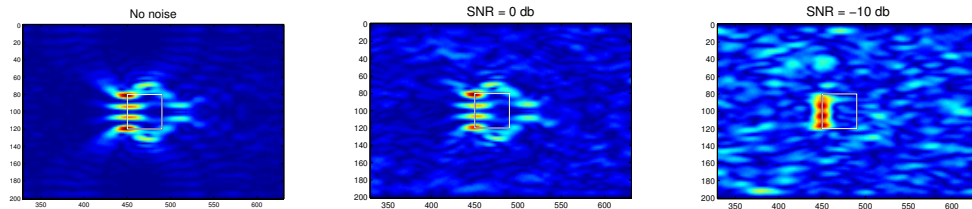


Figure 1.9: Normalized values of $\tilde{\mathcal{I}}^{\text{KM},f}$, for $b = 40$ m, $D = 200$ m, $c_0 = 1500$ m/s, $f \in [70.5, 79.5]$ Hz and SNR= $\infty, 0, -10$ dB, $[\alpha, \beta] = [0.05, 0.60]$.

In both cases the results with 0 dB SNR are qualitatively very similar to those obtained in the absence of noise. Note that even with -10 dB SNR, we are still able to recreate the left side of the object, but the effect of the noise is visible in the image.

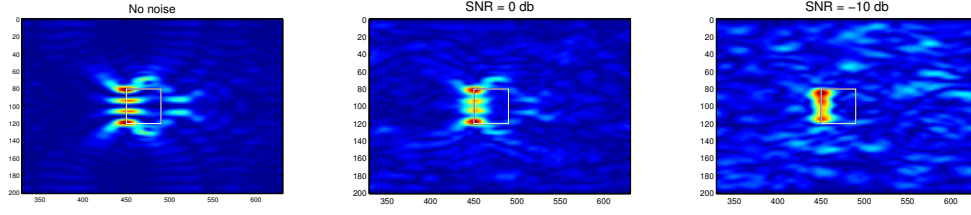


Figure 1.10: Normalized values of $\tilde{\mathcal{I}}^{\text{KM},f}$, for $b = 40$ m, $D = 200$ m, $c_0 = 1500$ m/s, $f \in [70.5, 79.5]$ Hz and SNR = $\infty, 0, -10$ dB, $[\alpha, \beta] = [0.12, 0.74]$.

Chapter 2

A One-Dimensional Model Problem

In this chapter we are going to introduce and study a simplified model problem in order to shed some light to the behaviour of the imaging functionals \mathcal{I}^{KM} and $\tilde{\mathcal{I}}^{\text{KM}}$. Let us turn our attention to the case of the square scatterer (Test Case 3) in Section 1.4. Figures 1.8 and 1.9 suggest that we are able to locate the left side of the square. This motivates us to introduce a one-dimensional vertical mirror as a target, and try to analyze the array response matrix and the imaging functionals in this simpler case. Specifically, we consider the following model problem: In the marine environment described in the beginning of Chapter 1, we assume that the active array passes through the x axis, i.e., the transducers' coordinates are $(0, x_i)$, $x_i = ih$, $1 \leq i \leq N$, where $h := D/(N + 1)$ is the pitch. The target, denoted by \mathcal{T} , is assumed to be a vertical one-dimensional perfect reflector, i.e., a 'crack' of width b , located at range $z = L$. The center of the target is denoted by $\vec{y}^* = (L, x_0)$. Let us also denote by \mathcal{C} the vertical section of the waveguide at range $z = L$, i.e., $\mathcal{C} := \{(L, x) : 0 \leq x \leq D\}$. This setup is schematically depicted in Figure 2.1 and aims at simulating the left side of a square scatterer. We refer to [23] for an analogous setup used to analyze the response matrix for extended targets in the free space.

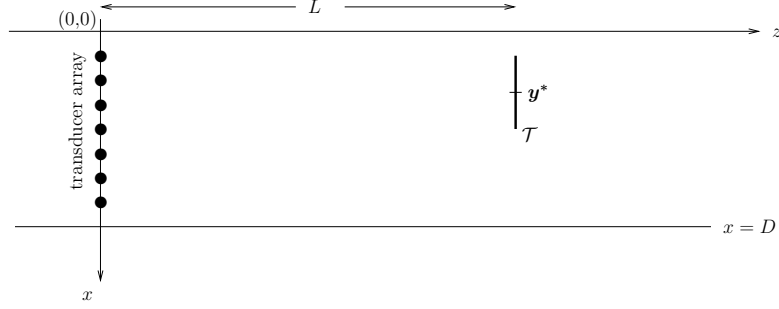


Figure 2.1: A vertical crack, implemented in the waveguide.

2.1 Properties of the array response matrix

Assuming unit reflectivity at each point of the target we may approximate the response in a receiver placed at $\vec{x}_r = (0, x_r)$ due to a source at $\vec{x}_s = (0, x_s)$, $r, s \in \{1, 2, \dots, N\}$, as

$$\hat{\Pi}(\vec{x}_r, \vec{x}_s, \omega) = \int_{\mathcal{T}} \hat{G}(\vec{y}, \vec{x}_r) \hat{G}(\vec{y}, \vec{x}_s) dx, \quad (2.1)$$

where $\vec{y} = (L, x)$, $x \in [x_0 - b/2, x_0 + b/2]$, and \hat{G} is the Green's function defined in (1.5). For future reference, let us also recall that μ_n , X_n are the eigenvalues and corresponding eigenfunctions of the operator $-d^2/dx^2$ in $H^2(0, D) \cap H_0^1(0, D)$, defined in (1.3), and β_n are the horizontal wavenumbers defined in (1.4).

Inserting (1.5) into (2.1) shows that

$$\hat{\Pi}(\vec{x}_r; \vec{x}_s, \omega) = -\frac{1}{4} \sum_{m,n=1}^{\infty} \frac{e^{i\beta_m L}}{\beta_m} X_m(x_s) X_n(x_r) \frac{e^{i\beta_n L}}{\beta_n} \int_{x_0 - \frac{b}{2}}^{x_0 + \frac{b}{2}} X_m(x) X_n(x) dx. \quad (2.2)$$

Moreover, let $g_m(x_i) := \frac{i}{2} \frac{e^{i\beta_m L}}{\beta_m} X_m(x_i) = \left(\hat{G}(\cdot, \vec{x}_i), X_m \right)_{L^2(\mathcal{C})}$, where the outer parentheses in the second equality denote the standard L^2 inner product on \mathcal{C} . Let us also define \mathcal{G} to be the matrix

$$\mathcal{G} := \begin{pmatrix} g_1(x_1) & g_2(x_1) & \dots & g_M(x_1) & g_{M+1}(x_1) & \dots \\ g_1(x_2) & g_2(x_2) & \dots & g_M(x_2) & g_{M+1}(x_2) & \dots \\ \vdots & \vdots & & \vdots & \vdots & \\ g_1(x_N) & g_2(x_N) & \dots & g_M(x_N) & g_{M+1}(x_N) & \dots \end{pmatrix}$$

and A_{inf} the (infinite) matrix with entries

$$a_{mn} = \int_{x_0 - \frac{b}{2}}^{x_0 + \frac{b}{2}} X_m(x) X_n(x) dx, \quad m, n = 1, 2, \dots \quad (2.3)$$

Then, using (2.2), we may write the array response matrix $\hat{\Pi}$ as a matrix product of the form

$$\hat{\Pi} = \mathcal{G} A_{\text{inf}} \mathcal{G}^T. \quad (2.4)$$

We point out that if L is sufficiently large and $m \geq M + 1$, then

$$g_m(x_i) = \frac{i}{2} \frac{e^{i\beta_m L}}{\beta_m} X_m(x_i) = \frac{1}{2} \frac{e^{-\sqrt{\mu_n - k^2} L}}{\sqrt{\mu_n - k^2}} X_m(x_i) \simeq 0,$$

or, equivalently, only the principal $N \times M$ part of \mathcal{G} is practically non-zero; thus, in practice, instead of A_{inf} we work with its $M \times M$ principal part denoted by A_M . At this point let us remark that although $\hat{\Pi}$ is associated with A_{inf} (and, in practice, with A_M) through (2.4), we cannot infer from this formula an explicit relation between their singular values.

It is now natural to ask how A_M is related to the matrix $\hat{\mathbb{P}}$ that results when we project the array response matrix $\hat{\Pi}$ on the propagating modes. Recalling the definition of $\hat{\mathbb{P}}$ (1.13), and using the orthonormality of the eigenfunctions $\{X_n\}_{n=1,2,\dots}$, one may immediately see that

$$\hat{\mathbb{P}}_{mn} = -\frac{1}{4} e^{i(\beta_m + \beta_n)L} a_{mn}, \quad m, n = 1, \dots, M, \quad (2.5)$$

or, in matrix form,

$$\hat{\mathbb{P}} = -\frac{1}{4} Q A_M Q, \quad (2.6)$$

where Q is the diagonal matrix $\text{diag}(e^{i\beta_1 L}, \dots, e^{i\beta_M L})$. Hence $\hat{\mathbb{P}}$ is unitarily equivalent to A_M , since $Q^* Q = I$, therefore the spectral properties of $\hat{\mathbb{P}}$ are determined by those of the real symmetric matrix A_M .

In what follows, for an arbitrary positive integer n we shall denote by A_n the principal $n \times n$ submatrix of A_{inf} , and we will refer to either the eigenvalues/eigenvectors of A_n or to its singular values/vectors, since the latter are just the former written in descending order.

For $\ell, m \geq 1$, and in view of the simple trigonometric identity $2 \sin a \sin b = \cos(a - b) - \cos(a + b)$, it holds that

$$\begin{aligned} a_{\ell m} &= \int_{x_0 - \frac{b}{2}}^{x_0 + \frac{b}{2}} X_\ell(x) X_m(x) dx = \frac{2}{D} \int_{x_0 - \frac{b}{2}}^{x_0 + \frac{b}{2}} \sin \frac{\ell \pi x}{D} \sin \frac{m \pi x}{D} dx \\ &= \frac{1}{D} \int_{x_0 - \frac{b}{2}}^{x_0 + \frac{b}{2}} \cos \frac{(\ell - m) \pi x}{D} dx - \frac{1}{D} \int_{x_0 - \frac{b}{2}}^{x_0 + \frac{b}{2}} \cos \frac{(\ell + m) \pi x}{D} dx. \end{aligned}$$

Hence

$$A_n = T_n - H_n, \quad \text{where } T_n := (t_{\ell-m})_{\ell,m=1}^n, \quad H_n := (t_{\ell+m})_{\ell,m=1}^n,$$

and

$$t_m = \frac{1}{D} \int_0^D \mathbb{1}_{\mathcal{T}}(x) \cos \frac{m \pi x}{D} dx, \quad (2.7)$$

where $\mathbb{1}_{\mathcal{T}}(x)$ is the indicator function of \mathcal{T} and A_n is the principal $n \times n$ submatrix of A_{inf} . Note that $\mathbb{1}_{\mathcal{T}}(x)$ is the so called *generating function* of the matrices A_n , T_n and H_n . One may immediately recognise T_n as a (real symmetric) Toeplitz matrix, i.e., a matrix with constant entries along the diagonals, and H_n as a Hankel matrix, i.e., a matrix with constant skew-diagonals (these are the diagonals that are perpendicular to the main diagonal). Hence A_n has a special structure: It is a *Toeplitz-minus-Hankel* matrix.

As we shall briefly discuss next, the spectral properties of A_n are determined by the Toeplitz part T_n . This can be seen, for example, by modifying appropriately the proofs in the work of Fasino [24], who studies the spectral properties of Toeplitz-plus-Hankel matrices, or by tracing back to the work of Trench [25], who studies the spectral properties of the *real symmetric Toeplitz* matrix

$$T_n = (t_{r-s})_{r,s=1}^n, \quad \text{where } t_r = \frac{1}{\pi} \int_0^\pi f(x) \cos rx \, dx,$$

and the generating function $f \in L^2[0, \pi]$. Following Trench's notation, a vector $\mathbf{x} \in \mathbb{R}^n$ is called *symmetric* if $J\mathbf{x} = \mathbf{x}$ and *skew-symmetric* if $J\mathbf{x} = -\mathbf{x}$, where J is the flip matrix (i.e. the matrix that has ones on the secondary diagonal and zeros elsewhere); see also [26]. Moreover, an eigenvalue λ of T is defined to be *even* (*odd*) if T has a symmetric (skew-symmetric) λ -eigenvector.

Now, let $\lambda_1^{(n)} \leq \lambda_2^{(n)} \leq \dots \leq \lambda_n^{(n)}$ be the eigenvalues of T_n , and let $\nu_1^{(n)} \leq \nu_2^{(n)} \leq \dots \leq \nu_n^{(n)}$ be the eigenvalues of A_n . Since, in our case, the generating function f of the matrices A_n , T_n , and H_n , is the indicator function of \mathcal{T} , its essential lower and upper bounds are simply 0 and 1, respectively. A result of Szegő [27, pp. 64-65], guarantees that (i) $0 \leq \lambda_i^{(n)} \leq 1$ for all $i = 1, \dots, n$; (ii) for any fixed integer k , $\lambda_k^{(n)} \rightarrow 0$, $\lambda_{n-k}^{(n)} \rightarrow 1$ as $n \rightarrow \infty$; and (iii) if G is any continuous function defined in $[0, 1]$, we have

$$\lim_{n \rightarrow \infty} \frac{1}{n} \sum_{i=1}^n G(\lambda_i^{(n)}) = \frac{1}{D} \int_0^D G(f(x)) dx. \quad (2.8)$$

Moreover, the following theorem specializes results stated in [25] to our case, where we work on $[0, D]$, the entries of our matrix are given in (2.7), and $f = \mathbb{1}_{\mathcal{T}}$.

Theorem 1 (a) *The odd eigenvalues $\kappa_1^{(2n+1)} \leq \kappa_2^{(2n+1)} \leq \dots \leq \kappa_n^{(2n+1)}$ of T_{2n+1} are the eigenvalues of A_n [25, Thm. 2].*

(b) *Since f is bounded, the sets $\{\lambda_i^{(n)}\}_{i=1}^n$ and $\{\kappa_i^{(2n+1)}\}_{i=1}^n$ are absolutely equally distributed [25, Def. 1, Th. 5].*

(c) *Since f is bounded, (2.8) also holds for $\nu_i^{(n)}$ instead of $\lambda_i^{(n)}$. Moreover, if for $\epsilon > 0$ $C(\epsilon, 1 - \epsilon, n)$ is the cardinality of the set $\{i : \epsilon \leq \kappa_i^{(2n+1)} \leq 1 - \epsilon\}$, then*

$$\lim_{n \rightarrow \infty} \frac{1}{n} C(\epsilon, 1 - \epsilon, n) = 0$$

[25, Lem. 2 and Thm. 6].

Summarizing, the eigenvalues of the matrix A_n (which are the odd eigenvalues of T_{2n+1}) are clustered near 0 and 1, and considering the function G to be the identity on $[0, 1]$, we immediately see that

$$\lim_{n \rightarrow \infty} \frac{1}{n} \sum_{i=1}^n \nu_i^{(n)} = \frac{1}{D} \int_0^D \mathbb{1}_{\mathcal{T}}(x) dx = \frac{b}{D}.$$

This indicates that asymptotically, as $n \rightarrow \infty$, the ratio of the nonzero eigenvalues of A_n to the total number of eigenvalues is equal to b/D . In our case, where n is equal to the number of propagating modes $M = \lfloor \frac{2D}{\lambda} \rfloor$, it is

expected that the number of ‘significant’ singular values for our matrix A_M is

$$\left\lceil M \frac{b}{D} \right\rceil \approx \left\lceil \frac{2b}{\lambda} \right\rceil. \quad (2.9)$$

Moreover, if $\mathbf{u} = (u_1, \dots, u_M)^T$ is an orthonormal eigenvector of A_M that corresponds to an eigenvalue λ , then $\mathbf{v} = \frac{1}{\sqrt{2}}(\mathbf{u}, 0, -J\mathbf{u})^T$ is an orthonormal skew-symmetric λ -eigenvector of T_{2M+1} and vice versa.

To conclude, we have shown that the number of nonzero singular values is related to the size of the object. In particular, by performing a standard resolution analysis, one may deduce that the cross-range resolution is $\lambda/2$, therefore the rank of the matrix is roughly equal to the size of the object divided by the “array resolution.” The same result has been obtained in the free space case (see [4, §4.5.2]).

In the next subsection we explore the form of the eigenvectors of A_M in order to gain some insight about the behaviour of the functionals that we are using for selective imaging.

2.1.1 Selective imaging for the model problem

Next, we explore the form of the singular vectors of A_M . To this end, we consider the imaging functional $\tilde{\mathcal{I}}_J^{\text{KM}}$, where the subscript J indicates that the matrix $\hat{\mathbb{P}}$ is approximated by means of the J -th singular vector for selective imaging. Then, for a search point $\vec{\mathbf{y}}^s = (L, x^s)$ located at the correct range L , (1.21) and (2.5) imply that

$$\tilde{\mathcal{I}}_J^{\text{KM}}(\vec{\mathbf{y}}^s) = \frac{1}{16h^2} \sum_{m,n=1}^M X_m(x^s) X_n(x^s) \sigma_J u_J^m u_J^n = \sigma_J \left(\frac{1}{4h} \sum_{n=1}^M u_J^n X_n(x^s) \right)^2, \quad (2.10)$$

where $\mathbf{u}_J = (u_J^1, u_J^2, \dots, u_J^M)^T$ is the singular vector of A_M that corresponds to the singular value σ_J . Recalling the definition of X_n in (1.3), and suppressing constants, we associate to \mathbf{u}_J the trigonometric polynomial

$$s_J(x) = \sum_{n=1}^M u_J^n \sin \frac{n\pi x}{D}. \quad (2.11)$$

Therefore, the behaviour of $\tilde{\mathcal{I}}_J^{\text{KM}}$ is in fact determined by the properties of $s_J(x)$, that we shall illustrate in the following example: Consider a waveguide

with depth equal to $D = 200$ m and constant sound speed equal to $c_0 = 1500$ m/s. In Figure 2.2 (left subplot) we plot the singular values of A_M for a frequency of 74 Hz, for which the number of propagating modes $M = 19$, the wavelength $\lambda \approx 20.27$ m, and \mathcal{T} is centered at $x_0 = 70$ m while its width is taken equal to $b = 40$ m $\approx 2\lambda$. According to (2.9) the number of ‘significant’ singular values equals 4. Indeed, one may see that the first three remain very close to 1, the fourth one is approximately 0.65 and the fifth lies in the transition layer between 0 and 1 close to 0.3. The sixth one is less than 0.1 while the rest are very close to zero. In the right subplot of Figure 2.2 we plot

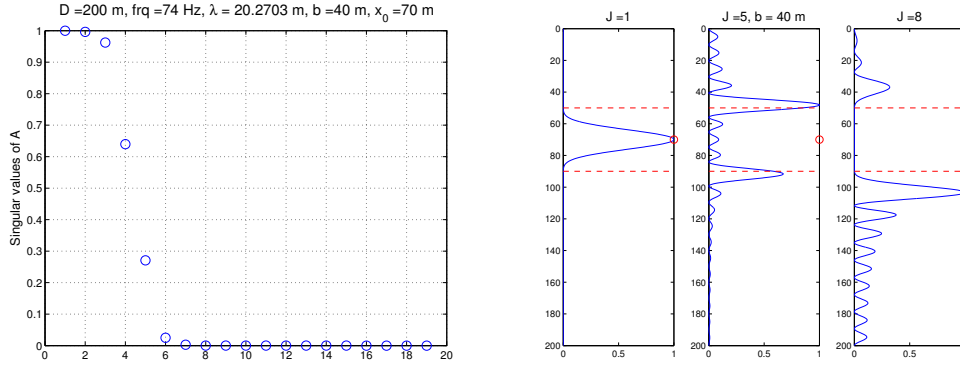


Figure 2.2: Left: The singular values of A_M ($M = 19$). Right: The graphs of $(s_J(x))^2$, $x \in [0, 200]$, for $J = 1, 5, 8$, normalized with respect to their largest values.

the square of the values of the trigonometric polynomials $s_J(x)$ for $J = 1, 5$ and 8, normalized with respect to their largest values. The relevant singular vectors \mathbf{u}_J , $J = 1, 5, 8$ have been computed with MATLAB. The red circle in these figures indicates the center x_0 of \mathcal{T} and the red dashed lines the width b . Note that $s_1(x)$ that corresponds to the first singular value is supported in \mathcal{T} and exhibits a peak at the center x_0 , $s_5(x)$ exhibits peaks near the endpoints of \mathcal{T} , while $s_8(x)$ is approximately zero for $x \in \mathcal{T}$. These remind us the spectral properties and the band-limited behaviour of the so called *prolate matrix*, see [16, 28, 29]. As remarked in [29] for the prolate matrix, one may characterize the eigenspace corresponding to the eigenvalue cluster near 1 as the *signal subspace*, the eigenspace corresponding to the eigenvalue cluster near 0 as the *noise subspace* and the eigenspace corresponding to eigenvalues

in the intermediate layer as the *transient subspace*; the terminology is adopted from [29].

In the following sections we shall investigate further the properties of the eigenvectors of the matrix A_M , depending on the position of the target \mathcal{T} , and their relation with the behaviour of the imaging functional $\tilde{\mathcal{I}}^{\text{KM}}$.

2.2 Spectral properties of A_M (revisited)

For notational convenience let us denote the upper and lower endpoints of the crack \mathcal{T} as

$$\alpha = x_0 - \frac{b}{2} \quad \text{and} \quad \beta = x_0 + \frac{b}{2},$$

respectively. Then, of course, $b = \beta - \alpha$ and $x_0 = (\alpha + \beta)/2$. Moreover, the entries of the matrix A_M , defined in (2.3), may be written explicitly in the form

$$\begin{aligned} a_{mn} = & \frac{1}{(m-n)\pi} \left(\sin \frac{(m-n)\pi\beta}{D} - \sin \frac{(m-n)\pi\alpha}{D} \right) \\ & - \frac{1}{(m+n)\pi} \left(\sin \frac{(m+n)\pi\beta}{D} - \sin \frac{(m+n)\pi\alpha}{D} \right). \end{aligned}$$

The first part of this difference corresponds to the Toeplitz matrix T , while the second to the Hankel matrix H .

Now, let $\mathbf{u} = (u_1, u_2, \dots, u_{2M+1})^T$ be a μ -eigenvector of the $(2M+1) \times (2M+1)$ Toeplitz matrix T_{2M+1} . Then

$$\begin{aligned} & \sum_{n=1}^{2M+1} T_{mn} u_n = \mu u_m, \quad m = 1, 2, \dots, 2M+1 \\ \Leftrightarrow & \sum_{n=1}^{2M+1} \frac{1}{(m-n)\pi} \left(\sin \frac{(m-n)\pi\beta}{D} - \sin \frac{(m-n)\pi\alpha}{D} \right) u_n = \mu u_m. \end{aligned} \quad (2.12)$$

Letting

$$y_n = \frac{\lambda(n - (M+1))}{D} \quad \text{and} \quad x_m = \frac{\lambda(m - (M+1))}{D}$$

we may interpret the sum (2.12) as a Riemann sum over $(-1, 1)$, thus (2.12) may be seen as an approximation of the following integral equation

$$\int_{-1}^1 \frac{1}{\pi(x-y)} \left[\sin\left(\frac{2\pi\beta}{\lambda}(x-y)\right) - \sin\left(\frac{2\pi\alpha}{\lambda}(x-y)\right) \right] u(y) dy = \mu u(x). \quad (2.13)$$

In the following paragraphs we examine the properties of (2.13), i.e. properties of the eigenvalues and eigenfunctions of the integral operator

$$\mathcal{K}_1 u(x) = \int_{-1}^1 \frac{\sin(\tilde{\beta}(x-y)) - \sin(\tilde{\alpha}(x-y))}{\pi(x-y)} u(y) dy, \quad (2.14)$$

where $\tilde{\alpha} = 2\pi\alpha/\lambda$ and $\tilde{\beta} = 2\pi\beta/\lambda$, and the way they depend on the position of the crack in the waveguide.

2.2.1 A crack with an endpoint fixed on the surface

In this case we have $\alpha = 0$ and $\beta = b$. Therefore the Toeplitz part of the matrix A_M is the prolate matrix, and the Toeplitz matrix T_{2M+1} has entries $t_{mn} = t_{m-n}$, $m, n = 1, 2, \dots, 2M+1$, where

$$t_0 = \frac{\tilde{\beta}}{\pi} = \frac{2b}{\lambda}, \quad t_j = \frac{\sin(\tilde{\beta}j)}{\pi j} = \frac{\sin(\frac{2\pi b}{\lambda}j)}{\pi j}, \quad j = 1, 2, \dots, 2M.$$

Moreover, the integral operator defined in (2.14) takes the special form

$$\mathcal{K}_2 u(x) = \int_{-1}^1 \frac{\sin(\tilde{\beta}(x-y))}{\pi(x-y)} u(y) dy, \quad \text{where } \tilde{\beta} = \frac{2\pi b}{\lambda}. \quad (2.15)$$

A great deal of information about the spectrum of \mathcal{K}_2 is contained in a series of outstanding papers by Slepian, Pollak and Landau, [12, 13, 14, 15, 16], where they have studied the so-called concentration problem. (This, in short, amounts to determine those signals in $L^2(-\infty, \infty)$ that retain their largest fraction of energy, when they are first ‘time limited’ and then ‘band limited’.)

Specifically, for $\tilde{\beta}$ large enough, the spectrum of \mathcal{K}_2 is known to consist of three parts:

- Approximately $2\tilde{\beta}/\pi = 4b/\lambda$ eigenvalues are close to 1,
- order $\log(\tilde{\beta})$ eigenvalues decay very fast from 1 to 0,

- and the rest remain very close to zero.

Keeping in mind that the *odd* eigenvalues of the matrix T_{2M+1} are the eigenvalues of the matrix A_M , we recover the results described in Section 2.1.

A remarkable fact is that the eigenfunctions of (2.15), $\psi_0, \psi_1, \dots, \psi_n, \dots$, which form a complete orthonormal basis in $L^2[-1, 1]$, turn out to be the well-known *prolate spheroidal wave functions* (PSWFs). To be precise, the differential eigenvalue problem

$$\mathcal{L}\psi(x) = \frac{d}{dx} \left[(1-x^2) \frac{d\psi(x)}{dx} \right] - \tilde{\beta}^2 x^2 \psi(x) = -\chi \psi(x), \quad (2.16)$$

is such that the operators \mathcal{L} and \mathcal{K}_2 commute, i.e. $\mathcal{L}\mathcal{K}_2 = \mathcal{K}_2\mathcal{L}$, and they have an identical complete set of eigenfunctions $\{\psi_n\}_{n \geq 0}$ in $L^2(-1, 1)$. Moreover, using (2.15) to extend naturally each $\psi_n(x)$, for $x \notin [-1, 1]$, one may show that the set $\{\psi_n\}_{n \geq 0}$ is orthogonal on $(-\infty, \infty)$ as well as on $(-1, 1)$.

In what follows we give some of the basic properties of the PSWFs $\psi_n(x)$ and the eigenvalues μ_n :

$$\begin{aligned} \mu_0 &> \mu_1 > \mu_2 > \dots, \\ \psi_n(x) &\text{ is even or odd with } n, \\ \psi_n(x) &\text{ has exactly } n \text{ zeros in } (-1, 1), \end{aligned} \quad (2.17)$$

$$\begin{aligned} \psi_n(x) &\sim k_n \frac{\sin \tilde{\beta} x}{x}, \text{ as } x \rightarrow \infty, \\ \int_{-1}^1 e^{-2\pi i x t} \psi_n(t) dt &= a_n \psi_n(2\pi x / \tilde{\beta}), \quad -\infty < x < \infty, \end{aligned} \quad (2.18)$$

where k_n and a_n are independent of x . The dependence of $\psi_n(x)$ and μ_n on the parameter $\tilde{\beta}$ is of particular interest. In Figure 2.3, we see the eigenvalues μ_n in the top row and in the bottom row the amplitude of the function $\psi_4(x)$ for $\tilde{\beta} = 5, 10, 20, 30$. We observe that for $\tilde{\beta} = 5$ that $\mu_4 < 1$ which means that the eigenfunction is not fully concentrated inside our interval $(-1, 1)$ and this is apparent by the corresponding plot of ψ_4 . For $\tilde{\beta} = 10, 20, 30$ we see that all the energy of ψ_4 is contained within our interval. Note here that there are 4 zeros of ψ_4 in our interval, in accordance with (2.17) and as $\tilde{\beta}$ increases the zeros move closer to the origin.

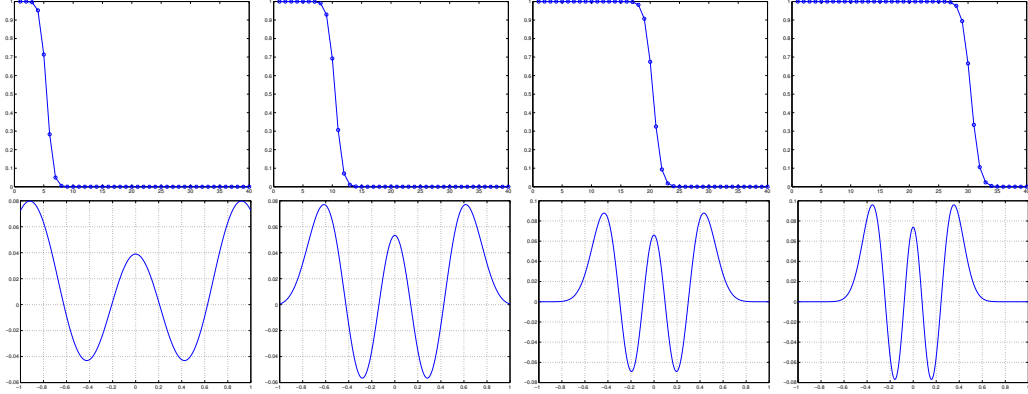


Figure 2.3: Eigenvalues μ_n (top) and values of the eigenfunction $\psi_4(x)$, for $\tilde{\beta} = 5, 10, 20, 30$.

Now, let us go back to the discrete case and recall that the Toeplitz matrix T_{2M+1} is exactly the prolate matrix, while the eigenvalues of A_M are the *odd* eigenvalues of T_{2M+1} . Moreover, if $\mathbf{v} = \frac{1}{\sqrt{2}}(\mathbf{u}, 0, -J\mathbf{u})^T$ is an orthonormal *skew-symmetric* eigenvector of T_{2M+1} corresponding to an odd eigenvalue of T_{2M+1} , then $\mathbf{u} = (u_1, \dots, u_M)^T$ is an orthonormal eigenvector of A_M .

In Figure 2.4, we plot the *odd* eigenvalues and the first four *odd* eigenvectors of T_{2M+1} . The eigenvectors of \mathcal{T}_{2M+1} are the discrete prolate spheroidal sequences $\psi^{(k)}$, and we compute them using the MATLAB function `dpss`.

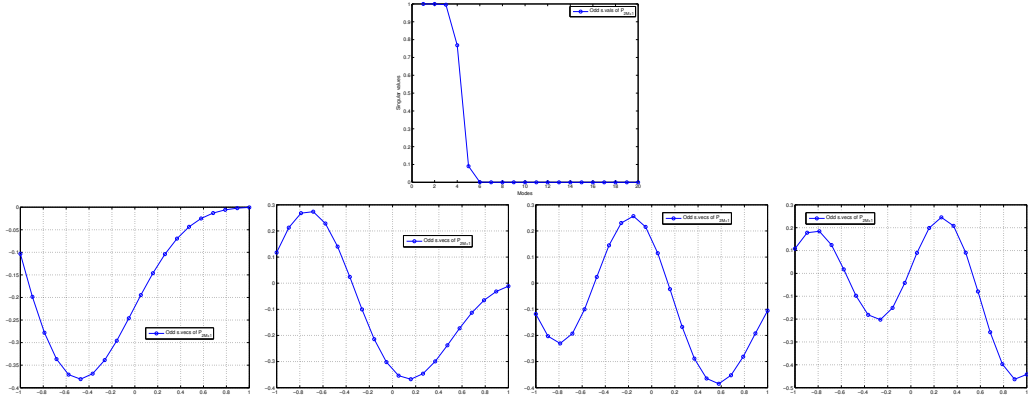


Figure 2.4: Odd eigenvalues (top) and the first four odd eigenvectors (bottom) of T_{2M+1} .

2.2.2 A crack with endpoints $\alpha, \beta \in (0, D]$, ($\alpha < \beta$)

In this general case instead of having the integral operator \mathcal{K}_2 defined in (2.15) we have to deal with \mathcal{K}_1 , see (2.14). Then, it cannot be found, in general, a nice second or fourth order differential operator with polynomial coefficients that commutes with \mathcal{K}_1 , []. Nevertheless, \mathcal{K}_1 is a compact, symmetric, positive definite operator from $L^2[-1, 1]$ to $L^2[-1, 1]$, cf. [], hence it has countably many positive eigenvalues (possibly degenerate)

$$\nu_0 \geq \nu_1 \geq \dots \geq \nu_n \geq \dots \rightarrow 0,$$

and its corresponding orthonormal eigenfunctions are complete in $L^2[-1, 1]$. On the other hand, we cannot any more identify them as PSWFs.

In the case where the crack is placed symmetrically in the middle of the waveguide, i.e., $x_0 = D/2$, we use the identity $\sin a - \sin b = 2 \sin \frac{a-b}{2} \cos \frac{a+b}{2}$ to show that the entries of the Toeplitz matrix T_{2M+1} are

$$T_{mn} = \frac{2}{(m-n)\pi} \sin \frac{(m-n)\pi b}{2D} \cos(m-n) \frac{\pi}{2}.$$

Consider the prolate matrix \mathcal{P} with entries $\mathcal{P}_{mn} = p_{m-n}$, where

$$p_0 = 2w \quad \text{and} \quad p_k = \frac{\sin(2\pi w k)}{pk}, \quad k = 1, 2, \dots, \quad \text{for } w = \frac{b}{2D}.$$

Note that the entries of T_{2M+1} are equal to the corresponding ones of \mathcal{P}_{2M+1} multiplied by the term $\cos(m-n) \frac{\pi}{2}$, which takes the values $0, \pm 1$ depending on the diagonal we are looking at.

In Figure 2.5, we compare the eigenvalues and corresponding eigenvectors of A_M (blue circles) with the odd ones of \mathcal{P}_{2M+1} (red asterisks). Now, we see that the eigenvalues are different, something that did not happen in the previous case, while the eigenvectors of A_M seem to have no apparent similarities to those of \mathcal{P}_{2M+1} .

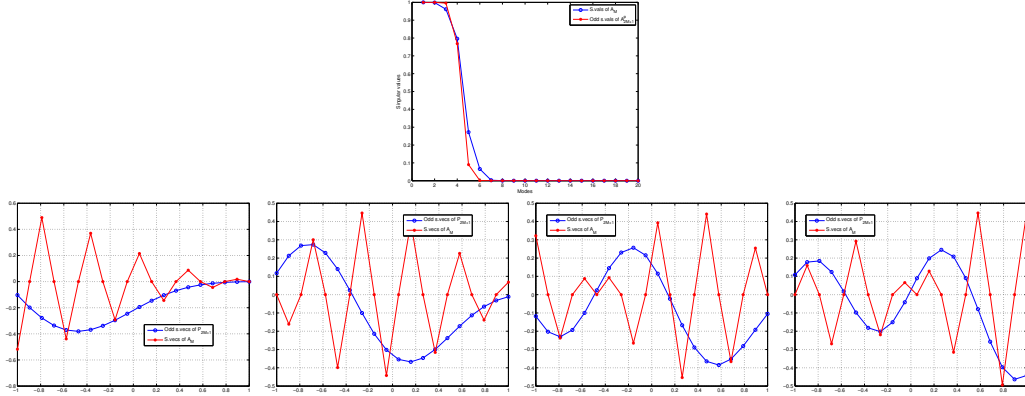


Figure 2.5: Comparison of eigenvalues (top) and the first four eigenvectors (bottom) of A_M (blue circles) vs. the first four odd eigenvectors of \mathcal{P}_{2M+1} (red asterisks).

2.3 Selective imaging for the model problem revisited

In Section 2.1.1, we have associated the eigenvectors of A_M with the trigonometric polynomial

$$s_J(x) = \sum_{n=1}^M u_J^n X_n(x) = \sqrt{\frac{2}{D}} \sum_{n=1}^M u_J^n \sin \frac{n\pi x}{D}, \quad (2.19)$$

and observed that their behavior is similar to the prolate spheroidal wave functions. Next, in Section 2.2.1 we saw that in the special case where the crack is adjacent to the surface of the waveguide we may identify the eigenvectors u_J of the matrix A_M as the M -first coordinates of the eigenvectors of the *prolate* matrix \mathcal{P}_{2M+1} .

Seeing as the vertical eigenfunctions X_n are a base of $[0, D]$, we may see equation (2.19) as a projection of the u_J^n on a different base. Note also that we have a finite sum, which means that the tail of the series will determine our error in the approximation. In Figure 2.6 we see a comparison between the prolate spheroidal wave functions $\psi_0(x), \psi_1(x), \psi_2(x), \psi_3(x)$ and the restriction on the crack of the trigonometric polynomials $s_1(x), s_2(x), s_3(x), s_4(x)$ as described in equation (2.19), for a crack fixed on the top of the waveguide.

We have shifted the calculation of the s_J 's in the interval $[-1, 1]$ in order to compare them properly with the ψ_J 's. We see that the trigonometric polynomials $s_J(x)$ are indeed similar to the prolate spheroidal wave functions and we attribute their discrepancy to the finite sum in our expression.

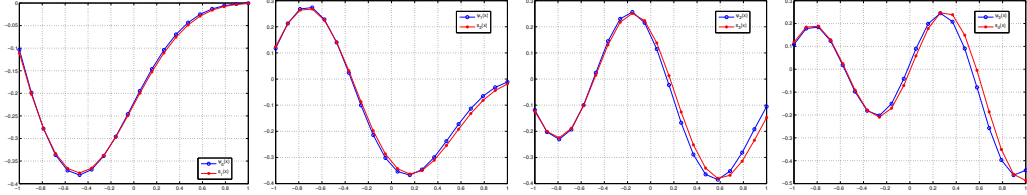


Figure 2.6: The first four prolate spheroidal wave functions (blue circles) and the first four trigonometric polynomials (red asterisks).

In Figure 2.7, we now plot the first four trigonometric polynomials s_J , for a crack that is centered at $x_0 = 73$ with a blue line, for $x_0 = 100$ m with a red line and $x_0 = 143$ m with a black line. We have shifted all our results to $[-1, 1]$, similar to what we have done previously. Here, we see that even though in these cases we do not recover the discrete PSWFs, we still have the prolate-like behavior in our image. It also interesting to note that while the positions of the crack differ a lot, we have good agreement for the s_J . We see that for $x_0 = 73$ m and $x_0 = 143$ m the polynomials have very good agreement, with only the case where the crack is centered in the middle of the waveguide having slight differences.

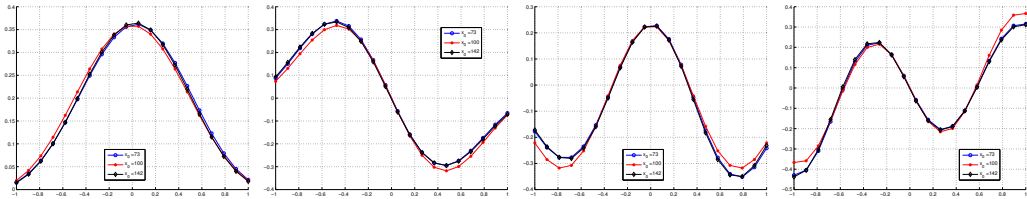


Figure 2.7: The first four trigonometric polynomials for $x_0 = 73$ m (blue circles), $x_0 = 100$ m (red asterisks) and $x_0 = 143$ m (black rhombi) for $f = 75.5$ Hz.

Next, we review the steps that we have followed in [1] in order to gain some insight regarding the form of the singular vectors (eigenvectors) of A_M , and

of the related trigonometric polynomial $s_J(x)$. To this end, we consider an orthonormal basis $\{Y_j(x)\}_{j=1}^\infty$ of $L^2[x_0-b/2, x_0+b/2]$; specifically, let $Y_j(x) = \sqrt{\frac{2}{b}} \sin\left(\frac{(x-x_0+\frac{b}{2})j\pi}{b}\right)$, $j = 1, 2, \dots$. Then, the restriction of the eigenfunctions $X_n \in L^2[0, D]$ on the crack \mathcal{T} may be written as

$$X_n(x)|_{[x_0-b/2, x_0+b/2]} = \sum_{j=1}^{\infty} v_j^n Y_j(x), \text{ where } v_j^n = \int_{x_0-\frac{b}{2}}^{x_0+\frac{b}{2}} X_n(x) Y_j(x) dx.$$

The orthonormality of the Y_i 's and Parseval's relation imply that

$$a_{mn} = (X_m, X_n)_{L^2(\mathcal{T})} = \sum_i (X_m, Y_i)_{L^2(\mathcal{T})} (X_n, Y_i)_{L^2(\mathcal{T})} = \sum_{i=1}^{\infty} v_i^m v_i^n. \quad (2.20)$$

Let us define

$$\mathbf{v}_i = (v_i^1, v_i^2, \dots, v_i^M, \dots)^T, \quad (2.21)$$

and note that the sequences $\mathbf{v}_i \in l_2$, for every i . Then the infinite matrix A_{inf} may be written as

$$A_{\text{inf}} = \sum_{i=1}^{\infty} \mathbf{v}_i \mathbf{v}_i^T. \quad (2.22)$$

Moreover, the \mathbf{v}_i are orthonormal. Indeed, let $\langle \cdot, \cdot \rangle$ denote the standard inner product in l_2 , and \tilde{Y}_i the extension by zero of Y_i on $[0, D]$. Then

$$\begin{aligned} \langle \mathbf{v}_i, \mathbf{v}_j \rangle &= \sum_{n=1}^{\infty} v_i^n v_j^n = \sum_n (X_n, Y_i)_{L^2(\mathcal{T})} (X_n, Y_j)_{L^2(\mathcal{T})} \\ &= \sum_n (\tilde{Y}_i, X_n)_{L^2[0, D]} (\tilde{Y}_j, X_n)_{L^2[0, D]} \\ &\stackrel{\text{Parseval}}{=} (\tilde{Y}_i, \tilde{Y}_j)_{L^2[0, D]} = (Y_i, Y_j)_{L^2(\mathcal{T})} = \delta_{ij}. \end{aligned}$$

Let V be the closure of $\text{span}\{\mathbf{v}_i\}_{i=1,2,\dots}$. Then $l_2 = V \oplus V^\perp$, and A_{inf} is a projection operator whose eigenvalues are 0 and 1.

It remains to investigate the relation between the eigenvectors \mathbf{u}_j of A_M that correspond to eigenvalues close to 1, and the eigenvectors \mathbf{v}_j of A_{inf} corresponding to the eigenvalue 1. Let us multiply, for example, A_M by the vector consisting of the M first components of \mathbf{v}_j , (i.e., $(v_j^1, v_j^2, \dots, v_j^M)^T$).

The i -th component of the resulting vector is equal to

$$\begin{aligned}
\sum_{k=1}^M a_{ik} v_j^k &= \sum_{k=1}^{\infty} a_{ik} v_j^k - \sum_{k=M+1}^{\infty} a_{ik} v_j^k \\
&= \sum_{k=1}^{\infty} (X_i, X_k)_{L^2(\mathcal{T})} (X_k, Y_j)_{L^2(\mathcal{T})} - \sum_{k=M+1}^{\infty} a_{ik} v_j^k \\
&= \sum_{k=1}^{\infty} (X_i \mathbb{1}_{\mathcal{T}}, X_k)_{L^2[0,D]} (\tilde{Y}_j, X_k)_{L^2[0,D]} - \sum_{k=M+1}^{\infty} a_{ik} v_j^k \\
&= (X_i \mathbb{1}_{\mathcal{T}}, \tilde{Y}_j)_{L^2[0,D]} - \sum_{k=M+1}^{\infty} a_{ik} v_j^k = v_j^i - \left(\sum_{k=M+1}^{\infty} a_{ik} v_j^k \right).
\end{aligned}$$

The last term above in the parenthesis depends on i , j , b and D , and is in general small (this has been checked numerically in all the test cases that we have considered). Hence if the j -th singular value is approximately 1, then $(v_j^1, v_j^2, \dots, v_j^M)^T$ approximates \mathbf{u}_j , i.e., the j -th singular vector of A_M . This is illustrated in Figure 2.8 where we plot the components of the first two singular vectors \mathbf{u}_J , $J = 1, 2$, of A_M and the M first terms of the sequences \mathbf{v}_J , $J = 1, 2$, for the parameters of the previous example for which $M = 19$.

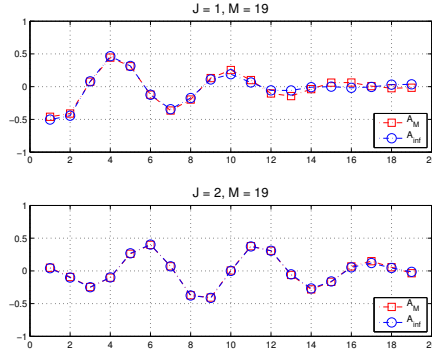


Figure 2.8: The singular vector \mathbf{u}_J of A_M (its components are marked with red squares) vs. the M first terms of \mathbf{v}_J marked with blue circles, for $J = 1$ (top) and $J = 2$ (bottom).

Hence, as long as J is associated to a singular vector that lies in the signal

subspace, one may approximate $\tilde{\mathcal{I}}_J^{\text{KM}}$ as

$$\tilde{\mathcal{I}}_J^{\text{KM}}(\vec{y}^s) \approx \sum_{m,n=1}^M X_m(x^s) X_n(x^s) v_J^m v_J^n = \left(\sum_{n=1}^M v_J^n X_n(x^s) \right)^2, \quad (2.23)$$

where constants are once more suppressed. Moreover, for M large enough, we formally get

$$\begin{aligned} (\tilde{\mathcal{I}}_J^{\text{KM}}(\vec{y}^s))^{1/2} &\approx \left| \sum_{n=1}^{\infty} v_J^n X_n(x^s) \right| = \left| \sum_n (X_n, Y_J)_{L^2(\mathcal{T})} X_n(x^s) \right| \\ &= \left| \sum_n (\tilde{Y}_J, X_n)_{L^2[0,D]} X_n(x^s) \right| = |\tilde{Y}_J(x^s)|. \end{aligned} \quad (2.24)$$

Using the specific form of the Y_J we deduce that, as long as the J -th singular value is close to one,

$$\tilde{\mathcal{I}}_J^{\text{KM}}(\vec{y}^s) \approx \frac{2}{b} \sin^2 \left(\frac{(x^s - x_0 + \frac{b}{2})J\pi}{b} \right). \quad (2.25)$$

In the next section, we will compare these asymptotic results with numerical simulations.

2.4 Numerical experiments

In this section, we present numerical results for the simplified model of the vertical one dimensional scatterer (the crack) and specifically, we compare results of selective imaging with $\tilde{\mathcal{I}}_J^{\text{KM}}$ with those obtained using the asymptotic formulae (2.23), (2.25). In the following examples the sound speed is taken equal to $c_0 = 1500$ m/s and the depth of the waveguide is equal to $D = 200$ m. First, we consider a single frequency $f = 74$ Hz, hence the wavelength $\lambda \approx 20.27$ m. The array has $N = 39$ receivers, the pitch $h = 5$ m $\simeq \lambda/4$ and the crack, centered at $(L, x_0) = (410, 70)$ m, has length $b = 40$ m $\simeq 2\lambda$. The number of propagating modes in the waveguide is $M = 19$. The singular values of A_M are shown in Figure 2.2. We have seen previously that A_M and, consequently, the matrix $\hat{\mathbb{P}}$ defined in (2.5), have $[2b/\lambda] = 4$ significant singular values. In other words, and with reference to Figure 2.2, it is expected that the first three singular vectors comprise the

signal subspace, the fourth and the fifth lie in the transient subspace, and the rest correspond to the noise subspace.

We now turn to check the validity of the asymptotic expressions (2.23) and (2.25). In Figure 2.9 we plot superimposed the normalized graphs of $\tilde{\mathcal{I}}_J^{\text{KM}}(\vec{x}^s, \omega)$ (see (1.21)), of (2.23) and of (2.25), for \vec{x}^s that are located at the correct range L , and for $J = 1$ and 2. The subscript J indicates that only the J -th singular vector is employed in the filtered version of the matrix $\hat{\mathbb{P}}$, defined in (2.5). As one may immediately see there is good agreement between the numerics and the asymptotic expressions.

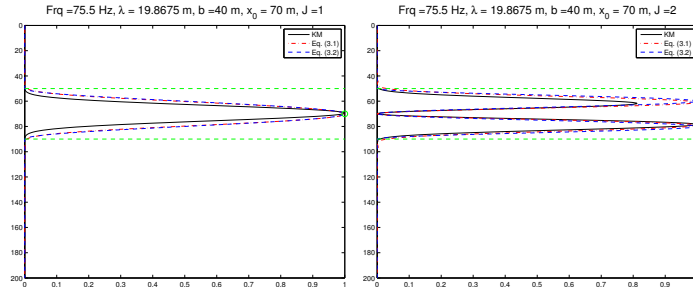


Figure 2.9: The graph of $\tilde{\mathcal{I}}_J^{\text{KM}}((L, x^s), \omega)$ (solid black line) normalized and superimposed on the graphs of (2.23) (dash-dotted red line) and (2.25) (dashed blue line). J indicates projection on the J th singular vector. The ordinates $x_0 - b/2$ and $x_0 + b/2$ are in dashed green lines, and x_0 is marked with a green circle. Here $c_0 = 1500$ m/s, $f = 74$ Hz, $D = 200$ m, $b = 40$ m, $x_0 = 70$ m and $J = 1$ (left subplot), $J = 2$ (right subplot).

In Figure 2.10 we show analogous results for selective imaging with $\tilde{\mathcal{I}}_J^{\text{KM}}(\vec{x}^s, \omega)$ and (2.23), based on the third to the sixth singular vectors. Now, one may notice somewhat larger discrepancies but, in general, the asymptotic expression agrees well with the numerical results for $J = 3, 4$ and 5. For $J = 6$ there is a clear mismatch, with $\tilde{\mathcal{I}}_J^{\text{KM}}$ focusing approximately 4.5 m below the lower endpoint of the crack, since now the corresponding singular vector belongs to the noise subspace. (The discrepancies, as expected, are even larger between the results of $\tilde{\mathcal{I}}_J^{\text{KM}}(\vec{x}^s, \omega)$ and (2.25), and we do not include them in the figure. These discrepancies may be attributed to the fact that the asymptotic analysis is based on matrices of order n , where $n \rightarrow \infty$, while in

the numerics only their principal $M \times M$ part has been taken into account. For example, the orthogonality of the \mathbf{v}_i is valid only for the infinite matrix A_{inf} and is expected to hold only approximately for fixed n .

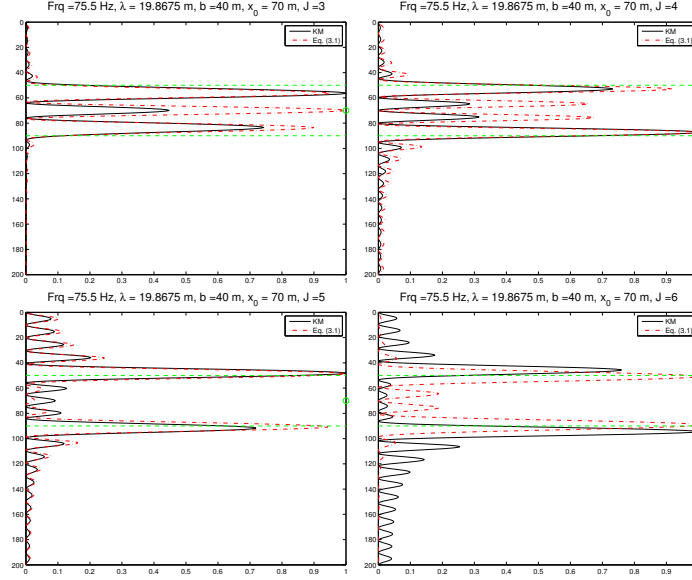


Figure 2.10: The graph of $\tilde{\mathcal{I}}_J^{\text{KM}}((L, x^s), \omega)$ (solid black line) superimposed on the graph of (2.23) (dash-dotted red line). J indicates projection on the J th singular vector and the ordinate $x_0 - b/2$ and $x_0 + b/2$ are in dashed green lines, while x_0 is marked with a green circle. Here $J = 3, 4, 5$ and 6 , $c_0 = 1500$ m/s, $f = 74$ Hz, $D = 200$ m, $b = 40$ m, $x_0 = 70$ m.

Figures 2.9 and 2.10, suggest that selective imaging with $\tilde{\mathcal{I}}_J^{\text{KM}}(\omega)$ by means of the first singular vector focuses in the middle of the object, while the fourth and the fifth singular vectors are focusing mainly in the lower and the upper endpoint of the crack, respectively.

Chapter 3

Model problems vs. full objects

In chapter 2, we examined properties of the response matrix for the model problem with the crack. In this chapter, we want to compare imaging results between the full object, where we retrieve the response matrix by solving the wave equation in our domain, and the model problem, which simulates the boundary of the object that is facing the array, where in this case we construct $\hat{\Pi}^{sc}$ using the Born approximation. We will also examine the comparison between another model problem of a semicircle and its respective full object, a disc shaped scatterer. The reason behind these comparisons is to examine if the behavior of $\tilde{\mathcal{I}}^{KM}$ for the model problem with the crack remains the same when we move to the square and, also, we want to see if this is also the case in other geometries. For all the numerical results we present in this chapter, we consider a waveguide with depth equal to $D = 200$ m and sound speed $c_0 = 1500$ m/s. We use a single frequency of $f = 73$ Hz for all our results.

3.1 Square scatterer vs. crack

First, we want to compare the results we get when we use selective imaging with $\tilde{\mathcal{I}}^{KM}$ when the scatterer is a crack, with the corresponding ones for the square. The side length of the square and the width of the crack is taken equal to $b = 40$ m. The square is centered at $x_0 = (470, 70)$ m, while the crack is centered at $x_0 = (450, 70)$ m so that the left side of the square and the body of the crack coincide.

First, in Figure 3.1 we see imaging results for $\tilde{\mathcal{I}}^{\text{KM}}$, for the square scatterer in the left, and for the crack in the right. As we have explained in Chapter 2, the model problem with the crack was motivated by the fact that imaging the square locates the left side of it.

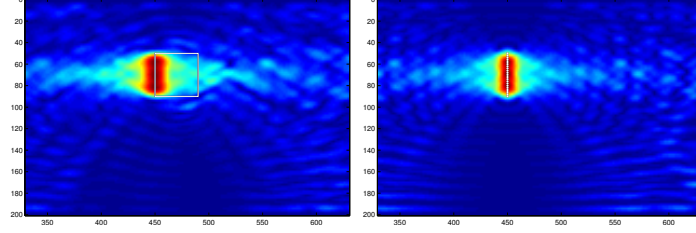


Figure 3.1: Values of $\tilde{\mathcal{I}}^{\text{KM}}$ for the square scatterer (left) and for the crack (right), for $b = 40$ m, $D = 200$ m, $c_0 = 1500$ m/s, $f = 73$ Hz.

In Figure 3.2, we plot the singular values of $\hat{\mathbb{P}}$ for the square on the left subplot, and for the crack on the right. For the square we observe that we have that the 3 first singular values are above 0.7, while for the crack case they are clustered closer to 1, and are above 0.9. As we have shown in Chapter 2 and specifically in (2.9), for our current setup we have 4 significant singular values, that give us information about the object.

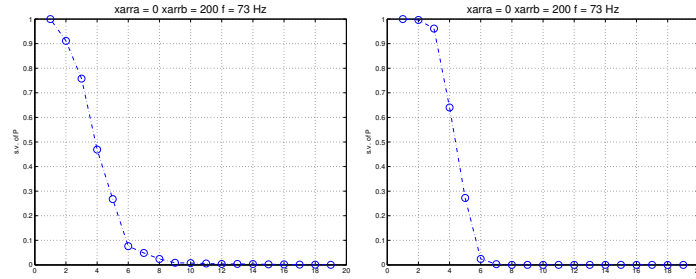


Figure 3.2: Normalized singular values of $\hat{\mathbb{P}}$ for the square scatterer (left) and for the crack (right), for $b = 40$ m, $D = 200$ m, $c_0 = 1500$ m/s, $f = 73$ Hz.

Next, in Figure 3.3 we have the results for selective imaging with $\tilde{\mathcal{I}}_J^{\text{KM}}$ for the square scatterer in the top row and for the crack in the bottom row, for $J = 1, 2, 3, 4$. We observe that when we project on the first singular vector, both images seem to focus on the center of the illuminated edge,

while when projecting on the next singular vectors, we see that the focusing moves towards the edges of the objects, as predicted by the theory.

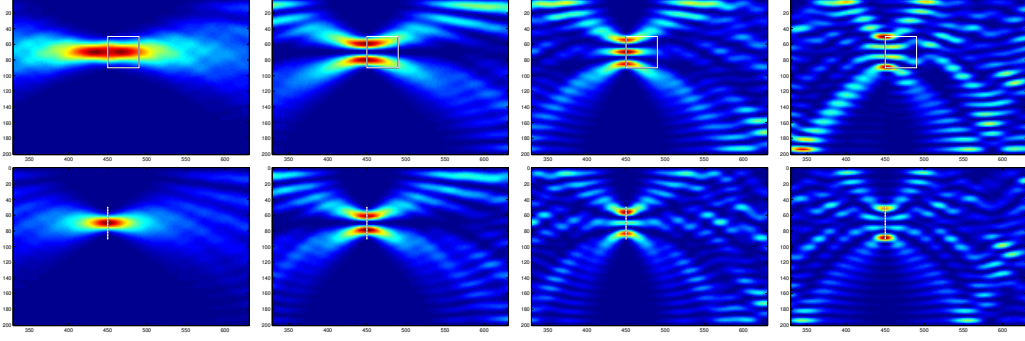


Figure 3.3: Values of $\tilde{\mathcal{I}}_J^{KM}$ for the square scatterer (top) and for the crack (bottom), for $b = 40$ m, $D = 200$ m, $c_0 = 1500$ m/s, $f = 73$ Hz, for $J = 1, 2, 3, 4$.

What is of particular interest here, is the fact that while the way we acquire the response matrix for the model problem and the square varies greatly, we see that our numerical results match the theory and the focusing behavior of $\tilde{\mathcal{I}}_J^{KM}$ is preserved when moving from the model problem to the square.

3.2 Disc shaped scatterer vs. semicircle

Next, we want to compare the results we get when we use selective imaging with $\tilde{\mathcal{I}}^{KM}$ for another scatterer geometry with the ones we just showed. In this case, we want to see the results when imaging a disc shaped scatterer and the equivalent of the crack in this case, a semicircle. First, let us present a brief analysis of the semicircle problem, similar to what we did for the crack.

We assume that the target \mathcal{T} is a semicircular arc (with diameter parallel to the x axis) of radius ρ , centered at $\mathbf{y}^* = (L + \rho, x_0)$. Let us also denote $\mathbf{y}_1^* = (L + \rho, x_0 - \rho)$ and $\mathbf{y}_2^* = (L + \rho, x_0 + \rho)$ the endpoints of the arc.

We approximate the response in a receiver placed at $\vec{\mathbf{x}}_r = (0, x_r)$ due to

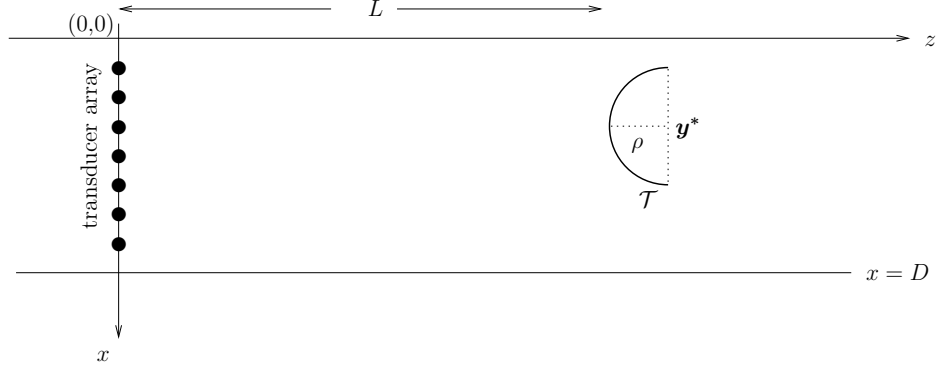


Figure 3.4: Schematic representation of the waveguide and basic notation.

a point source at $\vec{x}_s = (0, x_s)$, $r, s \in \{1, 2, \dots, N\}$, as

$$\hat{\Pi}(\vec{x}_r, \vec{x}_s, \omega) = \int_{\mathcal{T}} \hat{G}(\vec{y}, \vec{x}_r) \hat{G}(\vec{y}, \vec{x}_s) d\sigma, \quad (3.1)$$

where $\vec{y} \in \mathcal{T}$. We parametrize \mathcal{T} as follows. Let

$$z = L + \rho - \rho \sin t = L + \rho(1 - \sin t), \quad x = x_0 - \rho \cos t.$$

Then the line integral (3.1) with respect to arc length equals

$$\begin{aligned}
\widehat{\Pi}(\vec{x}_r, \vec{x}_s, \omega) &= \int_0^\pi \widehat{G}\left((L + \rho(1 - \sin t), x_0 - \rho \cos t); (0, x_r)\right) \\
&\quad \times \widehat{G}\left((L + \rho(1 - \sin t), x_0 - \rho \cos t); (0, x_s)\right) \sqrt{\left(\frac{dz}{dt}\right)^2 + \left(\frac{dx}{dt}\right)^2} dt \\
&= -\frac{1}{4} \int_0^\pi \sum_{m=1}^\infty \sum_{n=1}^\infty \frac{1}{\beta_m} e^{i\beta_m(L + \rho(1 - \sin t))} X_m(x_0 - \rho \cos t) X_m(x_r) \\
&\quad \times \frac{1}{\beta_n} e^{i\beta_n(L + \rho(1 - \sin t))} X_n(x_0 - \rho \cos t) X_n(x_s) \rho dt \\
&= -\frac{1}{4} \sum_{m=1}^\infty \sum_{n=1}^\infty \frac{1}{\beta_m} \frac{1}{\beta_n} X_m(x_r) X_n(x_s) \\
&\quad \times \int_0^\pi e^{i(\beta_m + \beta_n)(L + \rho(1 - \sin t))} X_m(x_0 - \rho \cos t) X_n(x_0 - \rho \cos t) \rho dt \\
&= -\frac{1}{4} \sum_{m=1}^\infty \sum_{n=1}^\infty \frac{1}{\beta_m} \frac{1}{\beta_n} X_m(x_r) X_n(x_s) \\
&\quad \times \int_0^\pi e^{i\beta_m(L + \rho(1 - \sin t))} X_m(x_0 - \rho \cos t) e^{i\beta_n(L + \rho(1 - \sin t))} X_n(x_0 - \rho \cos t) \rho dt
\end{aligned}$$

Passing the terms $e^{i\beta_m L}$ and $e^{i\beta_n L}$ outside the integral and we get

$$\begin{aligned}
\widehat{\Pi}(\vec{x}_r, \vec{x}_s, \omega) &= -\frac{1}{4} \sum_{m=1}^\infty \sum_{n=1}^\infty \frac{e^{i\beta_m L}}{\beta_m} \frac{e^{i\beta_n L}}{\beta_n} X_m(x_r) X_n(x_s) \\
&\quad \times \int_0^\pi e^{i(\beta_m + \beta_n)\rho(1 - \sin t)} X_m(x_0 - \rho \cos t) X_n(x_0 - \rho \cos t) \rho dt.
\end{aligned}$$

Now, let B be the matrix with entries

$$B_{mn} = \int_0^\pi e^{i(\beta_m + \beta_n)\rho(1 - \sin t)} X_m(x_0 - \rho \cos t) X_n(x_0 - \rho \cos t) \rho dt, \quad m, n = 1, 2, \dots$$

Then $\widehat{\Pi}$ may be written as

$$\widehat{\Pi} = \mathcal{G} B \mathcal{G}^T, \quad (3.2)$$

where G is the same matrix as in (2.4), which describes the scattered field for the crack but now B does not possess the special Toeplitz-minus-Hankel structure, as was the case for A in the crack problem.

In our experiment, the diameter of both the disc and the semicircle is taken equal to $\delta = 40$ m and their centers are placed at $x_0 = (440, 100)$ m. In Figure 3.5 we plot the imaging results for $\tilde{\mathcal{I}}^{KM}$, for the disc shaped scatterer in the left and for the semicircle in the right. We observe again that our images are mainly focused on the leftmost side of our objects and we have a good agreement between the image for the semicircle and the disc.

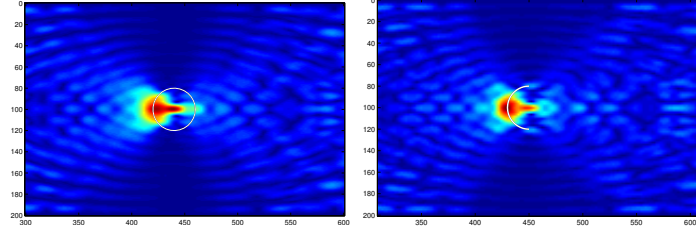


Figure 3.5: Values of $\tilde{\mathcal{I}}^{KM}$ for the circular scatterer (top) and for the semicircle (bottom), for $\delta = 40$ m, $D = 200$ m, $c_0 = 1500$ m/s, $f = 73$ Hz.

In Figure 3.6, we plot the singular values of $\hat{\mathbb{P}}$ for the disc on the left subplot, and for the semicircle on the right. Now we see that for the disc we seem to have 3 singular values that are above 0.5, while the rest lie below 0.2. For the semicircle, the first 3 singular values are above 0.7 and there are also 2 singular values above 0.3. While for the crack we had a special form for A , we could identify the number of significant singular values. However, since this is not the case for the semicircle, we cannot have an explicit relation between the size of the object and the number of significant singular values.

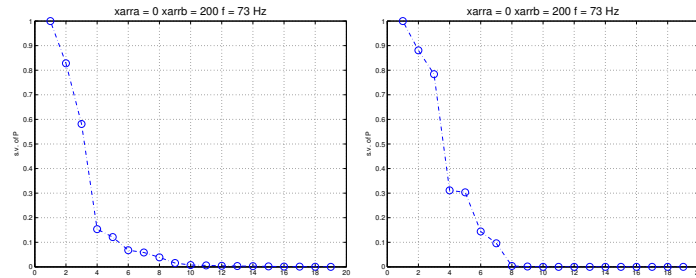


Figure 3.6: Normalized singular values of $\hat{\mathbb{P}}$ for the disc shaped scatterer (left) and for the semicircle (right), for $\delta = 40$ m, $D = 200$ m, $c_0 = 1500$ m/s, $f = 73$ Hz.

In Figure 3.7 we have the results for selective imaging with $\tilde{\mathcal{I}}_J^{KM}$ for the circular scatterer in the top row and for the semicircle in the bottom row, for $J = 1, 2, 3, 4$. We see that the selective imaging results in this case, remind us of the ones we obtained for the square and the crack in the previous case, in the sense that when we project on the first singular vector we locate the center of the target, while the following singular vectors focus towards the edges of the object.

In this case, using selective imaging was more helpful than in the square case, since, alongside focusing on specific parts of the object, we have the added benefit of getting information about parts of the object that are not illuminated when we use the full matrix to create an image. We see that although in Figure 3.5 we recover the leftmost part of the scatterers, when we do selective imaging with $\tilde{\mathcal{I}}_J^{KM}$ we have focusing further towards the edges of the vertical diameter of the objects for $J = 2, 3$. This illustrates the benefits of selective imaging that allows us to focus at the edges of the object and therefore obtain more information about its shape and size. Also, for $J = 4$ we seem to have a focusing on the right side of the disc, which could be misleading, if not for the fact that the same image is present for the semicircle, which has no body on that side, so we regard that focusing as an accident.

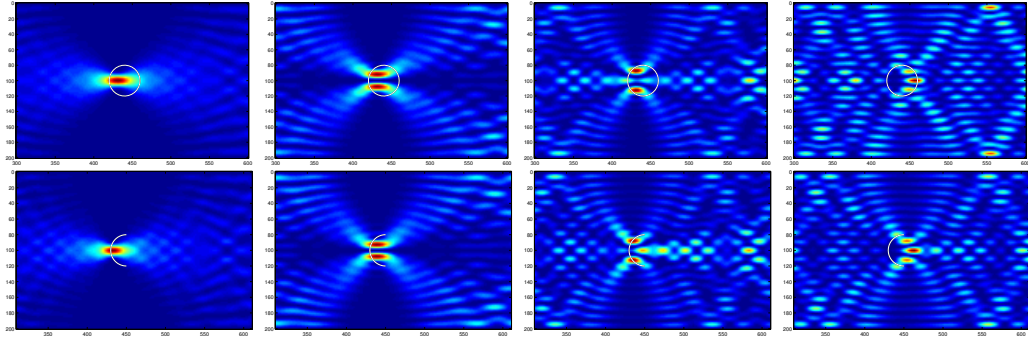


Figure 3.7: Values of $\tilde{\mathcal{I}}_J^{KM}$ for the circular scatterer (top) and for the semi-circle (bottom), for $\delta = 40$ m, $D = 200$ m, $c_0 = 1500$ m/s, $f = 73$ Hz, for $J = 1, 2, 3, 4$.

Chapter 4

Partial array imaging

In this chapter, we discuss the problem of imaging an extended reflector when the array \mathcal{A} has partial aperture, *i.e.*, it does not span the whole depth of the waveguide. As remarked in Chapter 1, and further investigated in Chapter 2 in the case of the crack model-problem, the assumption that the array spans the whole depth of the waveguide allows us to exploit the orthonormality of the vertical eigenfunctions X_n along the array in order to study the spectral properties of matrix $\hat{\mathbb{P}}$. Let us remind that $\hat{\mathbb{P}}$ is a weighted modal projection of the original array response matrix and that the construction and behaviour of the proposed imaging functional $\tilde{\mathcal{I}}^{\text{KM}}$ depends crucially on $\hat{\mathbb{P}}$. However, as expected, in the case of the partial array aperture the X_n 's are not any longer orthonormal along the array. In this chapter we propose a modification in the definition of $\hat{\mathbb{P}}$ which allows us to extend the applicability of $\tilde{\mathcal{I}}^{\text{KM}}$ in the case of partial array aperture. Let us also note that imaging with \mathcal{I}^{KM} does not require any modification for partial array aperture imaging and therefore it is interesting to assess its performance and compare it with $\tilde{\mathcal{I}}^{\text{KM}}$ as the array's aperture becomes smaller.

4.1 The weighted modal projection for the partial array case

In this work, as already mentioned in Chapter 1, we assume that our data for the scattered field is given in the form of the so-called array response matrix

$\widehat{\Pi}$; its size is $N \times N$ where N is the number of the transducers in the array. Moreover, recall that in order to construct the imaging functionals $\widetilde{\mathcal{I}}^{\text{KM}}$ we have introduced through (1.13) an $M \times M$ matrix $\widehat{\mathbb{P}}$, where M is the number of propagating modes, with entries

$$\widehat{\mathbb{P}}_{mn}(\omega) = \beta_m \beta_n \int_0^D dx_s \int_0^D dx_r \widehat{\Pi}(\vec{x}_s, \vec{x}_r, \omega) X_m(x_s) X_n(x_r), \quad (4.1)$$

where $m, n = 1, 2, \dots, M$. In what follows we assume that $N \geq M$, unless stated otherwise.

Now, we approximate the integrals in (4.1) using the composite trapezoidal rule in the partition of $[0, D]$ that is induced by the array's transducers. Thus, we may write down the following relation between $\widehat{\mathbb{P}}$ and $\widehat{\Pi}$:

$$\widehat{\mathbb{P}} = -\frac{h^2}{4} D_\beta^{-1} V^T \widehat{\Pi} V D_\beta^{-1}, \quad (4.2)$$

where h is the inter-element array distance (pitch), V is the $N \times M$ matrix with entries

$$V_{k\ell} = \sqrt{\frac{2}{D}} \sin\left(\frac{\ell \pi x_k}{D}\right), \quad k = 1, \dots, N, \quad \ell = 1, \dots, M, \quad (4.3)$$

and D_β is the $M \times M$ diagonal matrix $\text{diag}\left(\frac{1}{\beta_1}, \frac{1}{\beta_2}, \dots, \frac{1}{\beta_M}\right)$.

At this point, in order to gain some understanding in the case where the array has partial aperture, let us bring back to our minds the crack model problem where the Born approximation allows us to write the array response matrix $\widehat{\Pi}$ as in (2.4). Alternatively, in view of the above notation, we may write $\widehat{\Pi}$ as

$$\widehat{\Pi} = -\frac{1}{4} V D_\beta Q A_M Q D_\beta V^T, \quad (4.4)$$

where A_M is the principal $M \times M$ part of A_{inf} , cf. (2.3), and

$$Q = \text{diag}(e^{i\beta_1 L}, \dots, e^{i\beta_M L}).$$

Next, we insert (4.4) into (4.2) to deduce that $\widehat{\mathbb{P}}$ may be written in the form

$$\widehat{\mathbb{P}} = -\frac{h^2}{4} D_\beta^{-1} V^T V D_\beta Q A_M Q D_\beta V^T V D_\beta^{-1}. \quad (4.5)$$

Note that when the array has full aperture, *i.e.* $\mathcal{A} = [0, D]$, the orthonormality of X_n along the array implies that the matrix $hV^T V$, which

eventually may be viewed as an approximation of the matrix with entries $\int_{\mathcal{A}} X_n(x)X_m(x)dx$, $m, n = 1, \dots, M$, will be practically equal to I_M , where I_M is the identity $M \times M$ matrix. Then (4.5) simplifies to

$$\widehat{\mathbb{P}} = -\frac{1}{4}QA_MQ,$$

and we conclude that $\widehat{\mathbb{P}}$ is unitarily equivalent to A_M , see also (2.6).

However, when the array does not span the whole depth of the waveguide, *i.e.*, $\mathcal{A} \subset [0, D]$, then it does not hold any longer that hV^TV is approximately equal to I_M , and $\widehat{\mathbb{P}}$ does not necessarily have the same spectral properties as A_M . As a remedy to this we propose to modify (4.2) as follows: We multiply $\widehat{\Pi}$ from the left with V^+ instead of V^T , and from the right with $(V^T)^+$ instead of V , where V^+ denotes the Moore–Penrose pseudoinverse of V .

Hence we define $\widehat{\mathbb{P}}$ as

$$\widehat{\mathbb{P}} = D_\beta^{-1}V^+\widehat{\Pi}(V^T)^+D_\beta^{-1}.$$

Now, inserting (4.4) into (4.7) leads to

$$\widehat{\mathbb{P}} = -\frac{1}{4}D_\beta^{-1}V^+VD_\beta QA_MQD_\beta V^T(V^T)^+D_\beta^{-1}. \quad (4.6)$$

If $\text{rank}(V) = M$ then $V^+ = (V^TV)^{-1}V^T$, see for example [20, p. 257]. Moreover, it is then obvious that $V^+V = V^T(V^T)^+ = I_M$, which in turn implies that (4.6) simplifies to

$$\widehat{\mathbb{P}} = -\frac{1}{4}QA_MQ.$$

Thus we conclude that although $\widehat{\mathbb{P}}$ is defined differently than before it is still unitarily equivalent to A_M as long as V is a matrix of full column rank. To summarise, we propose the following definition.

Definition 1 *Given the array response matrix $\widehat{\Pi}$ for the scattered field, we propose to define the matrix $\widehat{\mathbb{P}}$ by*

$$\widehat{\mathbb{P}} = D_\beta^{-1}V^+\widehat{\Pi}(V^T)^+D_\beta^{-1}, \quad (4.7)$$

and then use it in $\tilde{\mathcal{I}}^{\text{KM}}$ (as defined in (1.12))

$$\tilde{\mathcal{I}}^{\text{KM}}(\vec{y}^s, \omega) = -\frac{1}{4h^2} \sum_{m,n=1}^M e^{-i(\beta_m + \beta_n)|z_a - z^s|} X_n(x^s) X_m(x^s) \hat{\mathbb{P}}_{mn}(\omega),$$

for imaging.

Remark 1 For the crack model problem, as long as $\text{rank}(V) = M$, we have shown that the spectral properties of $\hat{\mathbb{P}}$ (as defined by (4.7)) are determined by those of A_M , thus we expect $\tilde{\mathcal{I}}^{\text{KM}}$ to perform in exactly the same way as if we were using an array of full aperture.

Moreover, for the full aperture array, it is immediate to check that $V^+ = hV^T$, hence (4.7) is identical to (4.2).

A question that arises naturally is whether and when V has full column rank or, equivalently, $V^T V$ is invertible, and how is this related to the length of the array \mathcal{A} ?

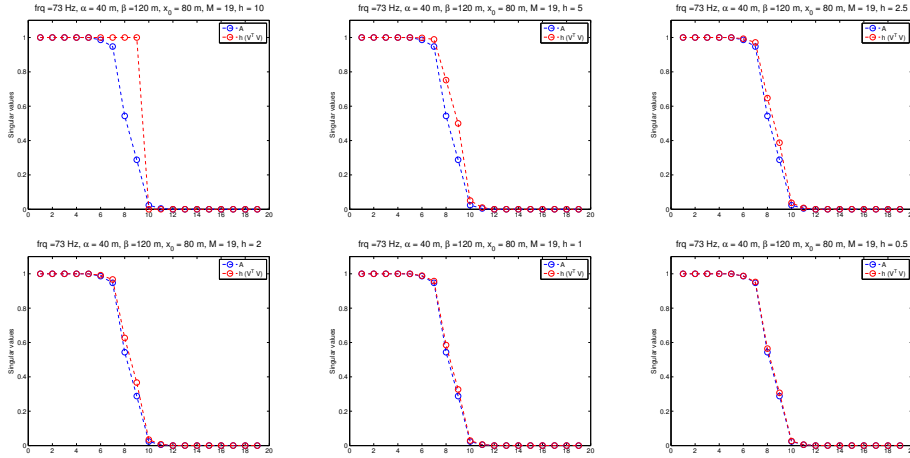


Figure 4.1: Singular values of A_{arr} (blue) and of $h(V^T V)$ (red) for $h = 10, 5, 2.5, 2, 1, 0.5$ m (from top left to bottom right). The array's length equals 80 m and is placed between 40 m and 120 m in a waveguide with depth equal to 200 m. The frequency is $f = 73$ Hz.

An important remark in this direction is that $V^T V$ may be considered as an

approximation of the $M \times M$ matrix A_{arr} with entries defined by

$$(A_{\text{arr}})_{mn} = \frac{1}{h} \int_{\mathcal{A}} X_n(x) X_m(x) dx, \quad \forall m, n = 1, 2, \dots, M.$$

This is illustrated in Figure 4.1 where we superimpose the singular values for the matrices A_{arr} and $hV^T V$ as the pitch h decreases, for an 80 m long array that is located between 40 and 120 meters. The source frequency is 73 Hz and the depth of the waveguide is 200 m, hence $M = 19$ modes propagate. The reference wavelength is taken equal to $\lambda_0 = 20$ m. The top left subplot corresponds to a pitch $h = \lambda_0/2 = 10$ m and while we move to the right we decrease h until the value $h = \lambda_0/40 = 0.5$ m that corresponds to the bottom right subplot. These figures indicate that as h is getting smaller we have a very good agreement between the singular values of these two matrices. Note that, as we have seen in Chapter 2, the matrix A_{arr} is a Toeplitz-minus-Hankel matrix, hence its singular values cluster near 0 and 1. Specifically, if l_{arr} is the length of the array, then the number of singular values that lie near 1 is roughly $\lceil l_{\text{arr}}/(\lambda/2) \rceil$, while the rest $M - \lceil l_{\text{arr}}/(\lambda/2) \rceil$ are approaching zero and comprise the so-called *noise subspace* of the matrix A_{arr} . The number of the singular values of A_{arr} that are small in magnitude increases as the length of the array decreases. At this point, let us remark that, in practice, the rank of the matrix $V^T V$ is computed numerically and specifically is determined by the number of singular values of $V^T V$ that lie above a certain threshold, which, of course, depends on the precision that we use. Therefore as l_{arr} decreases more singular values tend to zero, and in fact $V^T V$ will become practically singular as soon as its minimum singular value μ_{\min} falls below the previously mentioned threshold.

In order to give the reader a sense of how fast μ_{\min} decreases, as l_{arr} decreases, we plot the related values in Figure 4.2. Specifically, values on the x -axis refer to the portion of the array, in meters, that is removed from a 200 m-long array of full aperture, and a logarithmic scale is used for the y -axis. In the left subplot the length of the array is reduced symmetrically with respect to the mid-depth of the waveguide, while in the right one the lower part of the array is removed. The different markers (also typed in different colours) shown in Figure 4.2 correspond to arrays with different densities; the pitch h that corresponds to each marker is reported in the legend of the

figure in terms of a reference wavelength $\lambda_0 = 20$ m.

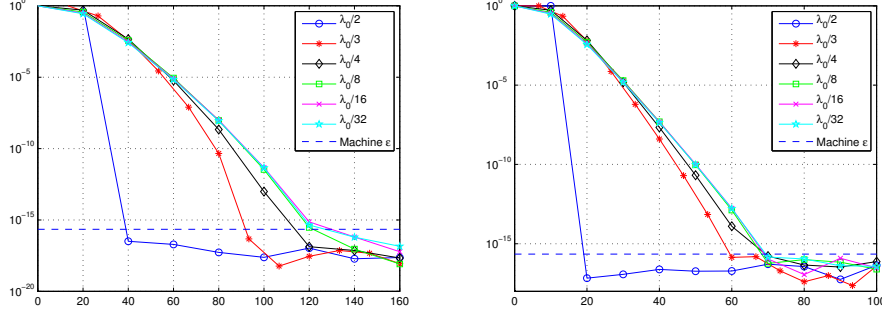


Figure 4.2: Behavior of the minimum singular value of $V^T V$, when we remove elements from the array symmetrically (left subplot) and from the bottom of the array (right subplot), for $f = 73$ Hz.

The results shown in Figure 4.2 suggest that μ_{\min} drops below the machine epsilon ε (indicated here as a blue dashed line, and implemented in MATLAB by the constant `eps` in double precision) much faster in the non-symmetric case (right subplot) than in the symmetric one (left). Moreover, the density of the array also plays a role in the rate at which μ_{\min} drops below ε . For example, μ_{\min} is already less than ε in the case where we remove 40 m from the array with pitch $h = \lambda_0/2$, while it is considerably larger than ε for denser arrays. However, in most cases for a given partial array, an array pitch $h = \lambda_0/4$ seems to suffice in order to assess the behavior of the smaller singular values of $V^T V$; in other words $h = \lambda_0/4$ is enough in order to determine whether $V^T V$ has numerically full column rank. This is of some importance: When $\mu_{\min} < \varepsilon$, $V^T V$ turns to be practically singular, hence many properties that hold in theory, such as $\text{rank}(V^T V) = \text{rank}(V)$, or $V^+ V = I_M$, are not expected to hold any more. For example, in the crack model problem this fact does not allow us any more to deduce from equation (4.6) that A_M and $\hat{\mathbb{P}}$ are unitarily equivalent. Furthermore, the fact that the minimum singular value of V tends to zero as the length of the array decreases has another interesting consequence: The modulus of the entries of matrix V^+ increase. For example, since $\|V\|_2 = \text{maximum singular value of } V$, it is

immediate to check that

$$\|V^+\|_2 = (\text{minimum singular value of } V)^{-1}.$$

Given that in (4.7), V^+ multiplies from the left (and its transpose from the right) the matrix $\widehat{\Pi}$, this may probably cause a significant loss of accuracy. For example, when we remove 160 m from an array with pitch $h = 2$ m the minimum singular value of V equals 2.51×10^{-15} , hence $\|V^+\|_2 = 3.98 \times 10^{14}$, $\|\widehat{\Pi}\|_2 \approx 14.3$, while $\|\widehat{\mathbb{P}}\|_2 \approx 1.05 \times 10^{12}$, whereas normally we would expect it to be approximately equal to $\|A_M\|_2 = 1$. (All these computations were performed with MATLAB.)

We close this section with a general comment: When we deal with more realistic problems that entail general shaped scatterers we cannot, in general, determine a particular expression for $\widehat{\Pi}$, e.g. in the form of (4.4), that would allow us to investigate its connection with the modified array response matrix $\widehat{\mathbb{P}}$ that is defined in (4.2) for an array with full aperture, or in (4.7) for an array with partial aperture. However, in the case of the full array-aperture we have seen that the use of $\widehat{\mathbb{P}}$, and its associated imaging functional $\widetilde{\mathcal{I}}^{\text{KM}}$, yield better results than the conventional Kirchhoff migration functional \mathcal{I}^{KM} , *cf.* [1] and, also, Chapter 1. In the following sections we will find that this is also true in the partial array-aperture case.

4.2 Imaging with \mathcal{I}^{KM} for the model problem

In Chapter 1, we have seen for a full array-aperture that imaging with \mathcal{I}^{KM} compared to $\widetilde{\mathcal{I}}^{\text{KM}}$ has some disadvantages: Images produced with \mathcal{I}^{KM} exhibit many oscillations (see for example Figure 1.4), and selective imaging with $\mathcal{I}_J^{\text{KM}}$ does not demonstrate the expected from the free-space case ordering. The term ‘expected ordering’ is used in the sense that projection on the singular vector that corresponds to the largest singular value is associated to an image focused on the center of the object, while the ones that correspond to smaller singular values carry information about its edges. In this section we will assess the performance of \mathcal{I}^{KM} in the crack model problem as we reduce the length of the array.

The setting for the numerical experiments that we are going to perform next is the same as in Section 2.4. Specifically, the sound speed is $c_0 = 1500$ m/s, the reference frequency is $f_0 = 75$ Hz, hence the reference wavelength $\lambda_0 = 20$ m, and the depth of the waveguide is equal to $D = 200$ m. We consider a single frequency $f = 73$ Hz, hence the wavelength $\lambda \approx 20.55$ m, and $M = 19$ modes propagate. The scatterer, i.e. the crack, is centered at $(L, x_0) = (450, 100)$ m and its length is $b = 40$ m $= 2\lambda_0$. The pitch of the array is equal to $h = \lambda_0/4 = 5$ m, unless stated otherwise.

To begin, we reduce the length of the full aperture array by 20 m $= 1\lambda_0$ symmetrically, *i.e.* we cut 10 m from each side of the array. The image obtained with \mathcal{I}^{KM} is shown in Figure 4.3. The crack is depicted by a white vertical line, and as we may see it is clearly detected although some oscillations are also present. Let us note that in order to produce all \mathcal{I}^{KM} images shown in this section we do not include the last propagating mode during the computation of the Green's function that is necessary to evaluate \mathcal{I}^{KM} , since its presence results in some numerical instabilities that add a lot of extra noise in the image.

One way to assess the noise level of an image, is to look at the image's Signal-to-Noise Ratio (SNR), which here is defined as

$$\text{SNR} = \frac{\max_{\vec{\mathbf{x}}^s \in \mathcal{R}} |\mathcal{I}^{\text{KM}}(\vec{\mathbf{x}}^s)|}{\max_{\vec{\mathbf{x}}^s \in \mathcal{S}, \vec{\mathbf{x}}^s \notin \mathcal{R}} |\mathcal{I}^{\text{KM}}(\vec{\mathbf{x}}^s)|},$$

where \mathcal{R} is usually determined according to what the image indicates with regard to the location of the scatterer. Here we use the SNR value as a quantitative measure that corroborates the qualitative characteristics of the image and, since the location of the scatterer is known, we fix \mathcal{R} as a $6\lambda_0 \times 6\lambda_0$ box with the scatterer lying at its center. In Figure 4.3, and in what follows, \mathcal{R} is drawn in red.

Removing 20 m symmetrically.

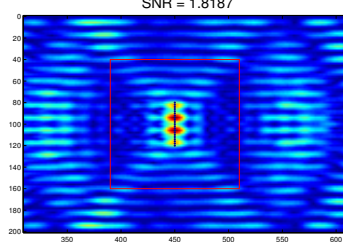


Figure 4.3: Imaging with \mathcal{I}^{KM} for the crack, when we remove 20 m from the array symmetrically, for $f = 73$ Hz.

Next, in Figure 4.4, we present the outcome of selective imaging with the functional $\mathcal{I}_J^{\text{KM}}$, for $J = 1, 2, 3, 4$. We observe that the $\mathcal{I}_J^{\text{KM}}$ images are again quite noisy, while the $\mathcal{I}_J^{\text{KM}}$ image for $J = 1$ is too noisy to allow us to locate the position of the scatterer. The images for $J = 2$ and 4 seem to provide information about the edges of the object with a good SNR above 1.5, however the image for $J = 2$ exhibits many oscillations, while for $J = 4$ the focusing is quite spread and does not give clear information about the object. On the other hand, \mathcal{I}^{KM} for $J = 3$ clearly focuses on the center of the crack; the good quality of this image is also supported by its high SNR value.

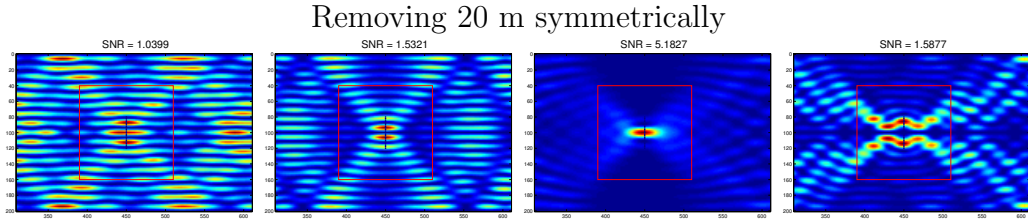


Figure 4.4: Imaging with $\mathcal{I}_J^{\text{KM}}$ for the crack, for $J = 1, 2, 3, 4$ when we remove 20 m from the array symmetrically, for $f = 73$ Hz.

When we remove $40 \text{ m} = (2\lambda_0)$ from the array, the resulting images are similar to those shown in Figure 4.4, yet of slightly worse quality. Our next step is to remove $60 \text{ m} = (3\lambda_0)$ from the array. Figure 4.5 depicts the image created with \mathcal{I}^{KM} . We see now that the \mathcal{I}^{KM} image has deteriorated a lot and based on its SNR we cannot be certain of the presence of an object in our search domain.

Removing 60 m symmetrically.

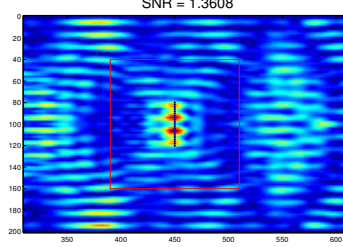


Figure 4.5: Imaging with \mathcal{I}^{KM} for the crack, when we remove 60 m from the array symmetrically, for $f = 73$ Hz.

This can be also seen in Figure 4.6, where selective imaging with $\mathcal{I}_J^{\text{KM}}$ yields only one image, the one that corresponds to $J = 4$, that focuses on the middle of the crack, while the rest of the images are too noisy to be useful. Notice that in this example one should probably combine the \mathcal{I}^{KM} image shown in Figure 4.5 with the one created by $\mathcal{I}_J^{\text{KM}}$ for $J = 4$, and is shown in the rightmost subplot in Figure 4.6, in order to detect the location of the scatterer with some confidence.

However, we should here remark that a reasonable process would be to consider selective imaging only if the \mathcal{I}^{KM} (or, later, the $\tilde{\mathcal{I}}^{\text{KM}}$) image provides some strong indications regarding the presence and the location of a scatterer. Henceforth, we will not pursue selective imaging techniques unless the qualitative characteristics of the \mathcal{I}^{KM} image, and a quantitative index of of an SNR around 1.4, suggest the presence and location of a scatterer.

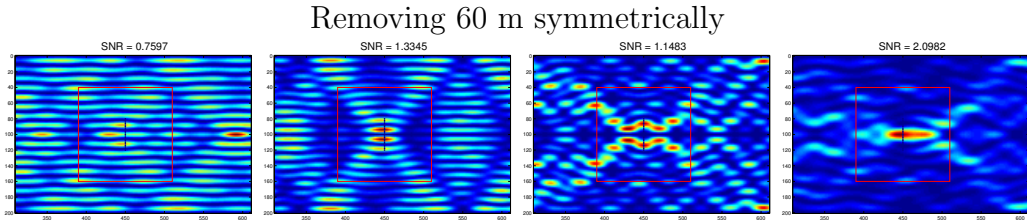


Figure 4.6: Imaging with $\mathcal{I}_J^{\text{KM}}$ for the crack, for $J = 1, 2, 3, 4$ when we remove 60 m from the array symmetrically, for $f = 73$ Hz.

Now, if we further reduce the length of the array the resulting \mathcal{I}^{KM} images are of a very bad quality. In the next section we will examine the performance of $\tilde{\mathcal{I}}^{\text{KM}}$ under the same circumstances.

4.3 Imaging with $\tilde{\mathcal{I}}^{\text{KM}}$ for the model problem

In this section, we assess the performance of the imaging functional $\tilde{\mathcal{I}}^{\text{KM}}$ in the crack model problem as we reduce gradually the length of the array. The physical and technical parameters that we consider in the experiments of this section are the same as those in Section 4.2. The image we obtain with the $\tilde{\mathcal{I}}^{\text{KM}}$ functional when we reduce symmetrically the length of the array by 20 m ($= \lambda_0$) is depicted in Figure 4.7. This compared with Figure 4.3 exhibits a much clearer view of the crack with much better SNR.

Removing 20 m symmetrically.

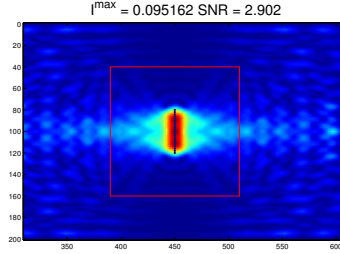


Figure 4.7: Imaging with $\tilde{\mathcal{I}}^{\text{KM}}$ for the crack, when we remove 20 m from the array symmetrically, for $f = 73$ Hz.

Next, in Figure 4.8, we plot selective imaging results obtained with the functional $\tilde{\mathcal{I}}_J^{\text{KM}}$, for $J = 1, 2, 3, 4$. We now observe that selective imaging with $\tilde{\mathcal{I}}_J^{\text{KM}}$ performs as if we were using a full-aperture array; all four images are very good with high $\text{SNR} > 1.9$, and projection on the first singular vector results in focusing on the middle of the crack while projection on the second to fourth singular vectors provides information about the edges of the crack.

Removing 20 m symmetrically

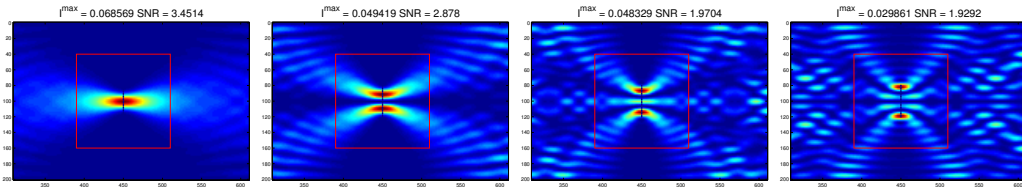


Figure 4.8: Imaging with $\tilde{\mathcal{I}}_J^{\text{KM}}$ for the crack, for $J = 1, 2, 3, 4$ when we remove 20 m from the array symmetrically, for $f = 73$ Hz.

Next, we remove 60 m ($= 3\lambda_0$) from the array symmetrically. Here, as we may immediately verify by comparing Figure 4.9 to Figure 4.7, the $\tilde{\mathcal{I}}^{\text{KM}}$ image remains unchanged; even its SNR value coincides with the previous one reported in Figure 4.7.

Removing 60 m symmetrically.

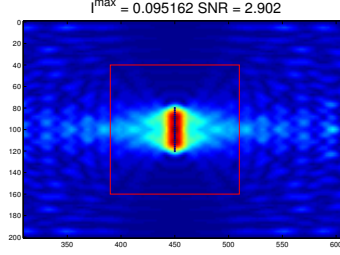


Figure 4.9: Imaging with $\tilde{\mathcal{I}}^{\text{KM}}$ for the crack, when we remove 60 m from the array symmetrically, for $f = 73$ Hz.

Moreover, as one may see in Figure 4.10, selective imaging with $\tilde{\mathcal{I}}_J^{\text{KM}}$ is in perfect agreement with the results that were obtained for the previous array length; compare to Figure 4.8. In both of these examples it holds that $\text{rank}(V^T V) = \text{rank}(V) = 19$, where we want to make clear that the rank is computed numerically with MATLAB that returns the number of singular values of V that are larger than some tolerance (its default value for some matrix C is $\max(\text{size}(C)) \cdot \varepsilon(\|C\|_2)$, where $\varepsilon(c)$ is the positive distance from $|c|$ to the next largest floating-point number of the same precision as c). These examples, and other that we do not show here, strengthen the case that as long as $\text{rank}(V^T V) = M$ (thus $\hat{\mathbb{P}}$ is still unitarily equivalent to A_M) our images are as good as those created with an array that spans the whole depth of the waveguide.

Removing 60 m symmetrically

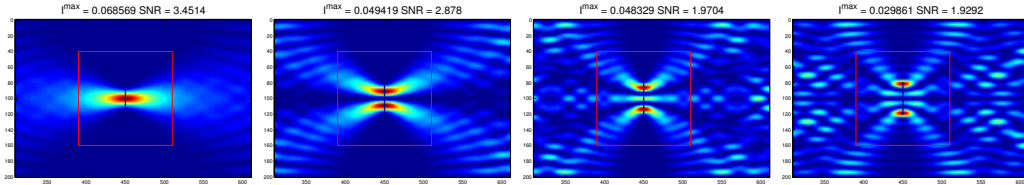


Figure 4.10: Imaging with $\tilde{\mathcal{I}}_J^{\text{KM}}$ for the crack, for $J = 1, 2, 3, 4$ when we remove 60 m from the array symmetrically, for $f = 73$ Hz.

Now, we want to proceed with the case where it does no longer hold that $\text{rank}(V^T V) = 19$, with the current array density suggested by a pitch equal to $h = \lambda_0/4$. To this end we remove 120 m from the array symmetrically, hence the number of the transducers in the array is $N = 17$, *i.e.* it is less than the number of propagating modes $M = 19$. Then $\text{rank}(V^T V) = \text{rank}(V) = 17$ and $V^T V$ is not invertible, so it does not hold that $V^+ V = I_M$, and we do not expect $\hat{\mathbb{P}}$ and A_M to be unitarily equivalent. However, irrespectively of this fact, the $\tilde{\mathcal{I}}^{\text{KM}}$ image in Figure 4.11 remains good, and is certainly much better than the corresponding \mathcal{I}^{KM} image which we did not show in Section 2 because it exhibits so many oscillations that do not allow us to locate the scatterer.

Removing 120 m symmetrically.

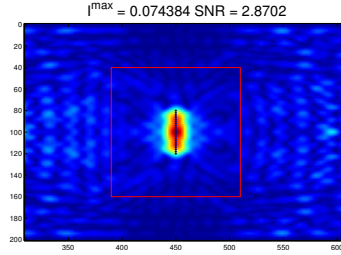


Figure 4.11: Imaging with $\tilde{\mathcal{I}}^{\text{KM}}$ for the crack, when we remove 120 m from the array symmetrically, for $f = 73$ Hz.

Next, in Figure 4.12, we plot the results of selective imaging. Here, the $\tilde{\mathcal{I}}_J^{\text{KM}}$ images are not ordered in the sense that, now, projection on the third singular vector seems to focus on the center of the object whereas this should be expected for $J = 1$. Furthermore, the quality of the images is worsened with respect to the ones of Figure 4.10.

Removing 120 m symmetrically

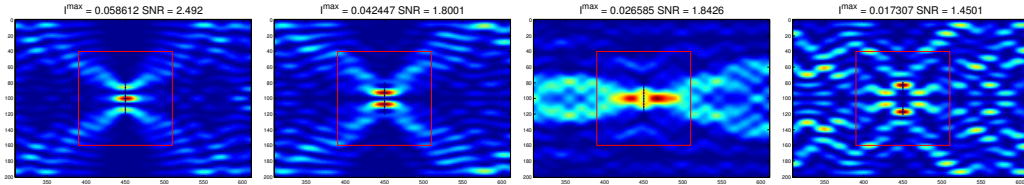


Figure 4.12: Imaging with $\tilde{\mathcal{I}}_J^{\text{KM}}$ for the crack, for $J = 1, 2, 3, 4$ when we remove 120 m from the array symmetrically, for $f = 73$ Hz.

Now, looking back to Figure 4.2, we realise that if we make the array denser by using a pitch of $h = \lambda_0/8$ meters, then the minimum singular value of $V^T V$, μ_{min} , is lifted a bit, enough to be above machine ε . Now, $N = 33$, $M = 19$ and $\text{rank}(V^T V) = \text{rank}(V) = 19$ in the sense that 19 singular values of the corresponding matrices are larger than $\varepsilon \approx 2.2 \times 10^{-16}$. Figure 4.13, presents the $\tilde{\mathcal{I}}^{\text{KM}}$ imaging when we remove 120 m from the array symmetrically, but now for $h = \lambda_0/8 = 2.5$ m. We observe that by making the array denser the $\tilde{\mathcal{I}}^{\text{KM}}$ image is better, and resembles to the images we have seen for smaller cuts in the array, with an SNR almost the same as before.

Removing 120 m symmetrically.

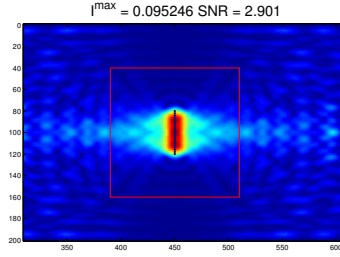


Figure 4.13: Imaging with $\tilde{\mathcal{I}}^{\text{KM}}$ for the crack, when removing 120 m from the array symmetrically, for $f = 73$ Hz.

Moreover, selective imaging with $\tilde{\mathcal{I}}_J^{\text{KM}}$, as shown in Figure 4.14, exhibits the expected ordering, and better quality corroborated by better SNR values.

Removing 120 m symmetrically

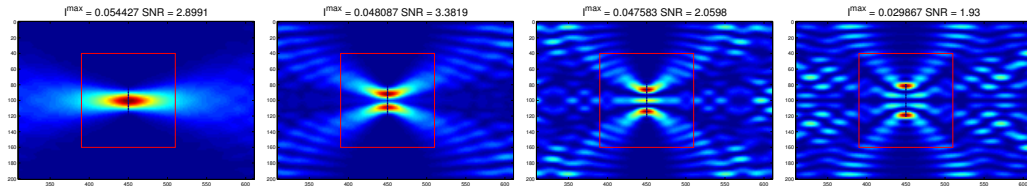


Figure 4.14: Imaging with $\tilde{\mathcal{I}}_J^{\text{KM}}$ for the crack, for $J = 1, 2, 3, 4$ when removing 120 m from the array symmetrically, for $f = 73$ Hz.

To summarize, we have seen here that, in this specific model problem, as long as the unitary equivalence between $\hat{\mathbb{P}}$ and A_M is preserved, we expect to obtain very good images with $\tilde{\mathcal{I}}^{\text{KM}}$. This is the case even if we remove almost

60% of the length of a quite fine array, symmetrically. However, as Figure 4.2 indicates, this will not be possible to hold for larger and/or non-symmetric cuts and this is the case that we will examine in the next subsection.

4.3.1 Using a regularized pseudoinverse

Turning back to Figure 4.2 and to the discussion in Section 4.1 about the behavior of the singular values of the matrix $V^T V$, we realise that, as the array becomes smaller, the small in magnitude singular values of $V^T V$ will become inevitably less than some very small positive number, say, ε . As a result, even if we consider a very fine array ensuring that $N > M$, at some time $\text{rank}(V^T V) \neq M$ numerically. However, since the singular values of V are equal to the square root of the corresponding ones of $V^T V$, it might be the case that numerically $\text{rank}(V) \neq \text{rank}(V^T V)$.

At this point we introduce an auxiliary tolerance ε^+ such that the number of singular values that are larger than ε^+ will be equal to the number of singular values of $V^T V$ that are larger than ε . (Note that $\varepsilon^+ \approx \sqrt{\varepsilon}$.) This is going to ensure numerically that $\text{rank}(V) = \text{rank}(V^T V)$.

Let us go on with some numerical experiments using the same parameter set as in the previous section. To start with, we remove 140 m from the array symmetrically, *i.e.* its endpoints are at 70 m and 130 m, respectively. The density of the array is determined by a pitch equal to $h = \lambda_0/8 = 2.5$ m, hence the number of transducers $N = 25$, while $M = 19$. Then, we find numerically that $\text{rank}(V^T V) = 16 < 19 = \text{rank}(V)$. Note that the minimum singular value of V is approximately equal to 1.59×10^{-11} and $\|V^+\|_2 = 6.28 \times 10^{10}$.

In the bottom left subplot of Figure 4.15 we plot the image obtained with $\tilde{\mathcal{I}}^{\text{KM}}$, which is very bad, depicts only noise, and does not give us any indication of the presence of a scatterer.

Our next attempt, is to employ the tolerance ε^+ in the computation of the pseudoinverse V^+ of V which is based on the SVD of V and treats any singular values of V less than ε^+ as zero. In this way the matrix $\hat{\Pi}$, in (4.7), is multiplied from the left and from the right with regularised pseudo inverses of V and V^T , respectively. Specifically, using an ε^+ that removes the last 3 singular values of V we obtain the $\tilde{\mathcal{I}}^{\text{KM}}$ image shown in the bottom right

subplot of Figure 4.15, which clearly focuses on the crack. Note that now $\|V^+\|_2 \approx 9.6 \times 10^5$.

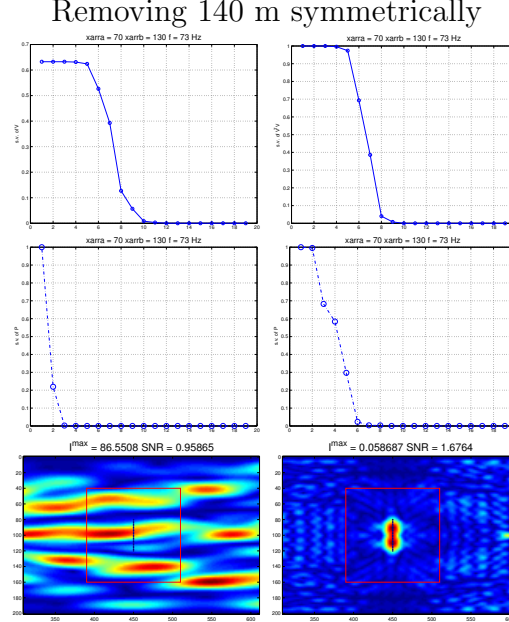


Figure 4.15: Top: SVD of V (left) and $V^T V$ (right). Middle: SVD of $\hat{\mathbb{P}}$ without tolerance (left) and with tolerance that removes the last 3 singular values. Bottom: Imaging with $\tilde{\mathcal{I}}^{\text{KM}}$ without tolerance (left) and with tolerance that removes the last 3 singular values (right), when we remove 140 m from the array symmetrically, for $h = \lambda_0/8$ and $f = 73$ Hz.

Figure 4.16 depicts selective imaging results with $\tilde{\mathcal{I}}_J^{\text{KM}}$, where in the course of constructing $\hat{\mathbb{P}}$ we employ the tolerance ε^+ in the computation of the pseudoinverse V^+ of V . We observe that although the usual sense of ordering is lost, the images for $J = 2, 3$ and 4 have good SNR and provide useful information about the object.

Removing 140 m symmetrically

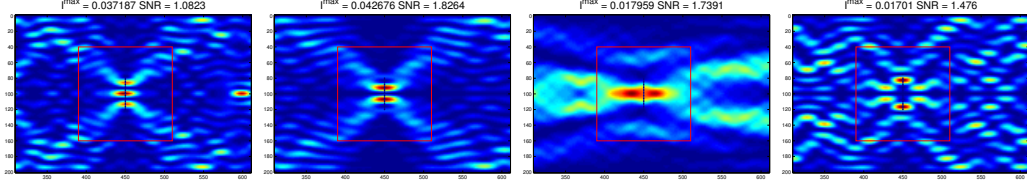


Figure 4.16: Imaging with $\tilde{\mathcal{I}}_J^{\text{KM}}$ for the crack, for $J = 1, 2, 3, 4$ when removing 140 m from the array symmetrically, for $h = \lambda_0/8$ and $f = 73$ Hz.

Our next move is to push $\tilde{\mathcal{I}}^{\text{KM}}$ to the limit for this model problem. In Figure 4.17 we see the imaging results with $\tilde{\mathcal{I}}^{\text{KM}}$ (top row), when we remove 180 m from the array symmetrically. In this case, we make the array denser, by setting the pitch $h = \lambda_0/32 = 0.625$ m, in order to have $N > M$ and we choose an ε^+ that removes the last 9 singular values of V . We observe that the $\tilde{\mathcal{I}}^{\text{KM}}$ image gives us very good information about the object, although its SNR value is quite low, around 1.1, due to a ghost behind the crack. In the bottom row of Figure 4.17 we show selective imaging results with $\tilde{\mathcal{I}}_J^{\text{KM}}$. Now only the image for $J = 1$ gives us good information, with higher SNR than the $\tilde{\mathcal{I}}^{\text{KM}}$ image.

Removing 180 m symmetrically, $h = \lambda_0/32$.

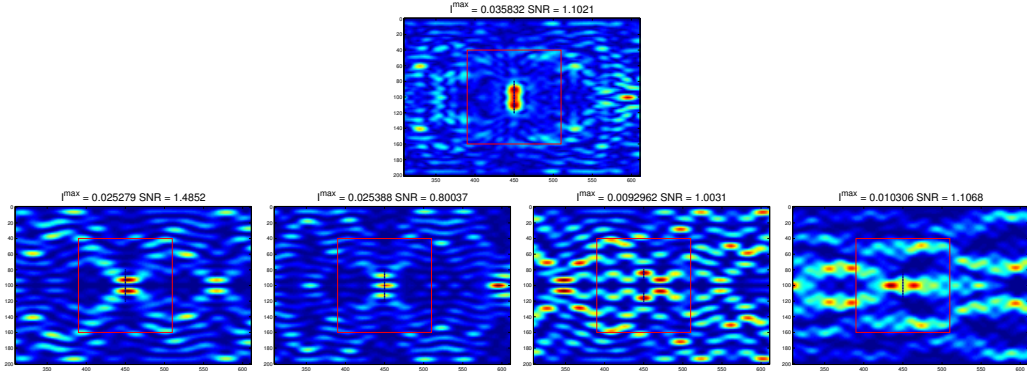


Figure 4.17: Imaging with $\tilde{\mathcal{I}}^{\text{KM}}$ for the crack (top), and $\tilde{\mathcal{I}}_J^{\text{KM}}$ for $J = 1, 2, 3, 4$ (bottom) when removing 180 m from the array symmetrically, for $f = 73$ Hz.

We close this section with another experiment. As in the beginning of this section, we consider an array with length equal to 60 m, *i.e.* we remove 140 m symmetrically. The difference is that we keep the value of the pitch

equal to $h = \lambda_0/4 = 5$ m, thus the number of the transducers in the array is $N = 13 < 19 = M$. Here numerically, as well as analytically, we have that $\text{rank}(V^T V) = \text{rank}(V) = 13 < M$. Now, we do not employ any tolerance in the computation of V^+ . In Figure 4.18 we plot from left to right the SVD of V , $V^T V$ and $\hat{\mathbb{P}}$ and the image created with $\tilde{\mathcal{I}}^{\text{KM}}$.

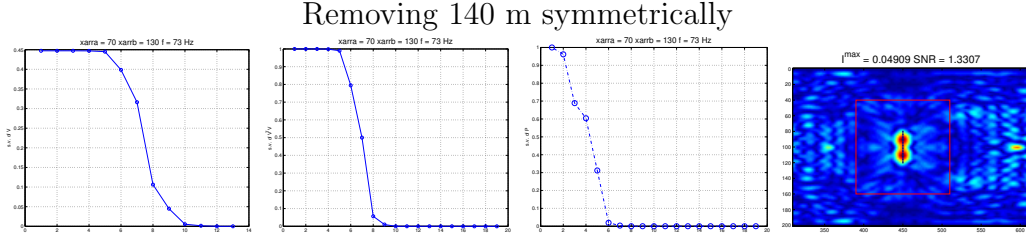


Figure 4.18: From left to right: SVD of V , $V^T V$, $\hat{\mathbb{P}}$ and imaging with $\tilde{\mathcal{I}}^{\text{KM}}$ without tolerance (right), when we remove 140 m from the array symmetrically, for $f = 73$ Hz.

Next, in Figure 4.19 we plot the results of selective imaging with $\tilde{\mathcal{I}}_J^{\text{KM}}$. We have that the images for $J = 2, 3$ give us information about the object with a higher SNR than the full matrix image, while the rest of the images have a low SNR. These figures have slightly poorer quality compared with the corresponding ones in Figures 4.15, 4.16. Nevertheless, and despite the fact that we work in this ideal model problem, it is interesting that although the matrix $V^T V$ is rank deficient, this seems to regularise the matrix V^+ enough in order to make this approach to give satisfactory results.

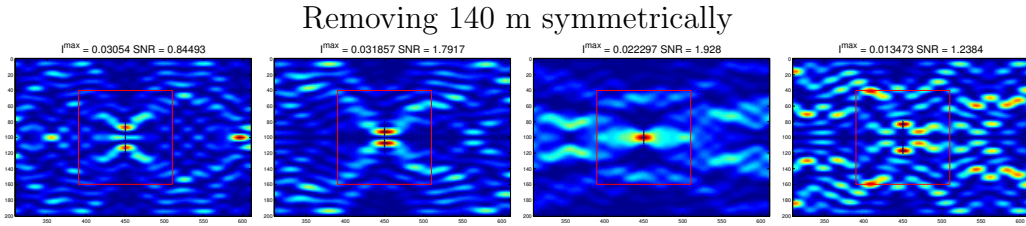


Figure 4.19: Imaging with $\tilde{\mathcal{I}}_J^{\text{KM}}$ for the crack, for $J = 1, 2, 3, 4$ when we remove 140 m from the array symmetrically, for $f = 73$ Hz.

4.3.2 Adding noise in the data

In the previous subsection, we have noticed that $\tilde{\mathcal{Z}}^{\text{KM}}$ for the model problem seems to work very well, even when removing ninety percent of our array! Of course, this concerns the crack model problem in which, under the Born approximation, it is possible to derive $\hat{\Pi}$ and $\hat{\mathbb{P}}$ in the special forms (4.4) and (4.6), respectively. Then, under the assumption that all required operations are carried out exactly we obtain that $\hat{\mathbb{P}}$ is unitarily equivalent with A_M . However, in the previous subsection we have seen that in practice, where almost everything is computed numerically, things are more complicated and extra care has to be taken, as the length of the array is reduced, in order to take into account inevitable loss of accuracy due to floating point operations.

As a step forward to a less ideal case, where it is not possible to express the array response matrix for the scattered field in an explicit form, we add noise to $\hat{\Pi}$. This is succeeded by the same process as we did in Section 1.4.

We start by adding 20 dB noise in our data, and we consider an array where we have removed 60 m, symmetrically, and the pitch $h = \lambda_0/4 = 5$ m. The rest of the parameters remain the same as in the previous sections. In Figure 4.20 we have on the top row the SVD of V on the left and the SVD of $V^T V$ on the right. On the bottom row, we have the SVD of $\hat{\mathbb{P}}$ and image that we obtain with $\tilde{\mathcal{Z}}^{\text{KM}}$. In this case we do not remove any singular value from V during the computation of V^+ , since there are no singular values of $V^T V$ smaller than machine ε . We observe that in this case, there is only one singular value that is high and in fact we have that the first singular value lies at $1.64 \cdot 10^3$, the second at $1.1 \cdot 10^2$, while the rest are below 1. As a result, the image we get is just noise. Our next attempt is to employ some tolerance ε^+ during the computation of V^+ in order to remove singular values from V .

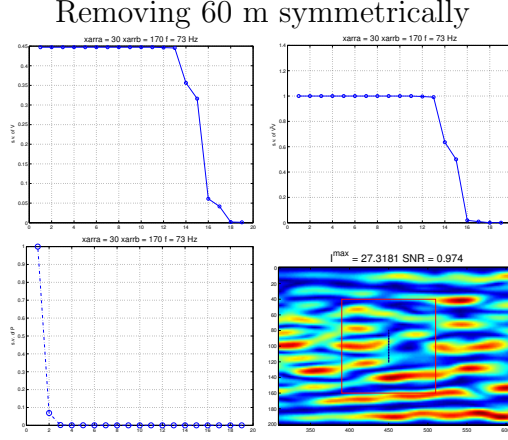


Figure 4.20: Top row: SVD of V (left) and $V^T V$ (right). Bottom row: SVD of $\hat{\mathbb{P}}$ (left) and imaging with $\tilde{\mathcal{I}}^{\text{KM}}$ without regularization (right), when we remove 60 m from the array symmetrically, for $f = 73$ Hz.

With reference to the top right subplot in Figure 4.20, and using the same terminology as in Sections 2.1.1 and 4.1, we may say that the last four singular values of $V^T V$ correspond to its *noise subspace*. Hence one may try to compute V^+ with some regularization by imposing a tolerance ε^+ that will remove from V as many small singular values as the number of singular values of $V^T V$ that lie in its noise subspace dictates. However, we prefer to be more cautious and remove gradually one singular value at the time. The results are shown in Figure 4.21, where we observe that when choose ε^+ in order to remove just the minimum singular value of V during the computation of V^+ , we still get only noise in the image. When we remove the last two singular values we get an image that locates the object, but the SVD of $\hat{\mathbb{P}}$ has only one significant singular value. When we remove another singular value, we see that the image has reduced SNR, but the SVD of $\hat{\mathbb{P}}$ is closer to the full array case. Finally, when we remove the last four singular values of V , the result seems to be equally good. To summarize, implementing a tolerance ε^+ that removes from V as many small singular values as the number of singular values of $V^T V$ that lie in its noise subspace, seems to be a good practice in order to obtain a good image. This has also been verified by other experiments for different array lengths, and for the same noise level.

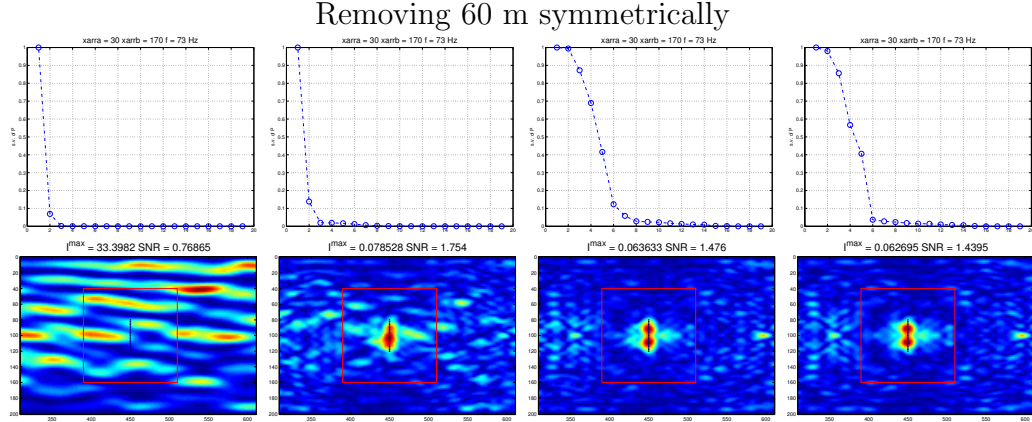


Figure 4.21: SVD of $\widehat{\mathbb{P}}$ (top) and imaging with $\widetilde{\mathcal{I}}^{\text{KM}}$ (bottom) for the crack, with tolerance that removes the 1,2,3,4 last singular values (from left to right), when removing 60 m from the array symmetrically, for $f = 73$ Hz.

Next we want to examine the effect of adding more noise to the data on the images. So, we now add 10 dB of noise, and in Figure 4.22 we start with the case where we have removed the last 3 singular values of V (in all previous cases the image was bad, exhibiting just noise). We observe that when we remove the last 3 singular values we are able to locate the crack, but the singular values of $\widehat{\mathbb{P}}$ are not distributed well. By removing 4 singular values we see that they are better separated and we now see the effect of the noise on the smaller singular values, much like what we have observed in Figure 1.7. Removing another singular value seems to help with separating the singular value subspaces more clearly and it has also increased the image's SNR. However, if we remove one more, we observe a decrease in the values of the second and third singular values that drop below 0.8 and the image is mainly focused around the center of the crack.

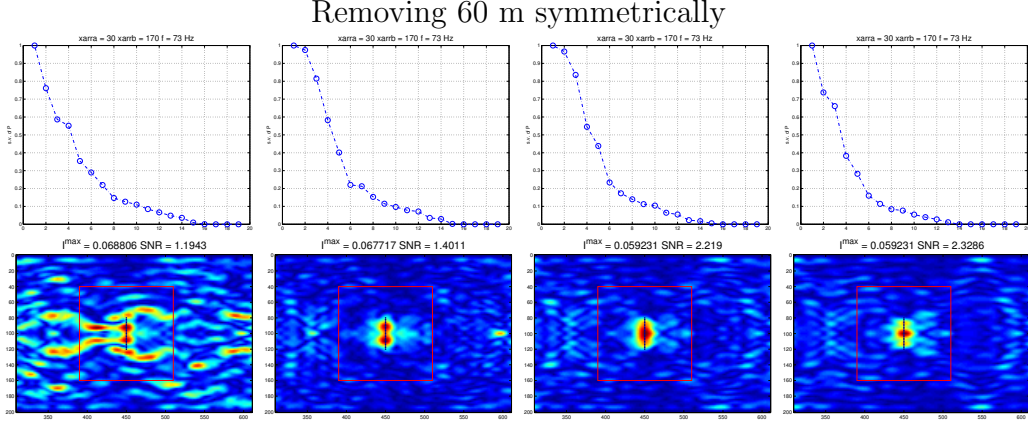


Figure 4.22: SVD of $\widehat{\mathbb{P}}$ (top) and imaging with $\widetilde{\mathcal{I}}^{\text{KM}}$ (bottom) for the crack, with tolerance that removes the 3, 4, 5, 6 last singular values (from left to right), when we remove 60 m from the array symmetrically, for $f = 73$ Hz.

So, we may comment that as the noise level increases it is not clear that removing only those singular values of V that correspond to the noise subspace of $V^T V$ would give the best image.

4.3.3 Algorithm for imaging with partial aperture arrays

So far, in this chapter, we have tried to assess the performance of the imaging functionals $\widetilde{\mathcal{I}}^{\text{KM}}$ and $\widetilde{\mathcal{I}}_j^{\text{KM}}$ in the crack model problem when the array has partial aperture. Based on the experience that we have gained, and in an attempt to describe systematically the procedure of imaging with a partial-aperture array, we summarise the basic steps of the proposed approach in the form of an algorithm. Specifically, the steps that we use are the following:

1. We form the matrix V defined in (4.3), its corresponding Gram matrix $V^T V$, and we compute their SVD.
2. We compute the pseudoinverse V^+ using a suitable tolerance ε^+ that removes from V singular values that are less than ε^+ .
3. We form the matrix $\widehat{\mathbb{P}}$ that is defined in (4.7).

4. We create an image with $\tilde{\mathcal{I}}^{\text{KM}}$.
5. If the quality and the SNR of the image are good, then we proceed to try selective imaging with $\tilde{\mathcal{I}}_J^{\text{KM}}$.

Let us remark here that ε^+ is the regularization parameter of our approach and its determination is not given by a universal formula as is often the case in inverse problems. We summarize below the insight we have gained so far with our numerical simulations.

In the crack model problem, and for the noiseless case, we found that it suffices to choose an ε^+ which guarantees that $\text{rank}(V) = \text{rank}(V^T V)$. When we had noise in our data, we determined ε^+ in order to remove from V a number of its smallest singular values that is equal to the number of singular values that correspond to the noise subspace of $V^T V$. However, as we have already discussed, this is not necessarily true for higher levels of noise. Moreover, the so-called noise subspace of $V^T V$ is only affected by the length and the position of the array and not by the noise level in the data.

In general, it would be safer to follow a more conservative approach, and remove gradually the smaller singular values from V , one at the time, until we get a sufficiently good image and a reasonable SVD of $\hat{\mathbb{P}}$. On the other hand, it could be more effective to try first to remove from V the number of its smallest singular values that is equal to the number of singular values that correspond to the noise subspace of $V^T V$, and then, if the results are acceptable, resort to some ‘fine tuning’ by adding or removing singular values.

4.4 Application of the algorithm

In this section we want to assess the performance of $\tilde{\mathcal{I}}^{\text{KM}}$ for an array with partial aperture, in the case where the scatterer is a square or a disc. Now, the array response matrix for the scattered field $\hat{\Pi}$ is evaluated numerically as it is described in Section 1.4.

In our experiments, we use a single frequency $f = 73$ Hz, the square is centered at $(470, 100)$ m and has side length $b = 40$ m $= (2\lambda_0)$, while the disc is centered at $(440, 100)$ m and its diameter $\delta = 40$ m. The rest of the parameters remain the same as in previous sections.

To begin with, we remove 20 m from the array symmetrically. In Figure 4.23 we plot on the top row the SVD of V on the left and of $V^T V$ on the right. Based on the singular values of $V^T V$, it seems that there is no need to remove any singular values in the computation of V^+ . Indeed, the $\tilde{\mathcal{I}}^{\text{KM}}$ images for the square and the disc, that are shown in the bottom row of Figure 4.23, are both very good. The image for the square focuses on the left side of the scatterer, while for the disc we have a focus mainly around the leftmost part of the scatterer.

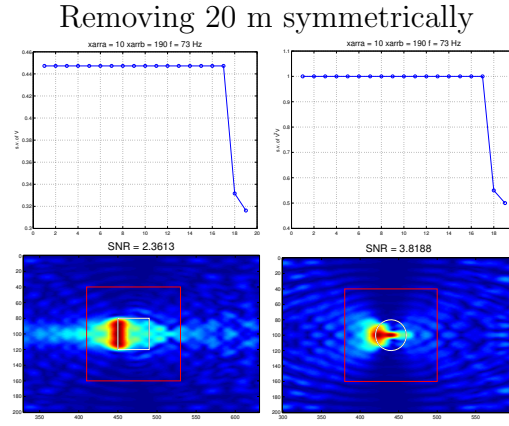


Figure 4.23: Top row: SVD of V (left) and $V^T V$ (right). Bottom row: Imaging with $\tilde{\mathcal{I}}^{\text{KM}}$ for the square (left) and the disc (right), when we remove 20 m from the array symmetrically, for $f = 73$ Hz.

Next, in Figure 4.24, we present the results of selective imaging with $\tilde{\mathcal{I}}_J^{\text{KM}}$ for the square on the top row and for the disc on the bottom row. The images are very similar to the ones we have seen for the full array case in Chapter 3, with only a slight loss in SNR.

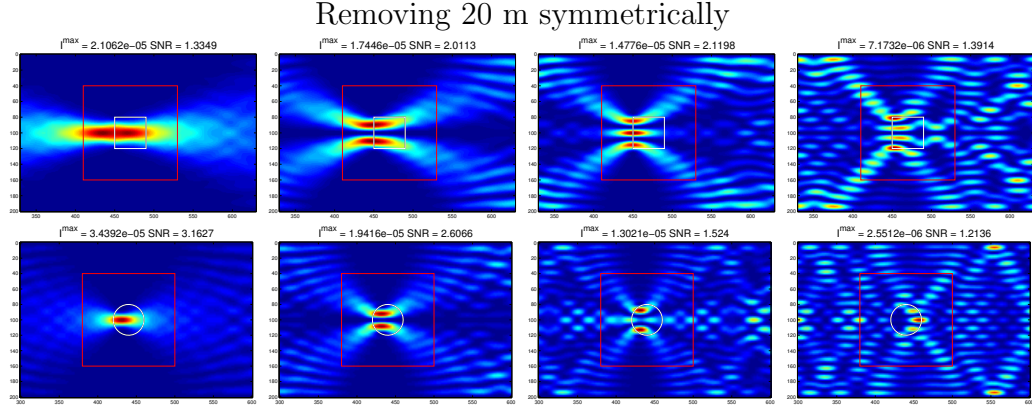


Figure 4.24: Imaging with $\mathcal{I}_J^{\text{KM}}$ (top) and $\tilde{\mathcal{I}}_J^{\text{KM}}$ (bottom) for the square, for $J = 1, 2, 3, 4$ when we remove 20 m from the array symmetrically, for $f = 73$ Hz.

Next, we remove 40 meters from the array, symmetrically. Now, the SVD of $V^T V$ is shown in the right subplot of Figure 4.25 and suggests that the last two singular values are quite small, in fact are of the order of 10^{-2} . This is an indication that we may need to employ a tolerance ε^+ in order to exclude some singular values of V during the computation of V^+ .

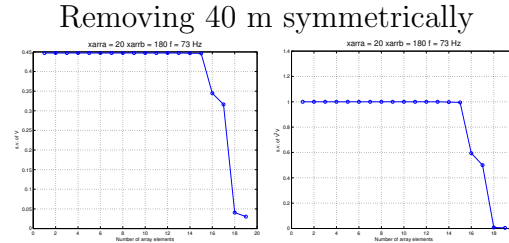


Figure 4.25: SVD of V (left) and $V^T V$ (right), when we remove 40 m from the array symmetrically, for $f = 73$ Hz.

Indeed, the bad images shown in the left column of Figure 4.26, are the outcome of using $\tilde{\mathcal{I}}^{\text{KM}}$ without imposing any tolerance in the computation of V^+ ; the results we get are just noise. The same happens when we remove the last singular value, as one may verify by looking at the middle column of Figure 4.26. However, if we use a tolerance that discards the last two singular values of V from the computation of V^+ , we get the good images in the right column of Figure 4.26.

In the results we will present next, we will always impose a tolerance in the computation of V^+ that removes the smallest singular values of V that are dictated by the number of the singular values of $V^T V$ that correspond to its noise subspace.

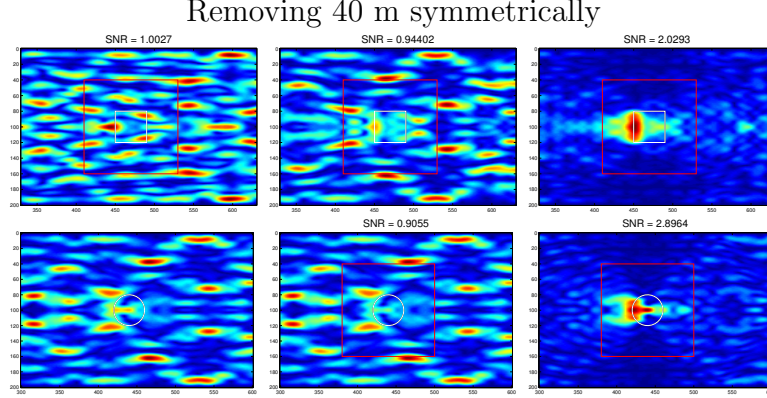


Figure 4.26: Imaging with $\tilde{\mathcal{I}}^{\text{KM}}$ without tolerance (left) and with tolerance that removes the last (middle) and the 2 last singular values (right) for the square (top) and the disc (bottom), when we remove 40 m from the array symmetrically, for $f = 73$ Hz.

Next, in Figure 4.27, we plot the results of selective imaging with $\tilde{\mathcal{I}}_J^{\text{KM}}$ for the square on the top row and for the disc on the bottom row. The fact that the images follow the usual ordering, while we have imposed some tolerance during the computation of V^+ , is regarded as a lucky accident. Let us note here that the $\tilde{\mathcal{I}}_J^{\text{KM}}$ image for $J = 3$ gives us good information about the object, but its SNR is around 1, which means that the level of noise in the picture is almost the same at the peaks of the image on the object. Also, the image for $J = 4$ for the square and the image for $J = 3$ for the disc have very similar SNR, but the disc image has significantly less oscillations. The point here is that while images with high SNR are usually very good, there are cases where images with SNR less than 1.4 may also provide useful information about the object.

Removing 40 m symmetrically

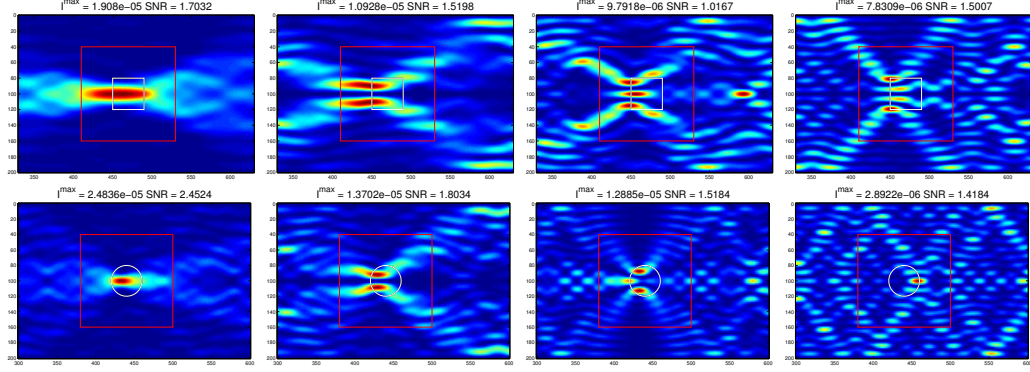


Figure 4.27: Imaging with $\mathcal{I}_J^{\text{KM}}$ (top) and $\tilde{\mathcal{I}}_J^{\text{KM}}$ (bottom) for the square, for $J = 1, 2, 3, 4$ when we remove 40 m from the array symmetrically, for $f = 73$ Hz.

Following the same steps, we remove 60 meters from the array, symmetrically. Then the quality of the images is slightly deteriorated, but they are still similar to the ones we just saw so we do not present them.

We continue decreasing the length of the array, where now we remove 80 meters, symmetrically. In Figure 4.28, we see that the image for the disc only has a peak on the leftmost part of the scatterer, while the image for the square continues to have a clear focusing on the whole left side of the scatterer. Our hope is that selective imaging will reveal more information about the body of the disc, as it did in the previous cases.

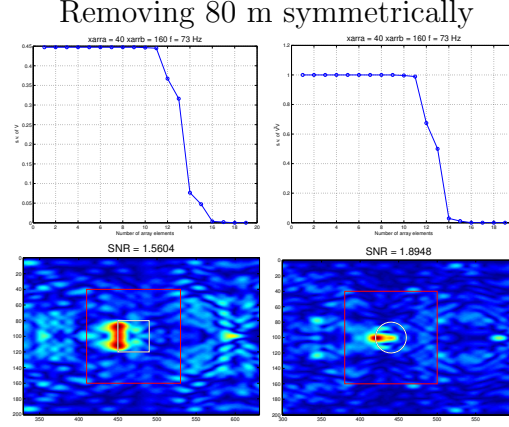


Figure 4.28: Top row: SVD of V (left) and $V^T V$ (right). Bottom row: Imaging with \mathcal{I}^{KM} (left) and $\tilde{\mathcal{I}}^{\text{KM}}$ with tolerance (right) for the square, when we remove 80 m from the array symmetrically, for $f = 73$ Hz.

In Figure 4.29, we have now that the selective images are too noisy to use, with the exception of the image for $J = 3$, for the square and $J = 1$ for the disc, which have a clear focusing in the middle of the objects with higher SNR than their respective full matrix images. Here, doing selective imaging for the disc gave us an image similar to the \mathcal{I}^{KM} one, but with better SNR, contrary to the square case where the \mathcal{I}^{KM} image already had information about the object. In this case, we will consider that removing 80 meters from the array symmetrically is a limiting case for the disc.

Removing 80 m symmetrically

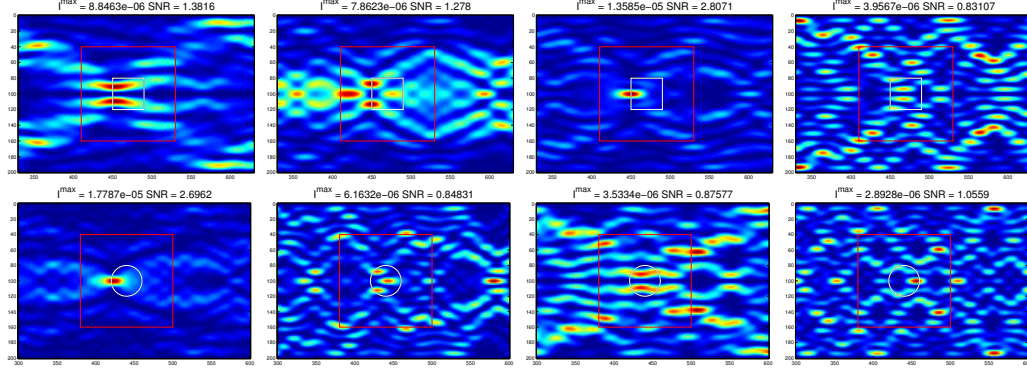


Figure 4.29: Imaging with $\tilde{\mathcal{I}}_J^{\text{KM}}$ for the square (top) and the disc (bottom), for $J = 1, 2, 3, 4$ when we remove 80 m from the array symmetrically, for $f = 73$ Hz.

If we remove a larger part of the array, imaging with $\tilde{\mathcal{I}}^{\text{KM}}$ fails to give us information about the square as well. Here, we do not have the option to make the array denser and see if this would affect the quality of our image. This is due to the fact that in order to create the scattered field we now have to solve the wave equation numerically. This is a computationally intensive task and its cost increases with the number of elements in the array.

4.4.1 Off-centered cuts

In this section we repeat the experiments that we have performed in the previous one, but now the array is not reduced symmetrically, but we rather remove elements from the bottom of the array.

First, in Figure 4.30 we plot on the top row the singular values of V and $V^T V$. From the SVD of $V^T V$, we estimate that we now have to impose a tolerance in the computation of V^+ earlier than when we were removing elements from the array symmetrically. Indeed, in the middle row, imaging without implementing a tolerance gives us only noise. In the bottom row we see imaging with $\tilde{\mathcal{I}}^{\text{KM}}$ for the square on the left and for the disc on the right. We observe that the images have lost quality, compared to the case where we have removed 20 meters symmetrically, as it may be seen in Figure 4.23, with their focus being shifted slightly to the top.

Removing 20 m from the bottom of the array

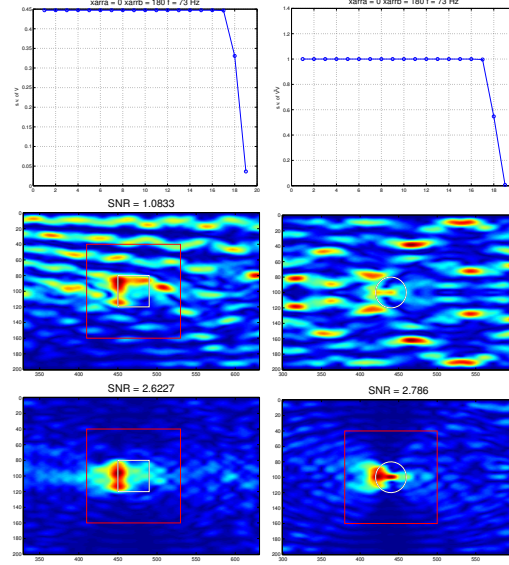


Figure 4.30: Top row: SVD of V (left) and $V^T V$ (right). Middle row: Imaging with $\tilde{\mathcal{I}}^{KM}$ for the square (left) and the disc (right) without tolerance. Bottom row: Imaging with $\tilde{\mathcal{I}}^{KM}$ for the square (left) and the disc (right) when we remove the last singular value, when we remove 20 m from the bottom of the array, for $f = 73$ Hz.

Next, in Figure 4.31 we plot the results of selective imaging with $\tilde{\mathcal{I}}_J^{KM}$ for the square on the top and the respective images for the disc on the bottom. In both cases we observe that for $J = 1$, the focusing has shifted slightly from the middle of the object, while when we focus towards the edges of the object, we do not get the symmetric results we had for the previous case.

Removing 20 m from the bottom of the array

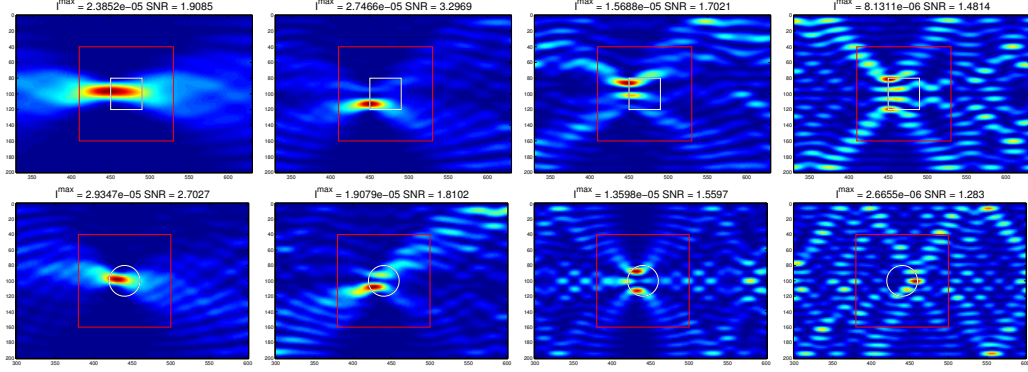


Figure 4.31: Imaging with $\tilde{\mathcal{I}}_J^{\text{KM}}$ for the square (top) and the disc (bottom), for $J = 1, 2, 3, 4$ when we remove 20 m from the bottom of the array, for $f = 73$ Hz.

Lastly, we move to the limiting case where we remove 80 meters from the bottom of the array. In Figure 4.32 we observe that the image for the square seems to focus mostly on the top side of the object, while for the disc we have a skewed focus in the middle, much like what we saw in Figure 4.28 for the symmetric case. Our hope is that doing selective imaging will give us more information about the object.

Removing 80 m from the bottom of the array

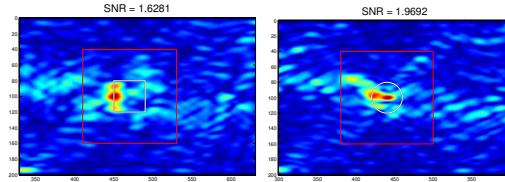


Figure 4.32: Imaging with $\tilde{\mathcal{I}}_J^{\text{KM}}$ for the square (left) and the disc (right) when we remove 80 m from the bottom of the array, for $f = 73$ Hz.

Next, in Figure 4.33 we plot the results of selective imaging with $\tilde{\mathcal{I}}_J^{\text{KM}}$ for the square on the top row and for the disc on the bottom. For the square we have that images for $J = 1, 2$ have good quality, while the image for $J = 3$ which focuses on the bottom of the object has very low SNR. For the disc however, we observe that the image for $J = 2$ gives us information about the bottom of the disc, which is an improvement over the \mathcal{I}^{KM} image.

Removing 80 m from the bottom of the array

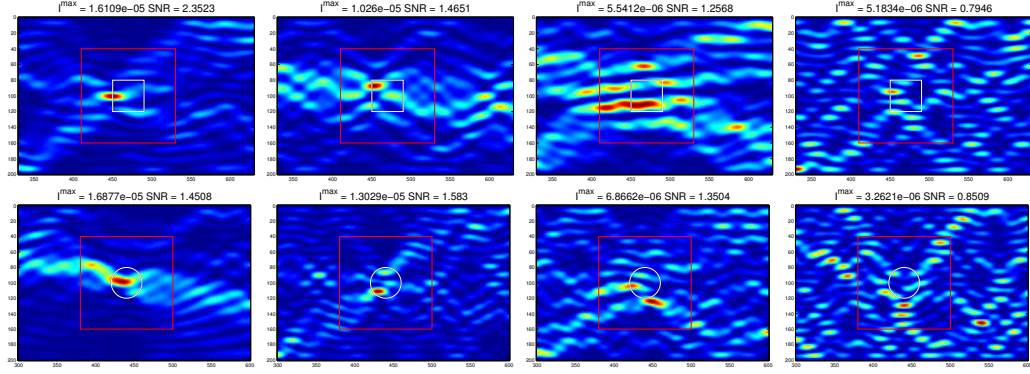


Figure 4.33: From top to bottom: Selective imaging with $\tilde{\mathcal{I}}_J^{\text{KM}}$ for the crack and the square, for $J = 1, 2, 3, 4$ (from left to right), when we remove 80 m from the bottom of the array, for $f = 73$ Hz.

Conclusion

In this work we considered the problem of selective imaging of extended reflectors in a waveguide using an active array of sensors. We have briefly discussed the full array case, which was presented in [1]. In particular, in [1] we have introduced a novel imaging functional, $\tilde{\mathcal{I}}^{\text{KM}}$, that is a variation of Kirchhoff migration where instead of back propagating the array response matrix, $\hat{\Pi}$, we back propagate a weighted modal projection of this, denoted $\hat{\mathbb{P}}$. To analyse the properties of $\tilde{\mathcal{I}}^{\text{KM}}$ we have considered a simplified model problem where the scatterer is a vertical ‘crack’. In this thesis we further investigated this problem and showed that there is a relation between the singular vectors of $\hat{\mathbb{P}}$ and the prolate spheroidal wave functions. More precisely, we observed that when the crack is fixed on the surface of the waveguide, we recover exactly the prolate spheroidal wave functions. Although this is not the case for other positions of the crack, selective imaging with $\tilde{\mathcal{I}}^{\text{KM}}$ still exhibits a prolate-like behavior, in the sense that projection on the singular vectors that correspond to the largest singular values results in an image that focuses on the bulk of the crack, projection on singular vectors that correspond to intermediate singular values results in an image that focuses on the endpoints of the crack, while projection on singular vectors that correspond to very small in magnitude singular values does not provide any information about the position and the size of the crack.

The main difference of our work compared to [1], lies in the fact that in this thesis we have considered partial array-aperture. We have extended the applicability of $\tilde{\mathcal{I}}^{\text{KM}}$ in this case, by proposing an alternative way to define $\hat{\mathbb{P}}$. The new definition of $\hat{\mathbb{P}}$ uses the regularized Moore-Penrose pseudoinverse of the matrix V , whose element V_{kl} is the value of the vertical eigenfunction X_l at the k -th array element. For the full array case, no regularization is

needed and we recover the same result as before. However, as the array aperture decreases the matrix V becomes ill-conditioned and some type of regularization is required.

We have seen that for the crack model problem, imaging with $\tilde{\mathcal{I}}^{\text{KM}}$ greatly outperforms imaging with the conventional Kirchhoff migration functional \mathcal{I}^{KM} . Despite the fact that this is a quite ideal model, it is very interesting that even if we remove half of the length of the originally full array, $\tilde{\mathcal{I}}^{\text{KM}}$ still creates images that are as good as those created with a full array-aperture. Furthermore, $\tilde{\mathcal{I}}^{\text{KM}}$ is able to locate the crack with an array that has length equal to 10% of the waveguide's depth. We have also determined a limit that, if we exceed it, selective imaging with $\tilde{\mathcal{I}}_J^{\text{KM}}$ fails, in the sense that the usual ordering in focusing does not hold anymore. (To be precise, this means that we lose the property that projection on the singular vector that corresponds to the largest singular value is associated to an image focused on the bulk of the object, while projection on the ones that correspond to smaller singular values carry information about its edges.) We have also examined the performance of the proposed imaging functionals in the presence of additive noise, and in the case of extended reflectors such as a square and a disc. In these cases the need for regularization during the computation of V^+ emerged earlier than in the crack case, since we have moved away from the ideal conditions of the model problem. However, we can still successfully image our scatterers even when we remove almost half of the array in length.

Further extensions of this work include the investigation of the case where we have an inhomogeneous waveguide. In the special case of a depth-dependent sound speed profile, the vertical eigenfunctions X_n are not known analytically, but they may be found numerically; this is not expected to affect the whole process. Also, it would be interesting to see if the presence of a larger scatterer in the waveguide would affect the quality of the images as the length of the array decreases.

Appendix A

Resolution analysis for a point scatterer

Resolution analysis is a classical way to assess the performance of an imaging method and relies on studying the behaviour of the *point spread function* (*PSF*), i.e., of the imaging functional for a *point* scatterer. We consider here an array passing through the x axis and a point scatterer placed far enough from the array at $\vec{x}^* = (z^*, x^*)$. Then, for a source located at $\vec{x}_s = (0, x_s)$ and a receiver at $\vec{x}_r = (0, x_r)$ we may approximate the (r, s) entry of the response matrix for the scattered field by

$$\hat{\Pi}(\vec{x}_r, \vec{x}_s, \omega) = \tau(\omega) \hat{G}(\vec{x}^*, \vec{x}_s, \omega) \hat{G}(\vec{x}_r, \vec{x}^*, \omega). \quad (\text{A.1})$$

In (A.1), we ignore the direct waves going from \vec{x}_s to \vec{x}_r and assume that the scattered field is simply the Green's function from \vec{x}_s to \vec{x}^* multiplied by the scattering coefficient $\tau(\omega)$ and then by the Green's function from \vec{x}^* to \vec{x}_r . In what follows, we assume for simplicity that our scatterer is an isotropic point reflector with $\tau(\omega) = 1$. Next, we replace the expression for the Green's function given by (1.5) into (A.1) taking into account only the propagating modes, and get

$$\hat{\Pi}(\vec{x}_r, \vec{x}_s, \omega) = -\frac{1}{4} \sum_{k=1}^M \sum_{\ell=1}^M \frac{e^{i\beta_k z^*}}{\beta_k} X_k(x_s) \frac{e^{i\beta_\ell z^*}}{\beta_\ell} X_\ell(x_r) X_k(x^*) X_\ell(x^*). \quad (\text{A.2})$$

For a $\vec{\mathbf{y}}^s = (z^s, x^s)$ in our search domain, the imaging functional (1.6) becomes

$$\begin{aligned} \mathcal{I}^{\text{KM}}(\vec{\mathbf{y}}^s, \omega) = \frac{1}{16} \sum_{s,r=1}^N \sum_{m,n=1}^M \sum_{m',n'=1}^M \frac{e^{i(\beta_m + \beta_n)z^*}}{\beta_m \beta_n} X_m(x_s) X_n(x_r) X_m(x^*) X_n(x^*) \times \\ \times \frac{e^{-i(\beta_{m'} + \beta_{n'})z^s}}{\beta_{m'} \beta_{n'}} X_{m'}(x_s) X_{n'}(x_r) X_{m'}(x^s) X_{n'}(x^s). \end{aligned} \quad (\text{A.3})$$

Assuming that the array spans the whole depth of the waveguide with an array pitch h small enough, we can approximate the double sum with respect to s and r in (A.3), by a double integral over x_s and x_r , and use the orthonormality of the eigenfunctions X_n to obtain

$$\mathcal{I}^{\text{KM}}(\vec{\mathbf{y}}^s, \omega) \approx \left(\frac{1}{4h} \sum_{n=1}^M \frac{e^{i\beta_n(z^* - z^s)}}{\beta_n^2} X_n(x^*) X_n(x^s) \right)^2. \quad (\text{A.4})$$

On the other hand, using (A.2) the matrix $\widehat{\mathbb{P}}$, defined in (1.13), takes the form

$$\widehat{\mathbb{P}}_{mn}(\omega) = -\frac{1}{4} e^{i\beta_m z^*} e^{i\beta_n z^*} X_m(x^*) X_n(x^*).$$

Hence, in view of the above relation, (1.12) reduces to

$$\widetilde{\mathcal{I}}^{\text{KM}}(\vec{\mathbf{y}}^s, \omega) = \left(\frac{1}{4h} \sum_{n=1}^M e^{i\beta_n(z^* - z^s)} X_n(x^*) X_n(x^s) \right)^2. \quad (\text{A.5})$$

A.1 Cross-range resolution for $\widetilde{\mathcal{I}}^{\text{KM}}(\omega)$

To examine the resolution in cross-range, we assume that the wavelength λ is much smaller than the depth ($\lambda \ll D$) and that the search point is located at the correct range, i.e., $z^s = z^*$. Then, recalling (1.3), (A.4) simplifies to

$$\mathcal{I}^{\text{KM}}(\vec{\mathbf{y}}^s; \omega) = \left(\frac{1}{2Dh} \sum_{n=1}^M \frac{1}{\beta_n^2} \sin \frac{n\pi x^*}{D} \sin \frac{n\pi x^s}{D} \right)^2, \quad (\text{A.6})$$

while (A.5) takes the form

$$\widetilde{\mathcal{I}}^{\text{KM}}(\vec{\mathbf{y}}^s; \omega) = \left(\frac{1}{2Dh} \sum_{n=1}^M \sin \frac{n\pi x^*}{D} \sin \frac{n\pi x^s}{D} \right)^2. \quad (\text{A.7})$$

We have the following result:

Lemma 1 (A.7) can be approximated by

$$\tilde{\mathcal{I}}^{\text{KM}}(\vec{y}^s; \omega) \approx \left[\frac{1}{2\lambda h} \left(\text{sinc}\left(\frac{2}{\lambda}(x^* - x^s)\right) - \text{sinc}\left(\frac{2}{\lambda}(x^* + x^s)\right) \right) \right]^2, \quad (\text{A.8})$$

where $\text{sinc}(x) = (\sin(\pi x))/(\pi x)$.

Proof 1 Letting $\xi_n = \lambda n/(2D)$ we approximate the sum over n in (A.7) by an integral. Therefore, from (A.7) we have

$$\begin{aligned} \tilde{\mathcal{I}}^{\text{KM}}(\vec{y}^s; \omega) &\approx \left[\frac{1}{\lambda h} \int_0^1 \sin\left(\frac{2\pi x^* \xi_n}{\lambda}\right) \sin\left(\frac{2\pi x^s \xi_n}{\lambda}\right) d\xi_n \right]^2 \\ &= \left\{ \frac{1}{2\lambda h} \int_0^1 \left[\cos\left(\frac{2\pi(x^* - x^s)}{\lambda}x\right) - \cos\left(\frac{2\pi(x^* + x^s)}{\lambda}x\right) \right] dx \right\}^2 \\ &= \left[\frac{1}{2\lambda h} \left(\text{sinc}\left(\frac{2}{\lambda}(x^* - x^s)\right) - \text{sinc}\left(\frac{2}{\lambda}(x^* + x^s)\right) \right) \right]^2. \end{aligned} \quad (\text{A.9})$$

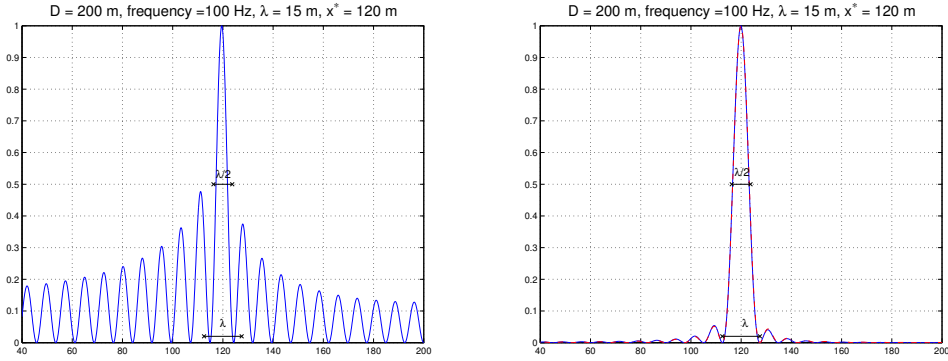


Figure A.1: Left subplot: The graph of (A.6) for $D = 200$ m, $f = 100$ Hz, $c_0 = 1500$ m/s, $x^* = 120$ m. Right subplot: The graph of (A.7) (solid blue line) superimposed on the graph of (A.8) (dashed red line), for the same parameters.

In the left subplot of Figure A.1 we plot the normalized modulus of the imaging functional (A.6) for $D = 200$ m, $c_0 = 1500$ m/s, $x^* = 120$ m and frequency 100 Hz, in the cross-range window $[40, 200]$ (in meters). In the right subplot we superimpose for the same parameters the graphs of (A.7) and (A.8), normalized with respect to their maximum values. As one may see $\tilde{\mathcal{I}}^{\text{KM}}$ exhibits considerably lower side lobes than \mathcal{I}^{KM} , albeit \mathcal{I}^{KM} 's main lobe is slightly narrower than that in $\tilde{\mathcal{I}}^{\text{KM}}$.

A.2 Range resolution for $\tilde{\mathcal{I}}^{\text{KM}}(\omega)$

In order to estimate the resolution in range we assume that the search point is located at the correct depth, i.e. at $\vec{y}^s = (z^s, x^s)$, and, for simplicity, that the scatterer is placed at half the depth of the waveguide, i.e., $x^s = x^* = D/2$.

Then, the imaging functional (A.4) takes the form

$$\mathcal{I}^{\text{KM}}(\vec{y}^s, \omega) = \left(\frac{1}{2Dh} \sum_{n=0}^{\lceil \frac{M}{2} \rceil - 1} \frac{e^{i\beta_{2n+1}(z^* - z^s)}}{\beta_{2n+1}^2} \right)^2, \quad (\text{A.10})$$

and similarly, (A.5) becomes

$$\tilde{\mathcal{I}}^{\text{KM}}(\vec{y}^s, \omega) = \left(\frac{1}{2Dh} \sum_{n=0}^{\lceil \frac{M}{2} \rceil - 1} e^{i\beta_{2n+1}(z^* - z^s)} \right)^2. \quad (\text{A.11})$$

Lemma 2 (A.11) can be approximated by

$$\tilde{\mathcal{I}}^{\text{KM}}(\vec{y}^s, \omega) \approx \left\{ \frac{1}{2\lambda h} \left[1 - \frac{\pi}{2} \mathbf{H}_1\left(\frac{2\pi}{\lambda}(z^* - z^s)\right) + i \frac{\pi}{2} J_1\left(\frac{2\pi}{\lambda}(z^* - z^s)\right) \right] \right\}^2, \quad (\text{A.12})$$

where $J_1(x)$ and $H_1(x)$ denote the Bessel and Struve function of order one, respectively, [1].

Proof 2 Let $(n + \frac{1}{2}) \frac{\lambda}{D} = \xi_n$. Then $\beta_{2n+1} = \frac{2\pi}{\lambda} \sqrt{1 - \xi_n^2}$ and the sum in the right-hand side of (A.11) may be approximated by

$$\mathcal{I}^{\text{KM}}(\vec{y}^s, \omega) \approx \left(\frac{1}{2\lambda h} \int_0^1 e^{i\frac{2\pi}{\lambda}(z^* - z^s)\sqrt{1-x^2}} dx \right)^2. \quad (\text{A.13})$$

Letting $\alpha = 2\pi(z^* - z^s)/\lambda$, we want to evaluate the integral $\int_0^1 e^{i\alpha\sqrt{1-x^2}} dx$. To this end, letting $x = \sin \theta$ we have

$$\begin{aligned} \int_0^1 e^{i\alpha\sqrt{1-x^2}} dx &\approx \int_0^{\pi/2} e^{i\alpha \cos \theta} \cos \theta d\theta \\ &= \int_0^{\pi/2} \cos(\alpha \cos \theta) \cos \theta d\theta + i \int_0^{\pi/2} \sin(\alpha \cos \theta) \cos \theta d\theta =: I_1 + i I_2 \end{aligned}$$

In I_2 we change variables $\theta = \frac{\pi}{2} - x$ to obtain

$$I_2 = \int_0^{\pi/2} \sin(\alpha \sin x) \sin x \, dx = \frac{\pi}{2} J_1(\alpha),$$

where the integral is found in [?, (3.715.2)].

For I_1 we integrate by parts

$$I_1 = \int_0^{\pi/2} \cos(\alpha \cos \theta) (\sin \theta)' \, d\theta = 1 - \alpha \int_0^{\pi/2} \sin(\alpha \cos \theta) \sin^2 \theta \, d\theta = 1 - \frac{\pi}{2} \mathbf{H}_1(\alpha).$$

For the last integral above see [?, (3.716.16)]. Finally, we have that

$$\tilde{\mathcal{I}}^{\text{KM}}(\vec{y}^s, \omega) \approx \left[\frac{1}{2\lambda h} \left(1 - \frac{\pi}{2} \mathbf{H}_1(\alpha) + i \frac{\pi}{2} J_1(\alpha) \right) \right]^2. \quad (\text{A.14})$$

In Figure A.2 we plot the modulus of the imaging functional (A.10) (left subplot) and the modulus of (A.11) versus the modulus of the graph of (A.12) (right subplot), normalized with respect to their maximum values, for $D = 200$ m, $c_0 = 1500$ m/s, $z^* = 480$ m and frequency 100 Hz, in the range window $[380, 580]$ (in meters).

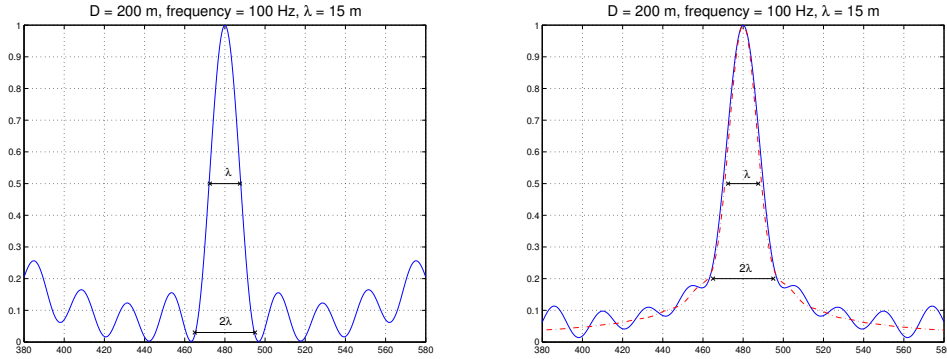


Figure A.2: Left subplot: The graph of (A.10) for $D = 200$ m, $f = 100$ Hz, $c_0 = 1500$ m/s, $z^* = 480$ m. Right subplot: The graph of (A.11) (solid blue line) superimposed on the graph of (A.12) (dashed red line), for the same parameters.

Note that for \mathcal{I}^{KM} the width of the PSF is about 2λ at less than 10% of its maximum value, while for $\tilde{\mathcal{I}}^{\text{KM}}$ the width becomes 2λ at about 20% of its maximum value.

Remark 2 *The plots in Figures A.1 and A.2 show the point spread function (PSF) of \mathcal{I}^{KM} and $\tilde{\mathcal{I}}^{\text{KM}}$ as a function of cross-range and range, respectively. We observe that the PSF is centered at the correct location of the scatterer. The resolution of the imaging method can be determined using these plots. If we define, for example, the resolution as the width of the PSF at half its maximal value we obtain a cross-range resolution of $\lambda/2$ (see Figure A.1) and a range resolution of λ (see Figure A.2).*

Bibliography

- [1] C. Tsogka, D. A. Mitsoudis, and S. Papadimitropoulos. Selective imaging of extended reflectors in two-dimensional waveguides. *SIAM J. Imaging Sci.*, 6(4):2714–2739, 2013.
- [2] N. Bleistein. *Mathematical methods for wave phenomena*. Computer Science and Applied Mathematics. Academic Press Inc., Orlando, FL, 1984.
- [3] W.A. Kuperman and D. Jackson. Ocean acoustics, matched-field processing and phase conjugation. Topics in Applied Physics, pages 43–97. Springer Berlin / Heidelberg, 2002.
- [4] L. Borcea, G. Papanicolaou, and F. Guevara Vasquez. Edge illumination and imaging of extended reflectors. *SIAM J. Imaging Sci.*, 1:75–114, 2008.
- [5] L. Borcea, G. Papanicolaou, and C. Tsogka. Subspace projection filters for imaging in random media. *Comptes Rendus Mecanique*, 338:390–401, 2010.
- [6] C. Prada and M. Fink. Eigenmodes of the time reversal operator: a solution to selective focusing in multiple-target media. *Wave Motion*, 20:151–163, 1994.
- [7] C. Prada, N. Mordant, and M. Fink. Highly resolved detection in a waveguide with the D.O.R.T. method. *J. Acoust. Soc. Amer.*, 105:1105–1105, 1999.

- [8] C. Prada, J. de Rosny, D. Clorennec, J.-G. Minonzio, A. Aubry, M. Fink, L. Berniere, P. Billand, S. Hibrat, and T. Folegot. Experimental detection and focusing in shallow water by decomposition of the time reversal operator. *J. Acoust. Soc. Amer.*, 122:761–768, 2007.
- [9] C. Hazard and K. Ramdani. Selective acoustic focusing using time-harmonic reversal mirrors. *SIAM J. Appl. Math.*, 64:1057–1076 (electronic), 2004.
- [10] B. Pinçon and K. Ramdani. Selective focusing on small scatterers in acoustic waveguides using time reversal mirrors. *Inverse Problems*, 23:1–25, 2007.
- [11] Montjoie user’s guide. <http://montjoie.gforge.inria.fr/>.
- [12] D. Slepian and H. O. Pollak. Prolate spheroidal wave functions, Fourier analysis and uncertainty. I. *Bell System Tech. J.*, 40:43–63, 1961.
- [13] H. J. Landau and H. O. Pollak. Prolate spheroidal wave functions, fourier analysis and uncertainty — II. *Bell System Technical Journal*, 40(1):65–84, 1961.
- [14] H. J. Landau and H. O. Pollak. Prolate spheroidal wave functions, fourier analysis and uncertainty—III: The dimension of the space of essentially time- and band-limited signals. *Bell System Technical Journal*, 41(4):1295–1336, 1962.
- [15] D. Slepian. Prolate spheroidal wave functions, fourier analysis and uncertainty — IV: Extensions to many dimensions; generalized prolate spheroidal functions. *Bell System Technical Journal*, 43(6):3009–3057, 1964.
- [16] D. Slepian. Prolate spheroidal wave functions, fourier analysis, and uncertainty—V: The discrete case. *Bell System Technical Journal*, 57(5):1371–1430, 1978.
- [17] F.B. Jensen, W.A. Kuperman, M.B. Porter, and H. Schmidt. *Computational Ocean Acoustics*. Modern Acoustics and Signal Processing. Springer, 2011.

- [18] N. Bleistein, J. K. Cohen, and J. W. Stockwell, Jr. *Mathematics of multidimensional seismic imaging, migration, and inversion*, volume 13 of *Interdisciplinary Applied Mathematics*. Springer-Verlag, New York, 2001. Geophysics and Planetary Sciences.
- [19] L. Borcea, G. Papanicolaou, and C. Tsogka. Optimal waveform design for array imaging. *Inverse Problems*, 23(5):1973–2020, 2007.
- [20] G. H. Golub and C. F. Van Loan. *Matrix computations*. Johns Hopkins Studies in the Mathematical Sciences. Johns Hopkins University Press, Baltimore, MD, third edition, 1996.
- [21] J.-P. Berenger. A perfectly matched layer for the absorption of electromagnetic waves. *Journal of Computational Physics*, 114:185 – 200, 1994.
- [22] S.D. Gedney. An anisotropic perfectly matched layer-absorbing medium for the truncation of FDTD lattices. *IEEE Transactions on Antennas and Propagation*, 44:1630 –1639, 1996.
- [23] H. Zhao. Analysis of the response matrix for an extended target. *SIAM J. Appl. Math.*, 64:725 – 745, 2004.
- [24] D. Fasino. Spectral properties of Toeplitz-plus-Hankel matrices. *Calcolo*, 33:87–98, 1996.
- [25] W. F. Trench. Asymptotic distribution of the even and odd spectra of real symmetric Toeplitz matrices. *Linear Algebra Appl.*, 302/303:155–162, 1999. Special issue dedicated to Hans Schneider (Madison, WI, 1998).
- [26] Alan L. Andrew. Eigenvectors of certain matrices. *Linear Algebra and Appl.*, 7:151–162, 1973.
- [27] U. Grenander and G. Szegő. *Toeplitz forms and their applications*. Chelsea Publishing Co., New York, second edition, 1984.
- [28] J. M. Varah. The prolate matrix. *Linear Algebra Appl.*, 187:269–278, 1993.

- [29] M. Hanke and J. Nagy. Inverse Toeplitz preconditioners for ill-posed problems. *Linear Algebra Appl.*, 284(1-3):137–156, 1998. ILAS Symposium on Fast Algorithms for Control, Signals and Image Processing (Winnipeg, MB, 1997).